ABSTRACT

Title of Document: Flame Extinction and Air Vitiation Effects In FDS

In Poorly Ventilated Compartment Fires

Zhixin Hu, Master Thesis, 2005

Directed by: Arnaud Trouvé, Associate Professor

Department of Fire Protection

Abstract: Compartment fires with different ventilation conditions exhibit different dynamical behaviors, ranging from steady fuel-limited fires to unsteady air-limited fires. Numerical simulations are here performed to study compartment fires in a configuration corresponding to a scaled-down model developed at University of Maryland, in which experimental data are available. The simulations use Fire Dynamics Simulator (FDS) developed by National Institute of Science and Technology (NIST). Four different cases are studied that are representative of different fire conditions: steady over-ventilated fires; steady under-ventilated fires; and unsteady fires with partial flame quenching; unsteady fires leading to total flame quenching. To account for air vitiation and flame extinction effects, a new flame extinction model is developed and integrated into FDS. It is found that the new model improves the numerical predictions and offers the potential of a better representation of the flame dynamics and upper-layer gas composition.

Flame Extinction and Air Vitiation Effects In FDS

In Poorly Ventilated Compartment Fires

By

Zhixin Hu

Thesis submitted to the Faculty of the Graduate School of the
University of Maryland, College Park, in partial fulfillment
of the requirements for the degree of
Master of Science
2005

Advisory Committee:

Professor Arnaud Trouvé, Chair
Professor Andre Marshall
Professor Peter B. Sunderland

Acknowledgements

First I would like to give the most thanks to my advisor, Dr.Trouvé, on offering me the chance to study and work in the department of fire protection in University of Maryland, the place where I had the best time ever. It has been a nice experience working with Dr. Trouvé, who shed me the light on how the high quality research work should be achieved, thanks for your strict demanding and patient instruction.

Appreciation is also going to Dr. Marshall and Dr. Sunderland. I learned a lot in both of your classes, and here it's my honor to have you being my committee member. Thanks for your support and time when you witness one of my biggest moments in my life.

I would also thank all professors and graduate students in this department, including professor Quintiere and coworkers Yunyong, Guillaume, Justin. There are so many guys in the following that I want to present my appreciation one by one, but here I have to speak one word "Thank you" to all of you: Sean, Darlene, Yi, Di, Monique, Tensei, Vivien, Yao, Ma, Lian, Peter; it's such a great time we've been together and all those occasions will be fixed in my memory. Other people whom I get to know since I came to U.S. also deserve my thanks here: Liang, Ray, Chris, Panyong, George, Ouyang, Sauro; you made my many hours after work meaningful .

Finally, I would thank my family member, dad, mom and brother. You are the most important ones to me in the world. I will love you for my whole life.

TABLE OF CONTENT

List of Figures

List of Table

Chapter I: Introduction

1.1   Overview

Fire is a complex phenomenon with various hazards to human, property and the environment. According to NFPA (National Fire Protection Association) report "Fire Loss in the United States During 2003", fire occurs in a structure at an average of once every 61 seconds. A civilian is injured in a fire every 29 minutes, and dies in one every 134 minutes. Four out of five fatal fires occur at home, which gives us a strong motivation to study compartment fires.

A lot of experimental studies on compartment fires have been done including Zukoski's work[1]. Compartment fires are characterized by three phases. The first phase is a *fire development phase* as the fire grows in size from a small incipient fire. If it is not put out, it will grow to a *fully developed* fire controlled by the amount of fuel available (*fuel controlled, well ventilated*) or the amount of air supplied through vents (*ventilation limited*). After all of the fuel is consumed, the fire will decrease in size, which can be called the *cooling phase* (*decay*). Through the whole process two factors are fatal to human life. One is smoke accumulation, as well as other toxic species that are generated such as CO, which is a threat to people involved in the fire or to firefighters. It is reported that 87 firefighters died of smoke inhalation while operating inside structures in the United States during the decade between 1990-1999. The other is possible flashover, which corresponds to a sudden transition from a developing fire to a fully developed fire. This rapid fire phenomenon can easily get people trapped without warning, and in its

generic sense, is a significant killer of firefighters. NFPA statistics recorded between

1985 and 1994 reported that a total of 47 US firefighters lost their lives because of

flashover. It is characterized by a sudden change of fire size to a point of involving all of

the fuel available in the compartment. If the compartment does not get sufficient air, the

flame will extend outside of the compartment. It usually corresponds to ventilation-

limited conditions. Average temperatures can rise to very high levels during flashover

(see Figure 1).
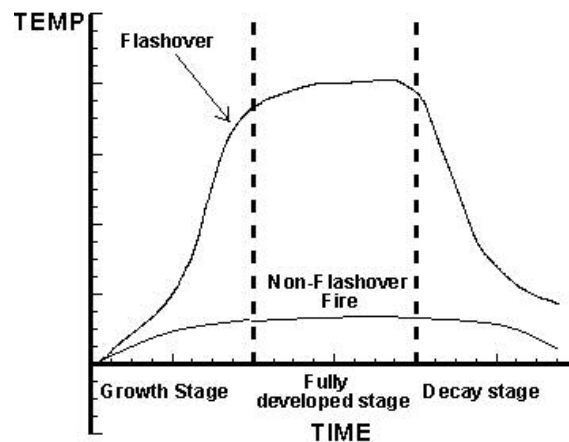
Figure 1: Flashover and non-flashover fire room temperature evolution

Due to different ventilation conditions, well-ventilated fires and ventilation-limited

fires exhibit different spreading and growth characteristics, giving different thermal and

species scenarios. A well-ventilated fire will extinguish only when the fuel is depleted or

a fire suppression system is activated. The combustion is always air-sufficient, so the fire

is relatively stable and duration is always long. When the flow of air into the enclosure is

less than the amount required for complete combustion of the vaporized fuel, ventilation

effects appear which lead to a fuel rich combustion with high CO generation [2]. The

flame is no longer stable, the fire can self-extinguish (locally or totally), and more

incomplete combustion species will be produced involving a much more complex combustion process. The difference in fire and smoke behavior is shown in Figures 2 and 3. A useful concept to quantify the effects of fire ventilation is the global equivalence ratio (GER), as discussed in the paper by Pitts [3]. It is defined in Equation (1). Globally $\dot{m}_f$ is the fuel mass loss rate, r_s is the stoichiometric oxygen-to-fuel mass ratio, and $\dot{m}_{o2}$ is the oxygen mass flow rate through the vents.

$$GER = \left(\frac{r_s \times \dot{m}_f}{\dot{m}_{o2}} \right) \tag{1}$$

By definition, GER<1 for a fuel-limited fire and GER>1 for a ventilation-limited fire. GER has been shown to be critical in correlating the composition of the upper layer in compartment fires [4], although in some cases the GER correlations show variations, in particular with hood experiments and more realistic compartment fires.

First I will review the fire behavior under well-ventilated and ventilation-limited conditions, which differ in three ways:

(1) Flame position and shape

While in a well-ventilated case, the flame is seated above the burner in an under-ventilated case, the flame tends to move towards the vent due to insufficient air supply. The flame can be easily stretched and broken, which also makes it weak and contributes to the self-extinguishment. A sketch of the differences in flame structure can be found in figures 2 and 3.
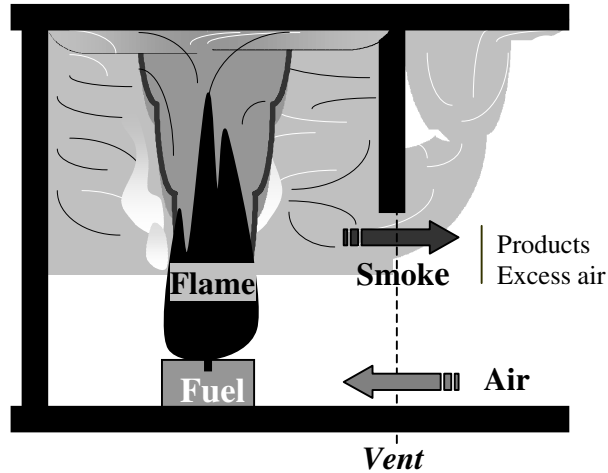
Figure 2: Well-ventilated fire configuration
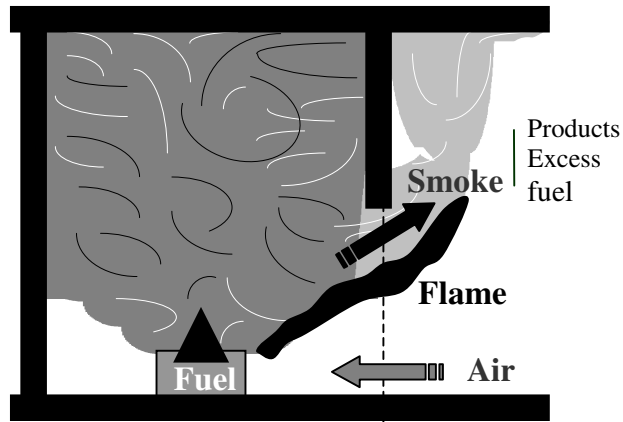
Figure 3: Under-ventilated fire configuration

(2) Air vitiation effects

Air vitiation is important because of its effect on combustion intensity and possible flame extinction. Under well-ventilated fire conditions, the lower air layer is thick and the doorway mixing between outgoing upper layer gases and incoming lower layer air has little impact on the fire. Under ventilation-limited fire conditions, air vitiation happens because of mixing between incoming fresh air and recirculating combustion products,

which results in a reduced oxygen concentration within the enclosure. This dilution effect has a negative impact on burning intensity. Once the oxygen concentration is below the lower-flammability limit, which is introduced in [5], or lower oxygen index (LOI), the flame is extinguished. However, the vitiated air is also preheated, which has a positive effect on flame burning. Due to inherent heat losses in the compartment system, the dominant effect is that of dilution and the net effect of air vitiation is to decrease the burning rate, possibly up to quenching conditions. Note that classical flame theory shows that both oxygen depletion and flame stretch are important in determining flame extinction conditions [6, 7, 8]. The effect of flame stretch or scalar dissipation rate is neglected in this study but will be considered in future work.

(3) Upper layer composition

Incomplete combustion in under-ventilated fires causes much more soot and CO emission, which is a safety hazard. In the research by Leonard and Mulholland[9], it is found that the generation of CO during ventilation-limited combustion of methane and ethane is a factor of 100 greater than for over-ventilated burning.

1.2 Literature Review

Many studies on the gas composition in compartment fires have been performed. Effect of combustion conditions on species production is described in the SFPE (Society of Fire Protection Engineers) Handbook [10]. Major species production rates by solid fuels in a two layer compartment fire environment were measured by Beyler [11]. The rates were found to be correlated by the fuel to oxygen mass ratio, which is similar to the

results obtained with simple gaseous fuels and evaporating liquid fuels. Experiments were done by Zukoski to study the species production in the upper layer of a room fire, in a configuration where the base of the natural gas flame is immersed in air and the upper part of the flame is in the vitiated gas [12]. Together with Morehart, he also studied experimentally the oxygen concentration in a vitiated environment of combustion products mixed with air which surrounded a large-scale diffusion flame[13, 14]. They measured the limiting oxygen concentrations and chemical species produced in fires near the flammability limit for methane and ethylene. Other relevant research on combustion products includes Refs [15, 16].

Of all fire-generated toxins, CO represents the most hazardous. Over half of all fire fatalities have been attributed to CO inhalation. Concentrations as low as 4000 ppm (0.4 percent by volume) can be fatal in less than an hour, and carbon monoxide levels of several percent have been observed in full scale compartment fires. Excess CO_2 and low oxygen also add to human fatal danger in fire scenarios. Leonard and Mulholland used a Burke-Schumann type burner to study the generation of CO and smoke during underventilated combustion, and they found that the peak of CO yield for methane and ethane is at least a factor of 100 greater than for overventilated burning. The proportionality between smoke yield and CO yield observed for overventilated burning for a wide range of fuels is found not to be valid for the underventilated case [9].

The mechanisms of CO generation have also been explored. In the work by Lomax and Simmons [17], it was determined that the primary oxidation reactions in the fire

plume and the secondary oxidation processes occurring in theupper layer above the burner are responsible for the increased formation of carbon monoxide which occurs with flames burning without enough oxygen. In Mulholland's experiment [18], it is also revealed that the CO yield from free burning in air vitiated separately by nitrogen and by carbon dioxide is mainly controlled by the flame temperature. The study of the effect of temperature on carbon monoxide production by Gottuk supports this theory[1 9]. Upper layer temperatures below 800 K correspond to chemically inert layers, and combustion within the fire plume dominates the CO production; when the upper layer temperature is above 900 K, chemical reactions in the bulk of the upper layer will contribute significantly to the final CO levels.

While there has been extensive experimental work on ventilation-limited combustion as well as on CO and smoke generation, in terms of the global equivalence ratio [20, 21], there has been little research on the Computation Fluid Dynamics (CFD) modeling of underventilated fires and flame extinction. Hyde and Moss proposed a model of CO production in compartment fires, based on laminar flamelet relationships, which are derived from computations of vitiated laminar diffusion flames, and a simplified two-step eddy dissipation model [22].

Tuovinen's work is similar [23-25]; it is aimed at simulating the combustion of hydrocarbons in under-ventilated conditions using the CFD code SOFIE; two different models (a laminar flamelet model and Magnussen's eddy dissipation concept) are considered. The chemistry of the hot upper layer has been investigated with respect to

CO production with the chemical kinetics code CHEMKIN, varying parameters such as equivalence ratio, temperature, oxygen, unburned fuel, and incomplete combustion products. Addition of extra CO_2 into the mixture increases the formation of CO and decreases the soot volume fraction. This effect increases with increasing temperature and equivalence ratio.

An algorithm based on experimental correlations was proposed by Pitts for the estimation of carbon monoxide concentrations in enclosure fires. Four CO formation mechanisms are considered – (1) quenching of a turbulent fire plume upon entering a rich upper layer, (2) mixing of oxygen directly into a rich, high-temperature upper layer with subsequent chemical reaction, (3) pyrolysis of wood in a high -temperature, vitiated environment, and (4) approach to full-equilibrium concentrations in a rich, high-temperature upper layer [26].

As mentioned above, CFD modeling is an essential tool in helping us predict fires and identify basic mechanisms. In the past decade, fire modeling went through the transition from zone to field models. Zone modeling decomposes a fire compartment into different distinctive zones, with uniform properties in each zone, simplifying the problem into a few sub-regions. Zone models have been available for a long time and are still popular and useful for many fire engineering calculations. An example is the paper by Quintiere [27] , in which a one-zone model is used to examine the fire behavior in building compartments. CFAST is a representative zone model for fire applications [28]. Zone modeling is computationally cheap, making the domain of application large without a

need for large computer resources. But its accuracy is also limited, since variables of interest are averaged over zones with significant spatial dimensions, resolution is poor and important local effects cannot be tracked. In contrast, field modeling features moderate-to-high accuracy by providing increased spatial and temporal resolution, at the cost of increased requirements for computational resources.

Another drawback of zone models is the necessity of a priori knowledge of the structure of the flow, which should be extracted either from experiments, or from theoretical considerations. Assumptions have to be always confirmed and can never be decoupled from supporting experimental studies. Field modeling overcomes this problem by resorting to the first principles of mechanics and thermodynamics. Therefore, field models are more general, with possible changes in the flow structure and the fire environment being accounted for automatically [28].

Depending on the method adopted for the treatment of turbulence phenomena, there are three major approaches in field models, which are: (i) Reynolds-Averaged Navier-Stokes (RANS); (ii) Direct Numerical Simulations (DNS); (iii) Large Eddy Simulation (LES). In *RANS models* the basic Navier-Stokes equations are filtered in order to obtain *statistically-averaged* flow values. In flows with large variations of density, such as flows with combustion, a convenient description is achieved via a variant of RANS filtering known as Favre-averaging. RANS models have proved to be a powerful tool in fire predictions, with all important processes being addressed by various available submodels. However, they have major limitations due to uncertainties in turbulence modeling.

DNS is an exact approach to turbulence simulation, which corresponds to a direct solution of the Navier-Stokes equations without averaging or approximations other than the necessary numerical discretizations. It is the most accurate method in CFD [29,30], but is unfortunately limited to simple flows and low Reynolds numbers due to the prohibitively expensive computational cost.

Compared to DNS, LES achieves a reduction in the computational load by applying a spatial filter to the governing equations so that large-scale turbulent fluctuations are resolved and small-scale fluctuations are modeled. Large-scale eddies contain most of the turbulent flow kinetic energy, so that resolving the large scale flow structure will provide key information, while not resolving the small scale flow structure will make the computational load acceptable. Furthermore, small eddies tend to be universal in character, so that their modeling is expected to be more reliable. Fire Dynamic Simulator (FDS) is a CFD solver developed by National Institute of Standard and Technology (NIST) featuring a LES formulation for turbulence [31-33]. FDS has been well validated for well-ventilated fires; however, its use for ventilation-limited fires needs to be explored and is the main focus of the present study.

1.3   *Research Objective*

This study will focus on the FDS capability for ventilation-limited fires. FDS predictions will be compared to a small-scale compartment fire experimental database developed at University of Maryland [34-36]. A flame extinction model is proposed and

incorporated into FDS in order to describe flame quenching phenomena resulting from

excessive air vitiation effects.

Chapter II: Model Description

2.1 FDS Combustion model

FDS (Fire Dynamic Simulator) is a fire modeling software developed by the
Building and Fire Research Laboratory (BFRL) at the National Institute of Standards and
Technology (NIST), based on LES (large eddy simulation) techniques, using a finite
difference scheme (2nd order in time, 1st~2nd order in space). Conservation equations of
mass, momentum and mixture fraction are solved under the low-Mach number
assumption, as in equations (2-4) below. The mixture fraction equation is a substitution
of species conservation equation, with no source term, which simplifies the resolution
process and makes FDS a powerful tool. The conservation equation of mixture fraction
will be explained later.

Conservation of Mass

$$\frac{\partial \rho}{\partial t} + \nabla \cdot \rho \vec{u} = 0 \tag{2}$$

Conservation of Momentum

$$\rho \left(\frac{\partial \vec{u}}{\partial t} + \left(\vec{u} \cdot \nabla \right) \vec{u} \right) + \nabla p = \rho \vec{g} + \vec{f} + \nabla \cdot \tau \tag{3}$$

Conservation of Mixture Fraction

$$\frac{\partial}{\partial t} \left(\rho Z \right) + \nabla \cdot \left(\rho Z \vec{u} \right) = \nabla \cdot \left(\rho D \nabla Z \right) \tag{4}$$

Equation of State

$$p = p_0 - \rho_\infty g z + \tilde{p} \tag{5}$$

$$p_0 = \rho T R \sum (Y_i / M_i) = \rho T R / M \qquad\qquad (6)$$

The conservation equations above are supplemented by an equation of state to give the thermodynamic quantities, instead of solving for the energy equation. Temperature is obtained from the ideal gas law, with the simplification that pressure is approximated by the "background" component. The pressure is decomposed into three parts: a "background" component, a hydrostatic component, and a flow-induced perturbation, as in equation (5). For low-Mach number flows, p_0 is spatially uniform (possibly a function of time) and the other two components are relatively small. So we can use p_0 in the state equation (6) and assume that the temperature and density are inversely proportional. In this formulation, the density is obtained from equation (2) and temperature from equation (6), without solving an energy equation.

Although there is no energy equation in FDS, the effect of the heat release rate on the flow is retained through a model expression for the divergence of velocity, which is then used in the following mass conservation and mixture fraction equations as well as in the Poisson equation for pressure (see below). The *mass conservation equation (2)* is rewritten as:

$$\frac{\partial \rho}{\partial t} + \vec{u} \nabla \rho = -\rho \nabla \cdot \vec{u} \qquad\qquad (7)$$

The *momentum equation (3)* is also re-formulated as follows:

1. Substract the hydrostatic pressure gradient, $\rho_\infty \vec{g}$, from both sides. Note that

    $$\nabla p = \rho_\infty \vec{g} + \nabla \tilde{p}$$

2. Apply the vector identity: $(\vec{u} \cdot \nabla) \vec{u} = \nabla |\vec{u}|^2 / 2 - \vec{u} \times \vec{\omega}$

3. Divide all terms by the density, ρ

4. Decompose the pressure term: $\dfrac{\nabla \tilde{p}}{\rho} = \dfrac{\nabla \tilde{p}}{\rho_\infty} + \left(\dfrac{1}{\rho} - \dfrac{1}{\rho_\infty}\right)\nabla \tilde{p}$

5. Define $H = \dfrac{|\bar{u}|^2}{2} + \dfrac{\tilde{p}}{\rho_\infty}$ (H may be interpreted as a pseudo total pressure), and H is

    solved by a Poisson solver in FDS.

So the momentum equation is written as:

$$\frac{\partial \bar{u}}{\partial t} - \bar{u} \times \bar{\omega} + \nabla H + \left(\frac{1}{\rho} - \frac{1}{\rho_\infty}\right)\nabla \tilde{p} = \frac{1}{\rho}\left[(\rho - \rho_\infty)\bar{g} + \bar{f} + \nabla \cdot \tau\right] \tag{8}$$

Furthermore the *mixture fraction equation (4)* is transformed to the following form:

$$\frac{\partial}{\partial t}(\rho Z) + \bar{u} \cdot \nabla(\rho Z) = -\rho Z \nabla \cdot \bar{u} + \nabla \cdot (\rho D \nabla Z) \tag{9}$$

The mixture fraction $Z(\bar{x}, t)$ is a conserved quantity that describes the mixing and is used to correlate the chemically reacting flow composition. It is made non-dimensional and is equal to 1 in the fuel supply stream and to 0 in the air supply stream. Mixture fraction may be expressed in terms of the oxygen and fuel mass fractions:

$$Z = \frac{Y_f - (Y_{O_2} / r_s) + (Y_{O_2,a} / r_s)}{1 + (Y_{O_2,a} / r_s)} \tag{10}$$

With the flame-sheet approximation, the mass fraction of each species and temperature (if combustion is adiabatic) are correlated to mixture fraction in a piecewise linear form. These correlations are known as "state relations" and are presented in Figure 4.
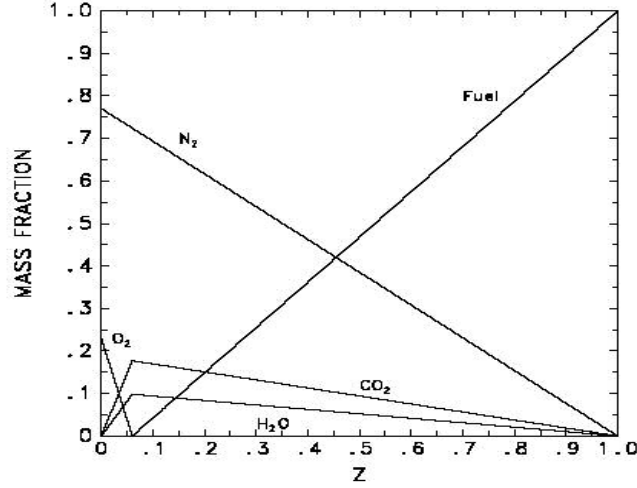
Figure 4: Burke-Schumann state relations for the main chemical species (Heptane)

The state relations are strictly valid for infinitely fast chemistry. The corresponding

equations are shown in the following equation sets (11)-(12), in which η is the mass of

species produced per unit mass of fuel consumed, $\eta_{CO_2} = -\dot{\omega}_{co_2}/\dot{\omega}_f$; $\eta_{H2O} = -\dot{\omega}_{H2O}/\dot{\omega}_f$.

$$\begin{cases} Y_f^{eq} = 0 \\ Y_{O_2}^{eq} = Y_{O_2,a}\left(1 - \dfrac{Z}{Z_{st}}\right) \\ Y_{CO_2}^{eq} = Z\eta_{CO_2} \\ Y_{H_2O}^{eq} = Z\eta_{H_2O} \end{cases} \qquad \text{for } Z < Z_{st} \qquad (11)$$

$$\begin{cases} Y_{O_2}^{eq} = 0 \\ Y_f^{eq} = \dfrac{Z - Z_{st}}{1 - Z_{st}} \\ Y_{CO_2}^{eq} = \dfrac{Z_{st}}{1 - Z_{st}}(1 - Z) \times \eta_{CO_2} \\ Y_{H_2O}^{eq} = \dfrac{Z_{st}}{1 - Z_{st}}(1 - Z) \times \eta_{H_2O} \end{cases} \qquad \text{for } Z > Z_{st} \qquad (12)$$

15

Note that the conservation equation for mixture fraction is derived from the conservation equation of fuel and oxygen (13-14):

$$\frac{\partial}{\partial t}(\rho Y_f) + \frac{\partial}{\partial x_j}(\rho Y_f u_j) = \frac{\partial}{\partial x_j}(\rho D \frac{\partial Y_f}{\partial x_j}) + \dot{\omega}_f \qquad (13)$$

$$\frac{\partial}{\partial t}(\rho Y_{O2}) + \frac{\partial}{\partial x_j}(\rho Y_{O2} u_j) = \frac{\partial}{\partial x_j}(\rho D \frac{\partial Y_{O2}}{\partial x_j}) + \dot{\omega}_{O2} \qquad (14)$$

From the definition of the stoichiometric oxygen-to-fuel mass ratio, we have:

$$\dot{\omega}_{O2} = r_s \dot{\omega}_f \qquad (15)$$

Combining equations (13) and (14), we get

$$\frac{\partial}{\partial t}(\rho(Y_f - Y_{O2}/r_s)) + \frac{\partial}{\partial x_j}(\rho(Y_f - Y_{O2}/r_s)u_j) = \frac{\partial}{\partial x_j}(\rho D \frac{\partial(Y_f - Y_{O2}/r_s)}{\partial x_j}) + \dot{\omega}_f - \dot{\omega}_{O2}/r_s \qquad (16)$$

Using equations (10) and (15), equation (16) can be rewritten as:

$$\frac{\partial}{\partial t}(\rho(Z(1+(Y_{O_2,a}/r_s)) - Y_{O_2,a}/r_s)) + \frac{\partial}{\partial x_j}(\rho(Z(1+(Y_{O_2,a}/r_s)) - Y_{O_2,a}/r_s)u_j)$$
$$= \frac{\partial}{\partial x_j}(\rho D \frac{\partial(Z(1+(Y_{O_2,a}/r_s)) - Y_{O_2,a}/r_s)}{\partial x_j}) \qquad (17)$$

Using mass conservation, equation (17) can be simplified into equation (18), which is identical to equation (4).

$$\frac{\partial}{\partial t}(\rho Z) + \frac{\partial}{\partial x_j}(\rho Z u_j) = \frac{\partial}{\partial x_j}(\rho D \frac{\partial Z}{\partial x_j}) \qquad (18)$$

The conservation equations described above for mass, momentum, mixture fraction, and the state equation are solved numerically by dividing the physical space in the fire region into a large number of rectangular cells. Within each cell the gas velocity and

temperature are assumed to be uniform and are evolved in time [31]. The computation

can either be treated as a DNS or a LES, depending on the resolution of the rectangular

cells. For a DNS calculation where the diffusion of fuel and oxygen can be modeled

directly, a global one-step chemical reaction scheme is adopted. However, for most

configuration of interest, the computational domain is too large to use a DNS approach; a

LES approach is adopted instead, in which the large scale motions are resolved, and

turbulence modeling is applied to the unresolved small scale motions. This has to be first

done by filtering out the small scales from the governing equations. A Favre filtering

operator is defined by the following convolution integral:

$$\tilde{q}(\vec{x},t) = \frac{\overline{\rho q}}{\overline{\rho}} = \frac{\iiint_{\Omega} G_{\Delta}(\vec{x}-\vec{\xi})\rho(\vec{\xi},t)q(\vec{\xi},t)d\vec{\xi}}{\iiint_{\Omega} G_{\Delta}(\vec{x}-\vec{\xi})\rho(\vec{\xi},t)d\vec{\xi}} \tag{19}$$

where the filter kernel, G is a localized function of finite support. Different forms of

filters may be applied, such as a Gaussian filter, a box filter, or a low-pass filter (which

eliminates all Fourier coefficients corresponding to wavenumbers above a cutoff). In any

case, some length scale, Δ, is associated with each filter, so that eddies of size above Δ

are resolved, and eddies of size below Δ are modeled. A LES requirement is that the grid

size should be less than the filter size[28]. In practice, the filter size is approximately

equal to the grid size (in FDS, Δ is equal to the cubic root of the local grid cell volume).

Then the flow is decomposed into two parts:

$$q(\vec{x},t) = \underbrace{\tilde{q}(\vec{x},t)}_{\substack{grid-resolved \\ component}} + \underbrace{q''(\vec{x},t)}_{\substack{subgrid-scale \\ component}} \tag{20}$$

So we can write down the LES governing equations, where the over-bar symbol

denotes LES-filtered quantities:

Mass conservation:

$$\frac{\partial \bar{\rho}}{\partial t} + \frac{\partial}{\partial x_j}(\bar{\rho}\tilde{u}_j) = 0 \tag{21}$$

Momentum conservation equation:

$$\frac{\partial}{\partial t}\tilde{u}_i - \tilde{u}_j \times \tilde{\omega}_j + \frac{\partial \tilde{H}}{\partial x_i} + \left(\frac{1}{\bar{\rho}} - \frac{1}{\rho_\infty}\right)\frac{\partial \tilde{p}}{\partial x_i} = \frac{1}{\bar{\rho}}\left[(\bar{\rho} - \rho_\infty)g_i + f_i + \frac{\partial \tilde{\tau}_{ij}}{\partial x_j}\right] \tag{22}$$

State equation:

$$\bar{p}_0 = \bar{\rho}(\frac{R}{M})\tilde{T} \tag{23}$$

Mixture Fraction conservation equation:

$$\frac{\partial}{\partial t}(\bar{\rho}\tilde{Z}) + \frac{\partial}{\partial x_j}(\bar{\rho}\tilde{Z}\tilde{u}_j) = \frac{\partial}{\partial x_j}(\bar{\rho}(\frac{v_t}{Sc_t} + \bar{D})\frac{\partial \tilde{Z}}{\partial x_j}) \tag{24}$$

in which v_t is the turbulent kinetic viscosity, and Sc_t is a turbulent Schimidt number.

Since in LES the grid resolution is not fine enough to capture the mixing processes at all relevant scales, a sub-grid scale model for the viscosity v_t is applied, known as Smagorinsky model:

$$v_t = (C_S\Delta)^2[2(\frac{\partial \tilde{u}_i}{\partial x_j} + \frac{\partial \tilde{u}_j}{\partial x_i})^2 - \frac{2}{3}(\nabla \cdot \tilde{u})^2]^{1/2} \tag{25}$$

where model coefficient $C_S \approx 0.2,$ Δ is the length scale introduced above.

Regardless of whether one is performing a LES or a DNS calculation, the overall solution algorithm is the same. As discussed before, in the low Mach number formulation presented in equations (7-9) as well as in the Poisson equation for H, the term $\nabla \cdot \bar{u}$ is an

important quantity to represent the effect of the heat release rate on flow motions since no

energy equation is ever solved. An expression for $\nabla \cdot \bar{u}$ in Ref.[30] is:

$$\nabla \cdot \bar{u} = \frac{1}{\rho c_p T}\left(\nabla \cdot k \nabla T + \dot{q}_R''' + \dot{q}''' \right) + \left(\frac{1}{\rho c_p T} - \frac{1}{p_0} \right)\frac{dp_0}{dt} \tag{26}$$

It is important to note that while we do not solve for energy in FDS, the source terms

that contribute to energy production are still needed in the expression for the flow

divergence, for instance $\dot{q}'''$ in equation (26). Here we first derive an expression for

$\dot{q}'''$ using the infinitely fast chemistry assumption. This expression is then LES-filtered to

provide a LES submodel. We start from the conservation equation of fuel mass and the

Burke-Schumann assumption that Y_f is a function of mixture fraction $Y_f(Z)$.

$$\frac{\partial}{\partial t}\left(\rho Y_f \right) + \frac{\partial}{\partial x_j}(\rho Y_f u_j) = \frac{\partial}{\partial x_j}(\rho D \frac{\partial Y_f}{\partial x_j}) + \dot{\omega}_f \tag{27}$$

$$\frac{\partial}{\partial t}\left(\rho Y_f \right) = \rho \frac{\partial}{\partial t}Y_f + Y_f \frac{\partial \rho}{\partial t} = \rho \frac{\partial Z}{\partial t}\frac{dY_f}{dZ} + Y_f \frac{\partial \rho}{\partial t} \tag{28}$$

$$\frac{\partial}{\partial x_j}(\rho Y_f u_j) = \frac{\partial}{\partial x_j}\left(\rho u_j \right)\cdot Y_f + \rho u_j \cdot \frac{dY_f}{dZ}\frac{\partial Z}{\partial x_j} \tag{29}$$

$$\frac{\partial}{\partial x_j}(\rho D \frac{\partial Y_f}{\partial x_j}) = \frac{\partial}{\partial x_j}(\rho D \frac{dY_f}{dZ}\cdot\frac{\partial Z}{\partial x_j}) = \frac{\partial}{\partial x_j}(\rho D \frac{\partial Z}{\partial x_j})\cdot\frac{dY_f}{dZ} + \frac{\partial}{\partial x_j}(\frac{dY_f}{dZ})\cdot\rho D \frac{\partial Z}{\partial x_j} \tag{30}$$

So Equation (27) may be re-written as:

$$\frac{dY_f}{dZ}(\rho \frac{\partial Z}{\partial t} + \rho u_j \frac{\partial Z}{\partial x_j}) + Y_f(\frac{\partial \rho}{\partial t} + \frac{\partial}{\partial x_j}(\rho u_j)) = \frac{\partial}{\partial x_j}(\rho D \frac{\partial Z}{\partial x_j})\cdot\frac{dY_f}{dZ} + \frac{\partial}{\partial x_j}(\frac{dY_f}{dZ})\cdot\rho D \frac{\partial Z}{\partial x_j} + \dot{\omega}_f \tag{31}$$

The mixture fraction conservation equation can also be re-written in the same way:

$$\rho\frac{\partial Z}{\partial t} + \rho u_j \frac{\partial Z}{\partial x_j} + Z\left(\frac{\partial \rho}{\partial t} + \frac{\partial(\rho u_j)}{\partial x_j}\right) = \frac{\partial}{\partial x_j}(\rho D\frac{\partial Z}{\partial x_j})$$ (32)

The second terms on the LHS of the above two equations are zero because of mass conservation. We then have:

$$\frac{dY_f}{dZ}(\rho\frac{\partial Z}{\partial t} + \rho u_j \frac{\partial Z}{\partial x_j}) = \frac{dY_f}{dZ}\frac{\partial}{\partial x_j}(\rho D\frac{\partial Z}{\partial x_j})$$ (33)

Combining Equations (31) and (33), we find:

$$0 = \frac{\partial}{\partial x_j}(\frac{dY_f}{dZ})\cdot\rho D\frac{\partial Z}{\partial x_j} + \dot\omega_f$$ (34)

or:

$$\dot\omega_f = -\frac{\partial}{\partial x_j}(\frac{dY_f}{dZ})\cdot\rho D\frac{\partial Z}{\partial x_j}$$ (35)

We also have:

$$\frac{\partial}{\partial x_j}(\frac{dY_f}{dZ}) = \frac{d^2Y_f}{dZ^2}\frac{\partial Z}{\partial x_j}$$ (36)

The final expression for the fuel mass reaction rate is,

$$\dot\omega_f = -\rho D\left(\frac{\partial Z}{\partial x_j}\right)^2\frac{d^2Y_f}{dZ^2} = -\frac{1}{2}\rho\chi\frac{d^2Y_f}{dZ^2}$$ (37)

where χ is the scalar dissipation rate, $\chi = 2D|\nabla Z|^2$, χ has dimension of inverse time and gives a measure of the rate of fuel-air mixing.

The corresponding expression for the heat release rate is

$$\dot q''' = -\Delta h_c\left(\frac{1}{2}\rho\chi\right)\frac{d^2Y_f^{eq}}{dZ^2}$$ (38)

where Δh_c is the heat of combustion per unit mass of fuel, and the notation Y_f^{eq} is used

instead of Y_f to refer to the Burke-Schumann equilibrium chemistry solution.

From state relations in (11-12) and figure 4, the fuel mass fraction is zero when Z<Z$_{st}$

and increases linearly when Z>Z$_{st}$. Therefore the first derivative of fuel mass fraction

dY_f / dZ is zero when Z<Z$_{st}$ and equal to 1/(1-Z$_{st}$) when Z>Z$_{st}$. So the second derivative

d^2Y_f / dZ^2 is zero except at Z=Z$_{st}$, which is expressed as:

$$\frac{d^2 Y_f^{eq}}{dZ^2} = a \cdot \delta(Z - Z_{st})$$
(39)

where δ is the Dirac-delta function, $\delta(x) = 0$ when x $\neq 0$ and $\delta(0)=1$. The quantity a is

some coefficient and we need to determine its value. Integrate the second derivative as in

(40), and we get the value of a.

$$a = \int_0^1 \frac{d^2 Y_f^{eq}}{dZ^2} dZ = \int_{Z_{st}^-}^{Z_{st}^+} \frac{d^2 Y_f^{eq}}{dZ^2} dZ = \frac{1}{1 - Z_{st}}$$
(40)

We then have:

$$\frac{d^2 Y_f^{eq}}{dZ^2} = \frac{\delta(Z - Z_{st})}{1 - Z_{st}}$$
(41)

and the final expressions for the fuel mass reaction rate and heat release rate are:

$$\dot{\omega}_f = -\left(\frac{1}{2}\rho\chi\right)\frac{\delta(Z - Z_{st})}{(1 - Z_{st})}$$
(42)

$$\dot{q}''' = \Delta h_c \left(\frac{1}{2}\rho\chi\right)\frac{\delta(Z - Z_{st})}{1 - Z_{st}}$$
(43)

This last expression shows that the heat release rate is a function of two factors—the mixing rate χ (for intensity) and the mixture fraction Z (for location). Also, combustion occurs whenever fuel and air meet in stoichiometric proportions (at $Z=Z_{st}$); the model clearly does not account for flame extinction.

Now we consider a LES approach in the treatment of the heat release rate. It starts from introducing the probability density function (pdf), as in figure 4, for a random variable q. The probability of q being between q_1 and q_2 is as equation (44); and for a certain value q_1, its pdf is defined as in equation (45). Using the pdf, a complete description of the statistical distribution of the variable q is achieved in equation (46). For variable density flow problems, a Favre-averaged formulation of the pdf is used instead, see equation (47).
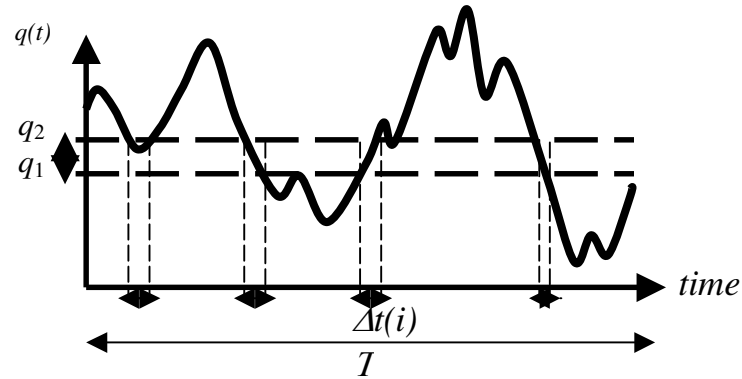

Figure 5: Probability of a random variable

$$\text{prob}(q_1 \leq q(t) < q_2) = \sum_{i=1}^{N} \frac{\Delta t(i)}{T} \tag{44}$$

$$p(q_i) = \lim_{q_2 \to q_1} \frac{\text{prob}(q_1 \leq q(t) \leq q_2)}{q_2 - q_1} \tag{45}$$

$$\overline{f(q)} = \int_{q_{min}}^{q_{max}} f(q_1) \underbrace{p(q_1) dq_1}_{\text{prob}(q_1 \leq q(t) \leq q_1 + dq_1)} \tag{46}$$

$$\tilde{f}(q) = \int_{q_{min}}^{q_{max}} f(q_1) \underbrace{\tilde{p}(q_1)}_{\text{Favre-averaged Pdf}} dq_1 \tag{47}$$

We now apply the pdf concept to the description of the statistical variations of mixture fraction and scalar dissipation rate in a LES grid cell and derive an expression for the LES-filtered fuel mass reaction rate. We write [36]:

$$\overline{\dot{\omega}_F} = \overline{\rho} \int_{Z=0}^{Z=1} \int_{\chi=0}^{\chi=\infty} \left(\frac{\dot{\omega}_F}{\rho} \right) \tilde{p}(Z,\chi) dZ d\chi \tag{48}$$

Combined with equation (43), we get:

$$\overline{\dot{\omega}_F} = -\left(\frac{1}{1-Z_{st}} \right) \frac{1}{2} \overline{\rho} \int_{Z=0}^{Z=1} \int_{\chi=0}^{\chi=\infty} \chi \delta(Z-Z_{st}) \tilde{p}(Z,\chi) dZ d\chi \tag{49}$$

The argument of the double integral can be transformed as in eqn.(50), the equation (49) will be rewritten as in eqn.(51)

$$\delta(Z-Z_{st}) \tilde{p}(Z,\chi) = \delta(Z-Z_{st}) \tilde{p}(Z_{st},\chi) = \delta(Z-Z_{st}) \tilde{p}(\chi \mid Z=Z_{st}) \tilde{p}(Z_{st}) \tag{50}$$

$$\overline{\dot{\omega}_F} = -\left(\frac{1}{1-Z_{st}} \right) \left(\frac{1}{2} \overline{\rho} \int_{Z=0}^{Z=1} \int_{\chi=0}^{\chi=\infty} \chi \delta(Z-Z_{st}) \tilde{p}(\chi \mid Z=Z_{st}) \tilde{p}(Z_{st}) dZ d\chi \right) \tag{51}$$

Which can also be rearranged as:

$$\overline{\dot{\omega}_F} = -\left(\frac{1}{1-Z_{st}} \right) \left(\frac{1}{2} \overline{\rho} \int_{\chi=0}^{\chi=\infty} \chi \tilde{p}(\chi \mid Z=Z_{st}) d\chi \right) \tilde{p}(Z_{st}) \tag{52}$$

An equivalent expression of (52) is:

$$\overline{\dot{\omega}_F} = -\left(\frac{1}{1-Z_{st}} \right) \left(\frac{1}{2} \overline{\rho} \tilde{\chi}_{st} \right) \tilde{p}(Z_{st}) \tag{53}$$

where $\tilde{\chi}_{st}$ is the conditional LES-filtered value of scalar dissipation rate, averaged along the subgrid-scale flame surface contour. $\tilde{p}(Z_{st})$ gives a measure of the local probability

of presence of the flame and $\tilde{\chi}_{st}$ a measure of the flame-surface-average intensity of turbulent fuel-air mixing. Equation (53) is the turbulent filtered analog of the unfiltered expression given in eqn.(42).

Up to this point, the only assumption that has been made is that of equilibrium chemistry. Additional simplifications for the description of the conditional mixing rate $\tilde{\chi}_{st}$ and the pdf value $\tilde{p}(Z_{st})$ need to be done. First we assume that $\tilde{\chi}_{st}$ may be approximated by the unconditional (Favre-weighted) LES-filtered scalar dissipation rate $\tilde{\chi}$. According to Ref.[37], we assume that $\tilde{\chi}$ can be approximated as:

$$\tilde{\chi} \approx 2 \left(\frac{v_t}{Sc_t} \right) \left| \nabla \tilde{Z} \right|^2 \tag{54}$$

when v_t is the Smagorinsky turbulent eddy-diffusivity, Sc_t is the turbulent Schimidt number, and $\tilde{Z}$ the (Favre-weighted) LES-filtered mixture fraction. In addition, in FDS we assume that the pdf of mixture fraction may be approximated by a simple delta function:

$$\tilde{p}(Z_{st}) = \delta(\tilde{Z} - Z_{st}) \tag{55}$$

We finally have the following model:

$$\overline{\dot{\omega}}_F = -\left(\frac{1}{1 - Z_{st}} \right) \left(\overline{\rho} \frac{v_t}{Sc_t} \left| \nabla \tilde{Z} \right|^2 \right) \delta(\tilde{Z} - Z_{st}) \tag{56}$$

$$\dot{q}''' = \Delta h_c \left(\frac{1}{1 - Z_{st}} \right) \left(\overline{\rho} \frac{v_t}{Sc_t} \left| \nabla \tilde{Z} \right|^2 \right) \delta(\tilde{Z} - Z_{st}) \tag{57}$$

2.2   *Flame Extinction model (flammability model)*

Not all fuel/oxidizer mixtures can sustain a flame, and flammability limits are always a key issue in premixed flame studies. For diffusion flames, the concept of a flammability limit was first examined by Simmons and Wolfhard [5]. The concept is more complex for diffusion flames than for premixed flames because of the influence of flame stretch [39-41], and chemical inhibition [42]. A simple flame temperature model based on the classical flame sheet approach is used as a starting point for the extinction model [31][36]. We start from the Burke-Schumann temperature relations in figure 6.
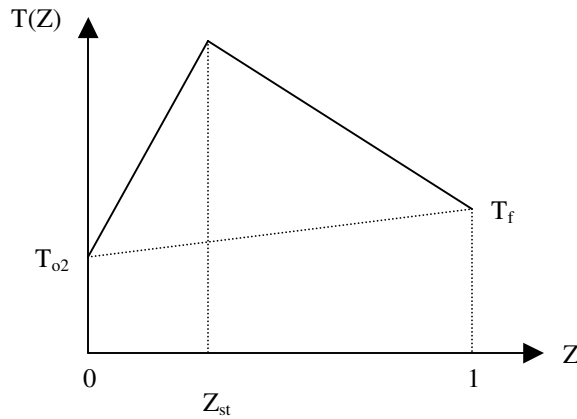

Figure 6: Burke-Schumann and pure mixing temperature relations

If oxygen and fuel mix without combustion, the mixture temperature will be like the dash line that goes from T_{o2} to T_f in fig.6, and is expressed as:

$$T = T_{o2}(1-Z) + T_f Z \qquad (58)$$

At stoichiometry, the temperature is:

$$T_{st} = T_{o2}(1-Z_{st}) + T_f Z_{st} \qquad (59)$$

With combustion, temperature increases by an amount ΔT. If a mass m_f of fuel is consumed, the increase in temperature is:

$$mc_p \Delta T = m_f \Delta h_c \tag{60}$$

where m is the mass of the mixture. The mass of fuel consumed by combustion may be evaluated by comparing the Burke-Schumann solution and the pure mixing solution in Figure 7. At stoichiometry, we have:

$$m_f = m Y_F^\infty Z_{st} \tag{61}$$
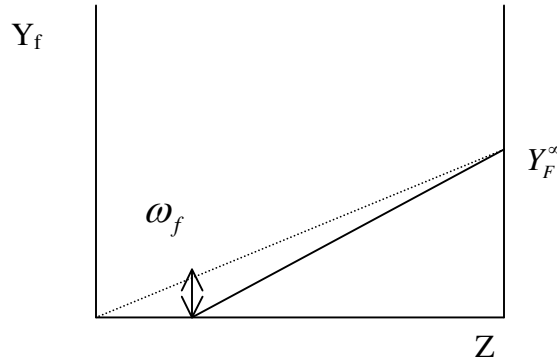
Figure 7: Burke-Schumann and pure mixing fuel mass fraction relations

Combining equation (60) and (61), we get:

$$\Delta T = Y_F^\infty Z_{st} \frac{\Delta h_c}{c_p} \tag{62}$$

The final expression for flame temperature is:

$$T_{st} = T_{o2}(1 - Z_{st}) + T_f Z_{st} + Y_F^\infty Z_{st} \frac{\Delta h_c}{c_p} \tag{63}$$

This expression assumes adiabatic combustion. A simple extension to non-adiabatic combustion is:

$$T_{st} = T_{o2}(1 - Z_{st}) + T_f Z_{st} + (1 - \chi_R) Y_F^\infty Z_{st} \frac{\Delta h_c}{c_p} \tag{64}$$

where χ_R is the radiant fraction. Note that $\quad Z_{st} = \dfrac{Y_{o2,ox}/rs}{Y_F^\infty + Y_{o2,ox}/rs}$

We can re-write equation (63) using the expression of Z_{st} :

$$T_{st} = T_{o2}\frac{Y_F^\infty}{Y_F^\infty + Y_{o2,ox}/rs} + T_f \frac{Y_{o2,ox}/rs}{Y_F^\infty + Y_{o2,ox}/rs} + Y_F^\infty \frac{\Delta h_c}{c_p}\frac{Y_{o2,ox}/rs}{Y_F^\infty + Y_{o2,ox}/rs} \tag{65}$$

which makes T_{st} a function of four variables:

$$T_{st} = function(Y_{o2,ox}, T_{ox}, Y_f^\infty, T_f) \tag{66}$$

We assume here that the fuel stream conditions are fixed: $Y_f^\infty = 1, T_f = T_{vap}$, and we consider that the flame temperature is a function of the oxidizer stream conditions:

$$T_{st} = f(Y_{o2,ox}, T_{ox}) \tag{67}$$

If the flame temperature controls flame extinction, we see that extinction is affected by both oxygen dilution (via $Y_{o2,ox}$) and preheating (via T_{o2}). We adopt in the following this flame temperature viewpoint and consider that flame extinction occurs when T_{st} falls below a critical value T_c. T_c is assumed to be independent of flow condition and fuel type. We take $T_c = 1700K$.

So the criterion for burning adopted here is that $T_{st} \geq T_c$. The flammable domain is then obtained from:

$$T_c\left(Y_F^\infty + Y_{o2,ox}/r_s\right) \leq T_{o2}Y_F^\infty + T_f\left(Y_{o2,ox}/r_s\right) + \frac{\Delta h_c}{c_p}\left(Y_F^\infty Y_{o2,ox}/r_s\right) \tag{68}$$

The equal sign in the expression above corresponds to the flammability limit. This

flammability limit corresponds to a straight line in the $(Y_{o2,ox}, T_{o2})$ diagram in figure.8. If $Y_{o2,ox} = 0$, the critical point is:

$$T_c Y_F^\infty = T_{o2} Y_F^\infty \Rightarrow T_{o2} = T_c \tag{69}$$

In addition, from the study of flammability limits of diluted diffusion flames at ambient temperature condition ($T_a = 300K$) [5], we know that $Y_{o2,ox}$ has also a critical value $Y_{o2,c}$ required to sustain burning. We take $Y_{o2,c} \approx 0.17$ (in terms of mole fraction, $X_{o2,c}$ is called the Lower Oxygen Index and is approximately 15%).
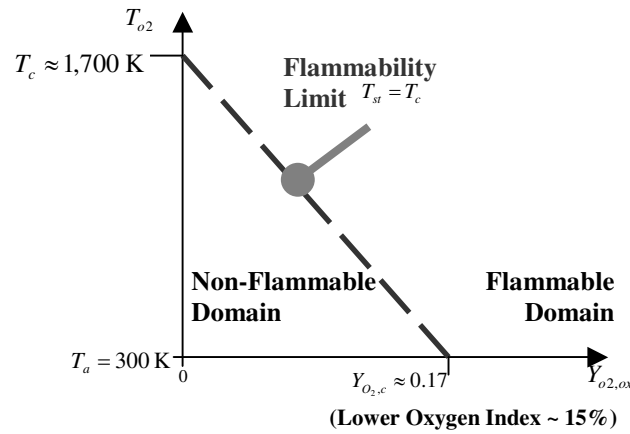
Figure8: Flammability limit in a $(Y_{o2,ox}, T_{o2})$ diagram

A useful expression for the critical extinction line is then:

$$\frac{T_c - T_{o2}}{T_c - T_a} = \frac{Y_{o2,ox}}{Y_{O_2,c}} \tag{70}$$

and the different regimes in figure 8 are identified as follows:

$$Y_{o2,ox} > Y_{o_2,c}(\frac{T_c - T_{o2}}{T_c - T_a}) \qquad\qquad \textit{Flammable domain} \tag{71}$$

$$Y_{o2,ox} \leq Y_{o_2,c}(\frac{T_c - T_{o2}}{T_c - T_a}) \qquad\qquad \textit{Non-flammable domain} \tag{72}$$

Chapter III: FDS modeling of compartment fires

It is revealed that when the global equivalence ratio in the fire room is above 0.5, or when the oxygen mole fraction in the bulk region of the ceiling layer is below a critical value LOI (Low Oxygen Index), air-vitiation effects are observed and incomplete combustion species are increasing [4,14,15]. This implies that some extinction events occur locally, which may lead to flame oscillation or total flame extinction.

In this chapter, we perform FDS simulations of an experimental configuration developed at University of Maryland to characterize the fire dynamics under poorly-ventilated conditions [33,34]. The FDS simulations are performed first with the original combustion model, i.e. without a flame extinction capability. The new extinction model in FDS will be activated in a second phase, so that its contribution can be clearly highlighted.

3.1   Experimental Configuration

The experimental setup is shown in figure 9. A cubic box of size 40 cm is used as a small scale compartment. The compartment walls are made of type-M Kaowool® board and are 2.54 cm thick. Two vents are opened on one of the sidewall, one near the ceiling, one near the floor. In different cases the vents width is varied from 2 to 40 cm, while the vent height is varied from 1 to 3 cm, giving different ventilation conditions. Heptane is supplied from a circular fuel pan in the center of floor, with the pan size ranging from 6.5

to 19 cm. A water sublayer is placed below the liquid fuel to account for heat conduction loss to pan as well as smoothing boundary effects.
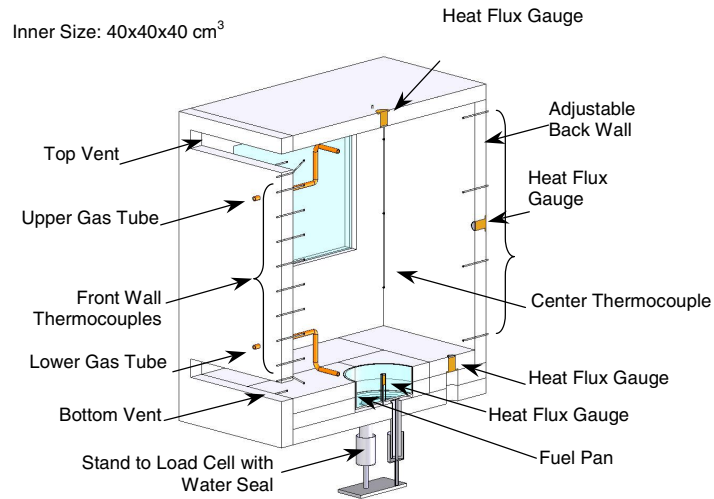
Figure 9: Schematic half-view of the experimental setup

The compartment instrumentation includes a load cell system, an array of 19 thermocouples, 4 heat flux gauges, 2 pressure transducers and a gas analysis system. The load cell is below the fuel pan and records the evolution of the fuel mass loss rate. Heat flux gauges, gas tubes, pressure transducers and thermocouples are distributed at different locations to monitor the thermal feedback to the heptane pool, the gas composition near the ceiling and floor, the flow fluctuation across the vents and the temperature evolution at specific locations. These are key data for compartment fires which we will use to compare with the simulation data.

A wide variety of flame behaviors are observed when varying vent sizes and pan sizes, as reported in Ref [33]. These different flame behaviors are analyzed and assumed to belong to one of the following four regimes: (R1) steady well-ventilated fires in which the flame is stabilized near the burner; (R2) steady under-ventilated fires in which the flame is stabilized near the vents; (R3) unsteady under-ventilated fires featuring large

periodic oscillations and temporary flame quenching; (R4) unsteady under-ventilated

fires leading to complete flame extinction. The global equivalence ratio (GER) Φ is the

main parameter distinguishing these categories. By definition, $\Phi>1$ characterizes over-

ventilated fires while $\Phi<1$ characterizes under-ventilated fires. Regime R1 corresponds to

small values of Φ, regime R4 corresponds to large values of Φ, and regime R2 and R3

correspond to intermediate, near-stoichiometric values.

Out of these four categories, four cases are selected to represent each category, as

shown in Table 1. They are characterized by different vent size or burning area, which

determines the flame behavior.

Table 1. Ventilation and fuel source parameters in cases 1-4

Case	Vent[a] Height[b] × Width[b]	Fuel Pan Diameter[b]	Flame Regime
1	3 × 40	9.5 (8)	R1
2	1 × 40	19 (16)	R2
3	3 × 10	9.5 (8)	R3
4	1 × 2	9.5 (8)	R4

[a]Single vent dimensions; multiply by two to get the total venting area

[b]In units of cm

3.2 Numerical configuration

The computational configuration is shown in figure 10, which is a schematic of the

case1 setup. In addition to the fire compartment, an adjacent air space is extended from

the vent wall of the cubic box and added to the simulation domain to treat more

accurately the vent flow rates and avoid treating the vents as numerical boundary

conditions (although the vent flow treatment is still limited by factors such as insufficient grid resolution and the absence of a proper representation of the wall thickness). In case 1, 3 and 4, the simulated air space is a cubic with 40 cm sides, and in these three cases, the computational mesh size is uniformly 1 cm. In case 2, the air space is $40*80*80$ cm^3, and while in the fire room, the mesh size is 1 cm, in the air space, the grid is stretched and designed to match the fire compartment grid resolution at the vent location. Simulations are performed either on a single- or a multi- processor Linux machine; the latter case uses the MPI (Message Passing Interface)-based version of FDS [31].

We now turn to a brief evaluation of the quality of the selected grid resolution. We start by considering the ability of the computational grid to resolve the geometrical features of the fire compartment. The only two features of interest here are the fuel pan and the vents. The numerical fuel source area is 64 or 256 cm^2 (Table 1); and with our choice of grid resolution, the corresponding footprint on the compartment floor is described by 64 or 256 grid cells. This number is large and the resolution of the fuel source is therefore rated as very good. The description of the vents is clearly much less satisfactory. For instance, the vents height may be as small as 1 cm (cases 2 and 4 in Table 1), which corresponds to the dimension of a single computational grid cell. This simplification is deemed acceptable at the present stage but it is worth emphasizing again that in the present simulations, the resolution of the vents is marginal.

Next, we consider the ability of the computational grid to resolve the expected flame structure. The fire size in cases 1-4 takes values on the order of a few thousand Watts;

and the flame length varies between 10 and 20 centimeters, which corresponds to the dimension of 10 to 20 grid cells. This number is re asonably large and the resolution of the flame is therefore rated as good.
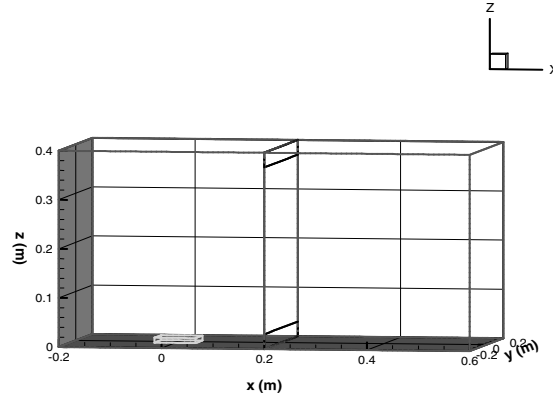

Figure 10: Computatio nal configuration

There are several simplifications made in the simulations. The first is to use a square burner instead of the round pan used in experiment; this choice is ma de because FDS is limited to rectangular grid s. Heptane is set as the fuel and injected from the burner. The burner area is close to the area of the round fuel pan (not exac tly the same because of grid geometry consideration) as repeated in the third colum n of table1 . The error in burner area is approximately 10%. A second simplification is to neglect the wa ll thickness at the vents. Note that in experiment the flow goes through vents that are 2.54cm thick, while in the FDS simulation this passage has zero thickness. This simplification is deemed acceptable at the present stage but will be removed in future work.

FDS calculations for cases 1 -4 are performed in two modes, correspond ing to two different treatments of the fuel mass loss rate (MLR): a pre scribed -MLR treatment in which the time evolution of MLR is directly taken from the experimental database and

treated as an input variable; a computed-MLR treatment in which the MLR is calculated from the gasification of the fuel due to the heat feedback and treated as a solution variable. In the following, numerical simulations performed with a prescribed-MLR treatment are identified with an extra letter P (case1P-4P), whereas simulations performed with a computed-MLR treatment are identified with an extra letter C (case 1C-4C). In cases 1C-4C, the fuel pyrolysis is initiated using a removable pilot-flame-like ignition device corresponding to a 4.8kW flame, sustained for a duration of 5 seconds, over a 16 cm^2 area centrally located above the heptane pool surface. Also for these computed-MLR cases, the value of the heat of vaporization for the fuel is a key parameter. While the thermodynamic value of the heat of vaporization for heptane is approximately 0.45 MJ/kg, the apparent value from the experimental load cell and heat flux data gives a significantly higher value, which is about 1.4 MJ/kg (this value is obtained as the ratio of the net gas-to-pool-surface radiative heat flux divided by the fuel mass loss rate). This higher value may be interpreted as an effective heat of gasification that accounts for unresolved physics, such as heat losses to the water-sublayer and to the fuel container walls, possible convective motion inside the liquid pool, semi-transparent radiation behavior of the liquid fuel layer as well as adjusting mass diffusivities. Simulations using the theoretical or experimental value of the heat of gasification are tested and compared with experimental data and the experimental value is found to provide much better results.

Chapter IV: Simulation results compared against experiments

– prescribing mass loss rate, extinction model deactivated

First we consider the FDS simulation results obtained with a prescribed mass loss rate (MLR). In the following plots, dash lines denote experimental data and solid lines denote simulation data. This convention applies to all plots, except figures (b), where the legend clarifies the plot style.

4.1   Case 1P

Case 1 is typical of regime R1 in which the combustion is fuel-limited and the flame is stabilized above the burner; turbulent fluctuations account for a certain level of unsteadiness but the flame behavior is essentially stable. Fig. 11(a) shows the measured and simulated fuel mass loss rate per unit area. The MLR per unit area in this case is about 20 g/m^{2}s, which is about twice as large as the estimated free-burn value (refer to *Appendix I for a detailed calculation*). This suggests that in regime R1, the net effect of the compartment is to increase the burning rate.

Fig. 11(b) gives the burning rate (BR) per unit area compared to the MLR per unit area in the simulation. BR is defined as the fuel mass consumption rate due to the combustion and calculated in this paper as the heat release rate $\dot{q}$ divided by the heat of combustion Δh_c and by the fuel source area. In this plot we can see that BR agrees with MLR with a small fluctuation. This shows that (on average) the fuel ejected from the burner is

35

consumed by the flame in the fire room which is consistent with a regime R1 case

corresponding to well-ventilated, fuel limited conditions.

(a)　　　　　　　　　　　　　　　　　　(b)

(c)　　　　　　　　　　　　　　　　　　(d)

(e)　　　　　　　　　　　　　　　　　　(f)

Figure 11 (*to be continued*): Comparison between experimental data (dashed line) and FDS data (solid line) in case 1P [extinction model deactivated]. (a) Fuel mass loss rate; (b) MLR and BR in the simulation; (c) Vent flow rates (upper and lower vents); (d) FDS-based isocontour plot of mixture fraction in the central vertical plane; (e) Oxygen mole fraction (near floor and ceiling); (f) Carbon dioxide mole fraction (near floor and ceiling)

(g)

(h)

(i)

(j)

(k)

(l)

(m)
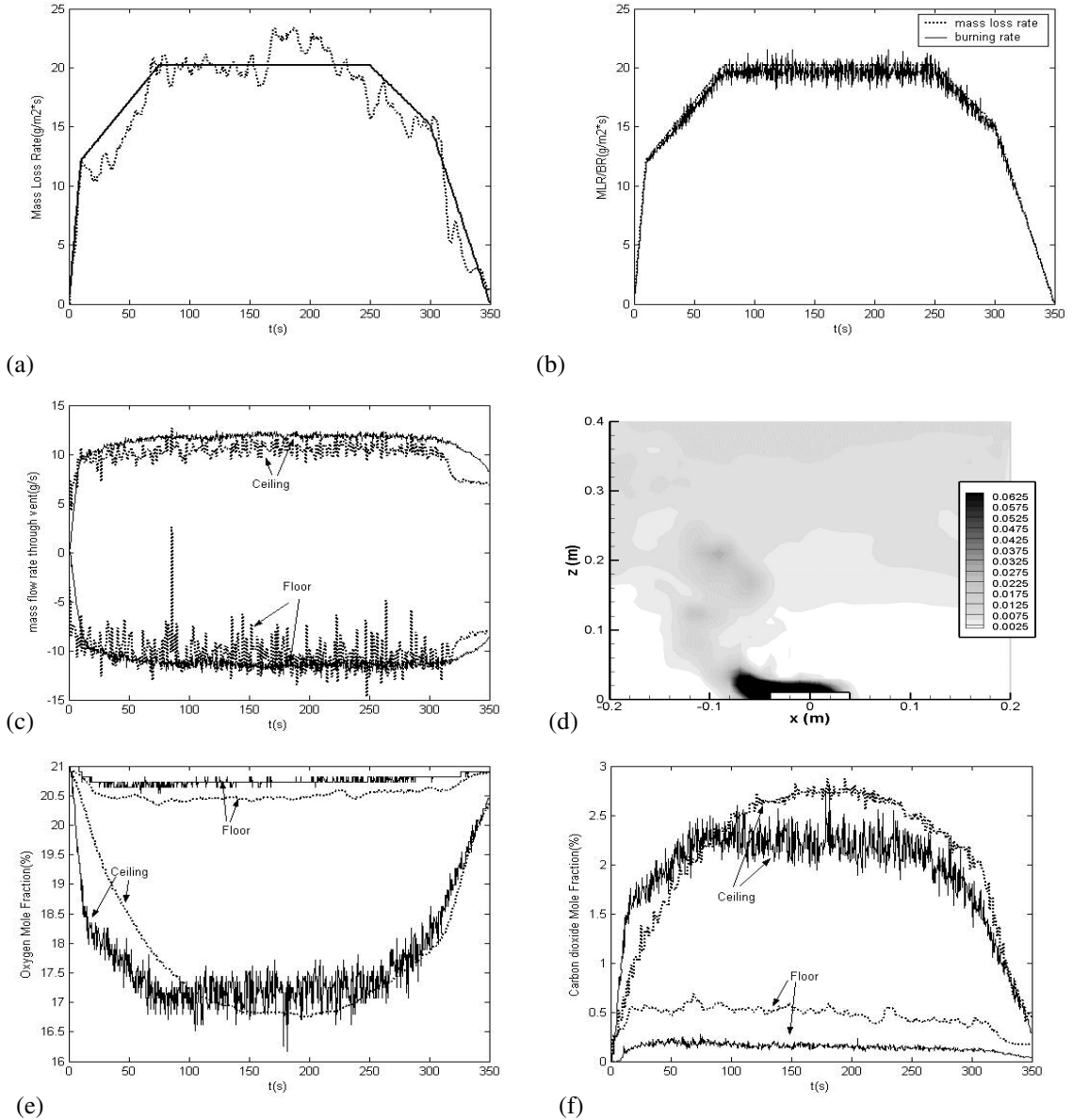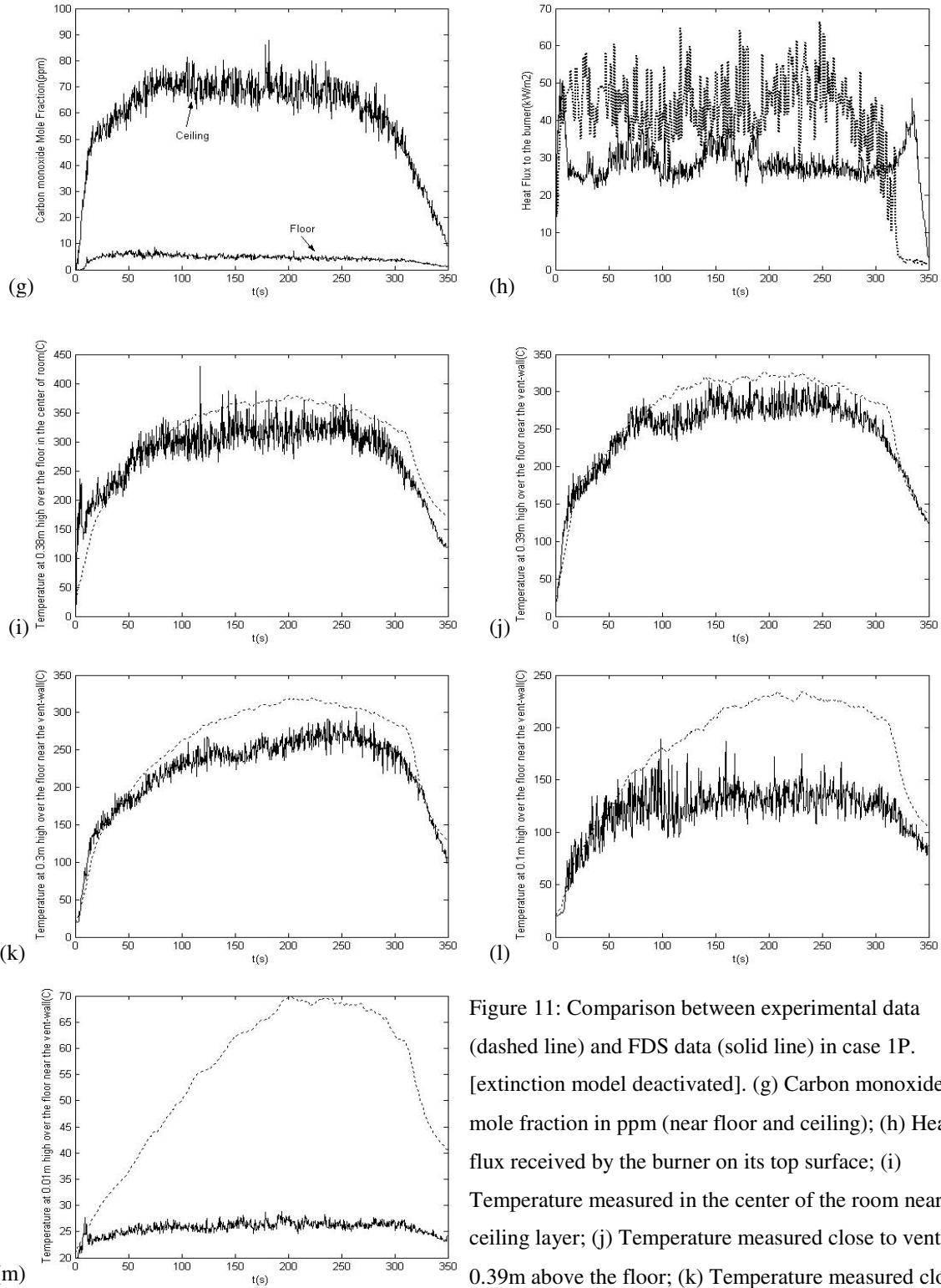
Figure 11: Comparison between experimental data (dashed line) and FDS data (solid line) in case 1P. [extinction model deactivated]. (g) Carbon monoxide mole fraction in ppm (near floor and ceiling); (h) Heat flux received by the burner on its top surface; (i) Temperature measured in the center of the room near ceiling layer; (j) Temperature measured close to vent wall 0.39m above the floor; (k) Temperature measured close to vent wall 0.3m above the floor; (l) Temperature measured close to vent wall 0.1m above the floor; (m) Temperature measured close to vent wall 0.01m above the floor.

37

Fig. 11(c) presents the mass flow rates through the upper and lower compartment vents. The experimental curves are based on pressure transducers data combined with temperature readings and Bernoulli theory. Although approximations are made in the numerical treatment of the vents, the computed and experimental mass flow rates agree very well. Using the data presented in Figs. 11(a)-(c), the fire room GER may now be evaluated as $\phi = (r_s / Y_{O2,a}) \times (\dot{m}_f / \dot{m}_a)$, where r_s is the stoichiometric oxygen-to-heptane mass ratio, $r_s \approx 3.52$; $Y_{O2,a}$ the oxygen mass fraction in ambient air, $Y_{O2,a} \approx 0.233$; $\dot{m}_f$ is the fuel MLR, $\dot{m}_f \approx 0.14\,\text{g/s}$; and $\dot{m}_a$ is the air mass flow rate though the lower compartment vent, $\dot{m}_a \approx 10\,\text{g/s}$. We find $\Phi = 0.2$, which quantifies the amount of excess air still present in case1.

Fig.11 (d) shows a snapshot of the mixture fraction isocontours at an arbitrary time, in a central vertical plane of the fire compartment that cuts through the fuel pan and the vents. The flame contour (stoichiometric value of mixture fraction) lies at the interface between the black and light grey regions and suggests that the flame features a cone-like shape attached to the fuel pan and is deflected towards the back wall.

Fig. 11(e) shows the oxygen mole fraction at the upper (ceiling) and lower (floor) layer. In this case, the numerical and experimental data agree very well, and are consistent with the classical two-layer structure of the compartment gas, in which a ceiling layer, filled with combustion products and air, lies above a fresh air floor layer. The lower layer oxygen level remains almost constant and equal to the air value, which means that enough air is present near the floor due to the well-ventillated conditions.

Fig. 11(f, g) presents the CO_2 and CO mole fractions data. The CO_2 numerical curves agree well with the experimental data, except for some slight discrepancy at the lower layer level. This plot also shows a stratification of the mixture composition with gases that are rich in CO_2 in the ceiling layer and poor in CO_2 in the floor layer. The CO plot only presents numerical predictions and no experimental data is shown because the CO detection system does not resolve signals below the 100 ppm level.

Fig. 11(h) presents the net heat flux (radiative and convective) measured at the center of the burner surface. The experimental data show a heat flux of about 45 kW/m^2, whereas the numerical data give a value around 30 kW/m^2.

Fig. 11(i) presents the measured and simulated temperature data measured in the center of the room near the ceiling, while Fig. 11(j-m) give the temperature data along the vent wall, from near ceiling to near floor. The agreement between the experimental data and numerical data is good, except at the lower location where boundary layer effects are important, and FDS under-predicts the temperature (this may involve complex physics unresolved by FDS).

4.2   Case 2P

Compared to case 1, case 2 has the vent area decreased by a factor of three and the fuel pan area increased by a factor of four, so a rough estimation of the fire room global equivalence ratio will be a twelve-fold increase from case 1, which is representative of regime R2, in which the combustion is oxygen-limited and the flame is stabilized near the

39

compartment vent. Fig.12(a) shows the measured fuel mass loss rate from the experiment

and the prescribed mass loss rate in FDS as the solid line, which is about 27 g/m^2-s. This

value is about 30% larger than the estimated free-burn value (***Appendix I***), but note that

due to a change in the flame structure (the flame is now located near the vent), the

comparison to the free-burn value has limited validity now.
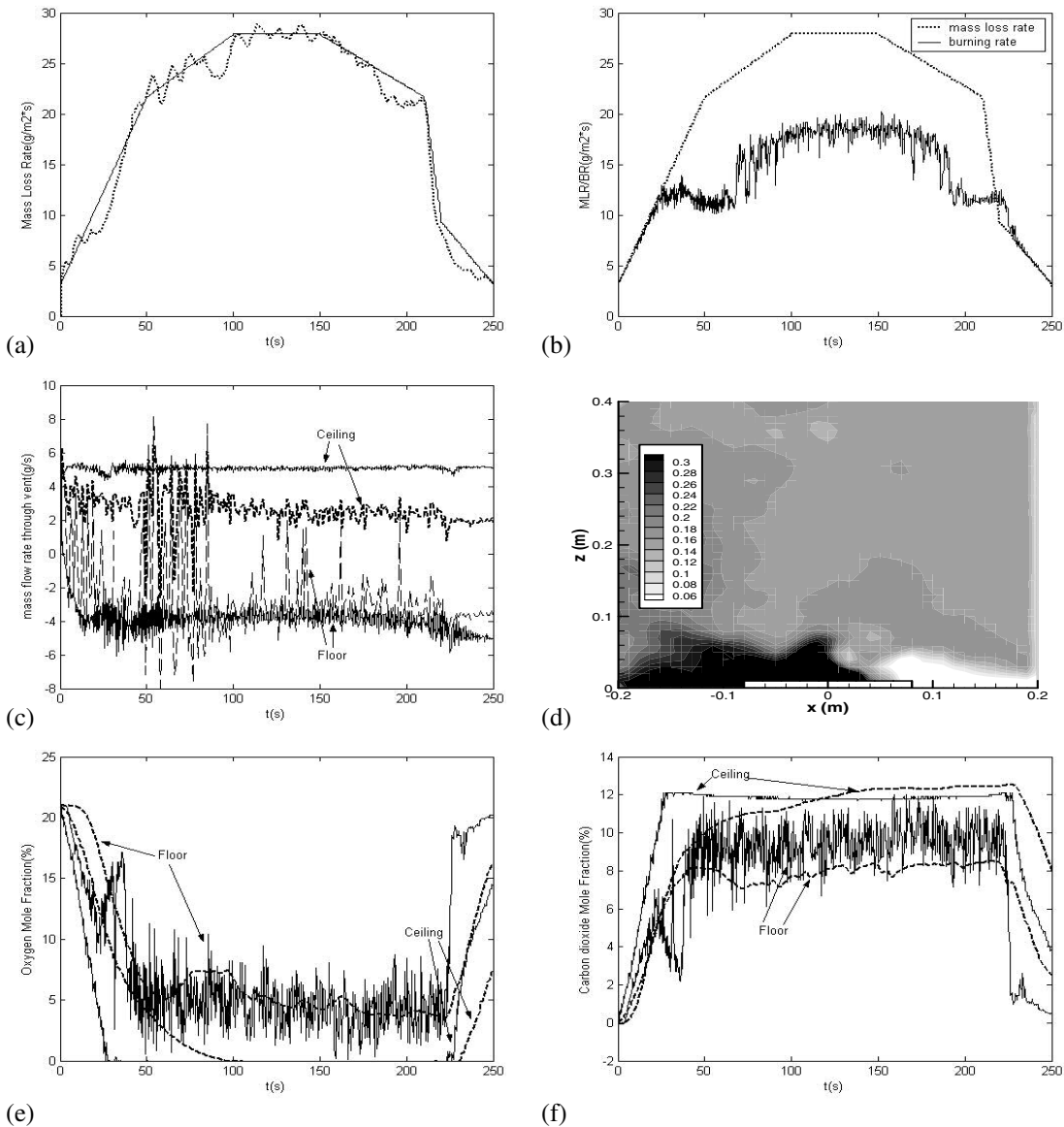

(a) (b) (c) (d) (e) (f)

Figure 12(*to be continued*): Comparison between experimental data (dashed line) and FDS data (solid line) in case 2P [extinction model deactivated]. (a) Fuel mass loss rate; (b) MLR and BR in the simulation; (c) Vent flow rates (upper and lower vents); (d) FDS-based isocontour plot of mixture fraction in the central vertical plane; (e) Oxygen mole fraction (near floor and ceiling); (f) Carbon dioxide mole fraction (near floor and ceiling)

40

Fig. 12(b) presents the burning rate (BR) per unit area compared to the MLR per unit area in the simulation. We see that BR is only 17 $g/m^2/s$, which is much less than MLR. This suggests that nearly half of the fuel ejected from the fuel pan is not burned in the fire compartment.

Fig. 12(c) presents the mass flow rates through the upper and lower compartment vents. The agreement between experimental and computational data is not as good as that obtained in case 1, but remains acceptable. Using the data presented in Figs. 12(a)-(c), the fire room GER may now be evaluated as $\phi = (r_s / Y_{O2,a}) \times (\dot{m}_f / \dot{m}_a) = (3.52/0.233) \times (0.7/4) = 2.0$, which confirms that the combustion is now ventilation-limited.

Fig.12 (d) shows an isocontour plot for mixture fraction at an arbitrary time; it is different from figure 11(d) in that a different range of isolevels is selected. In this plot, the stoichiometric flame contour lies at the interface between the white and dark grey regions. The flame now stays away from the pan and is near the lower vent where the oxygen comes in, while the excess unburnt fuel escapes the compartment from the upper vent. The flame position near the compartment vents is a clear sign of under-ventilated fire conditions.

Fig. 12(e) shows the oxygen mole fraction in the upper (ceiling) and lower (floor) layers. Both the experimental and numerical data agree that the upper layer is fuel-rich and fully depleted of oxygen, as expected for under-ventilated fire conditions. Both sets of data also predict that the oxygen mole fraction in the lower layer goes down to 5%.
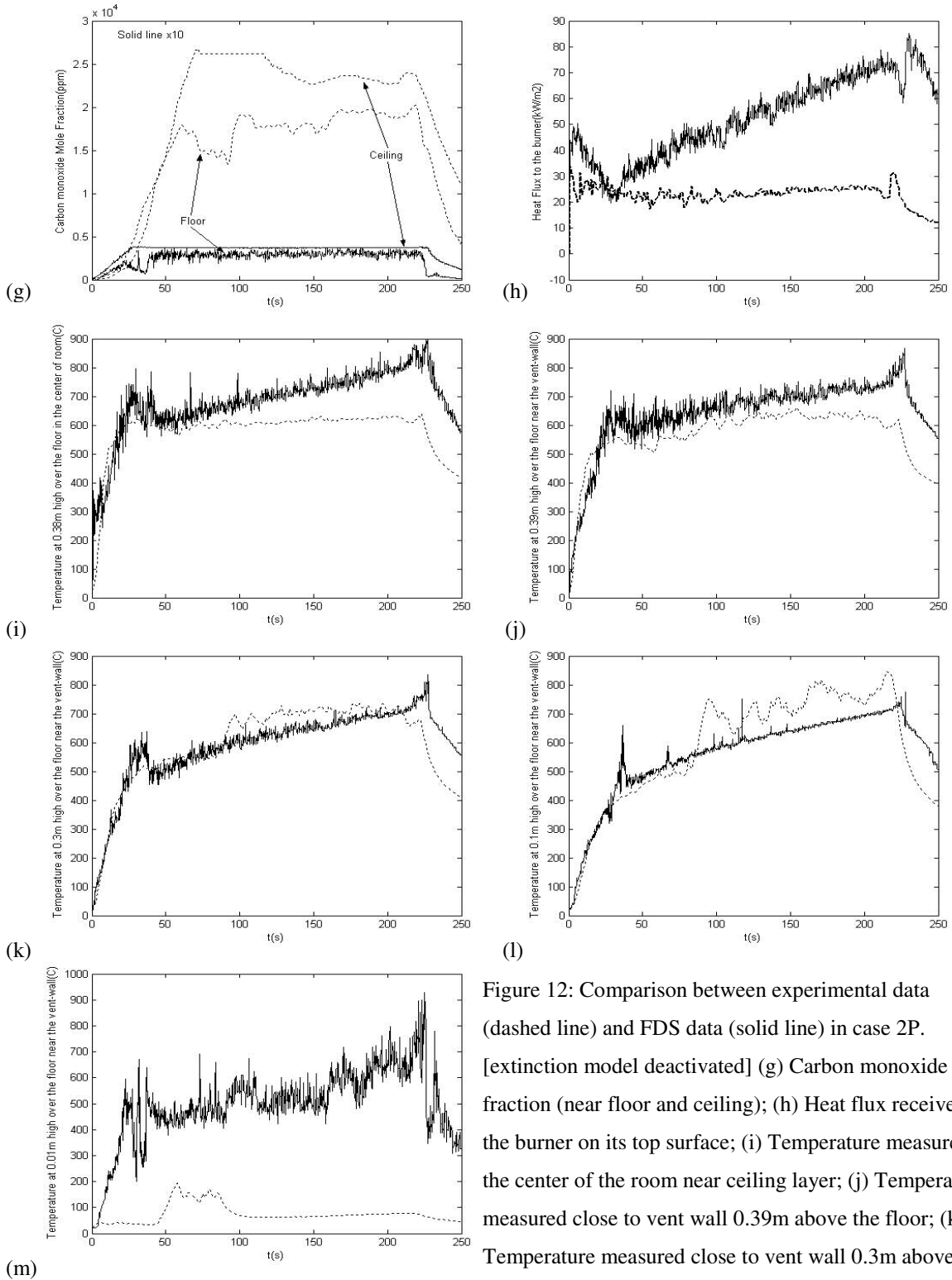
(g)

(h)

(i)

(j)

(k)

(l)

(m)

Figure 12: Comparison between experimental data (dashed line) and FDS data (solid line) in case 2P. [extinction model deactivated] (g) Carbon monoxide mole fraction (near floor and ceiling); (h) Heat flux received by the burner on its top surface; (i) Temperature measured in the center of the room near ceiling layer; (j) Temperature measured close to vent wall 0.39m above the floor; (k) Temperature measured close to vent wall 0.3m above the floor; (l) Temperature measured close to vent wall 0.1m above the floor; (m) Temperature measured close to vent wall 0.01m above the floor.

42

Fig. 12(f) presents the CO_2 mole fraction data. The agreement is good; the CO_2 mole fraction in the ceiling layer is about 12%, while it is about 8% in the floor layer. More fluctuations are observed for the FDS data.

Fig. 12(g) presents the CO mole fraction. The experiment has much higher CO concentrations than predicted. Note that the numerical data shown as a solid line have already been multiplied by 10 to facilitate the comparison. This shows the limited ability of FDS to predict CO, especially under ventilation-limited conditions. This problem should be addressed in future work.

Fig. 12(h) presents the heat flux data obtained at the center of the burner. The experimental data corresponds to a heat flux per unit area of about 25 kW/m^2, while the numerical data give an average value of 50 kW/m^2. An interesting observation here is that the numerical curve is increasing from 30 to 80 kW/m^2, which is due to the heat accumulation in the fire room as displayed in the following figures of room temperature.

Fig. 12(i) presents the temperature obtained in the center of the room near the ceiling, while fig. 11(j-m) give the temperature along the vent wall from near ceiling to near floor. Similar to case 1, the agreement of both data sets near the ceiling is good, except in the floor boundary layer.

4.3   Case3P

Now we consider case 3 (Fig. 13). Compared to case1, the vent area in case 3 is

decreased by a factor 4 and the fuel pan area is unchanged. This gives an estimation of

the fire room equivalence ratio to be four times the value of case 1, or about 0.8 and near

stoichiometry. More importantly, the flame is observed to be unstable in the experiment

(the instability frequency is about 1 Hz), which is typical of regime R3 featuring large

flame oscillations and periodic flame extinction and re-ignition. Fig. 13(a) shows that the

fuel mass loss rate per unit area continuously increases up to around 30 $g/m^2/s$, which is

about 3 times larger than the estimated free-burn value (***Appendix I***). Similar to case 1,

this also suggests that in regime R3, the net effect of the compartment is to increase the

rate of combustion.

Fig. 13(b) gives the burning rate (BR) per unit area compared to the MLR per unit

area in the simulation; we can see that BR agrees with MLR with a small fluctuation.

This is consistent with the estimated near-stoichiometric but still over-ventilated fire

conditions.

Fig. 13(c) presents the mass flow rates through the upper and lower compartment

vents. The average values of both data sets agree well, except that the numerical data do

not feature as much fluctuation as the experimental data does. This suggests that FDS

fails to reproduce the large oscillations of the flow rates observed in the experiment (the

oscillations at the lower vent are so large that the flow is found to alternate between

inflow and outflow conditions). Using the data presented in Figs. 13(a)-(c), the fire room

GER may now be evaluated as $\phi = (r_s / Y_{O2,a}) \times (\dot{m}_f / \dot{m}_a) = (3.52 / 0.233) \times (0.21 / 3) \approx 1$,

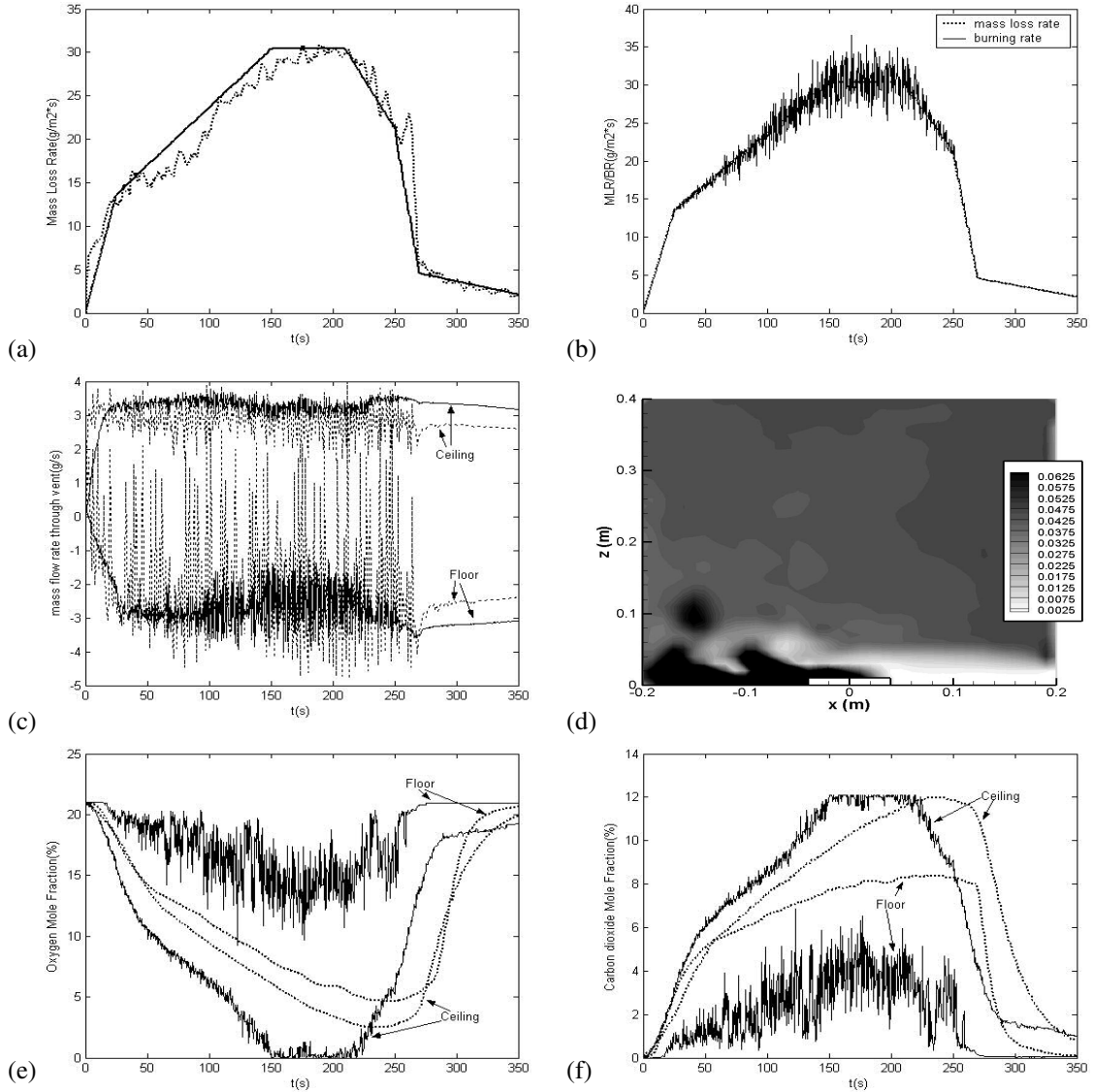which confirms the near-stoichiometric condition estimated above.

(a)

(b)

(c)

(d)

(e)

(f)

Figure 13(*to be continued*): Comparison between experimental data (dashed line) and FDS data (solid line) in case 3P [extinction model deactivated]. (a) Fuel mass loss rate; (b) MLR and BR in the simulation; (c) Vent flow rates (upper and lower vents); (d) FDS-based isocontour plot of mixture fraction in the central vertical plane; (e) Oxygen mole fraction (near floor and ceiling); (f) Carbon dioxide mole fraction (near floor and ceiling)

Fig.13 (d) shows the mixture fraction isocontours at an arbitrary time; the flame (defined as the interface between the black and light grey regions) is attached to the fuel pan and deflected towards the back wall, suggesting that the combustion in case 3 is still fuel-limited, but not as stable as in case 1P when the flame is attached above the burner.

Fig. 13(e) shows the oxygen mole fraction in the upper (ceiling) and lower (floor) layers. The experimental data predicts similar oxygen level in both layers, suggesting a well-mixed single-layer structure for the compartment gas. The compartment O2 mole fraction can go down as low as 2%, suggesting a certain level of air vitiation and an intermediate state between over-ventilation and under-ventilation conditions, although the BR curve above still shows all fuel ejected are burned. The numerical data agree well with the experiment in the ceiling layer but give a higher oxygen concentration near the floor.

Fig. 13(f, g) presents the CO_2 and CO mole fraction data. The CO_2 numerical predictions agree well with the experimental data, while the CO predictions are about 50 times lower than measured.

Fig. 13(h) presents the heat flux obtained at the center of the burner. The experimental data gives a heat flux per unit area of about 50 kW/m^2, and the numerical data gives a value around 30 kW/m^2. Both curves are showing a sudden decrease at about 270s, which is due to the sharp decrease in fuel mass loss rate.
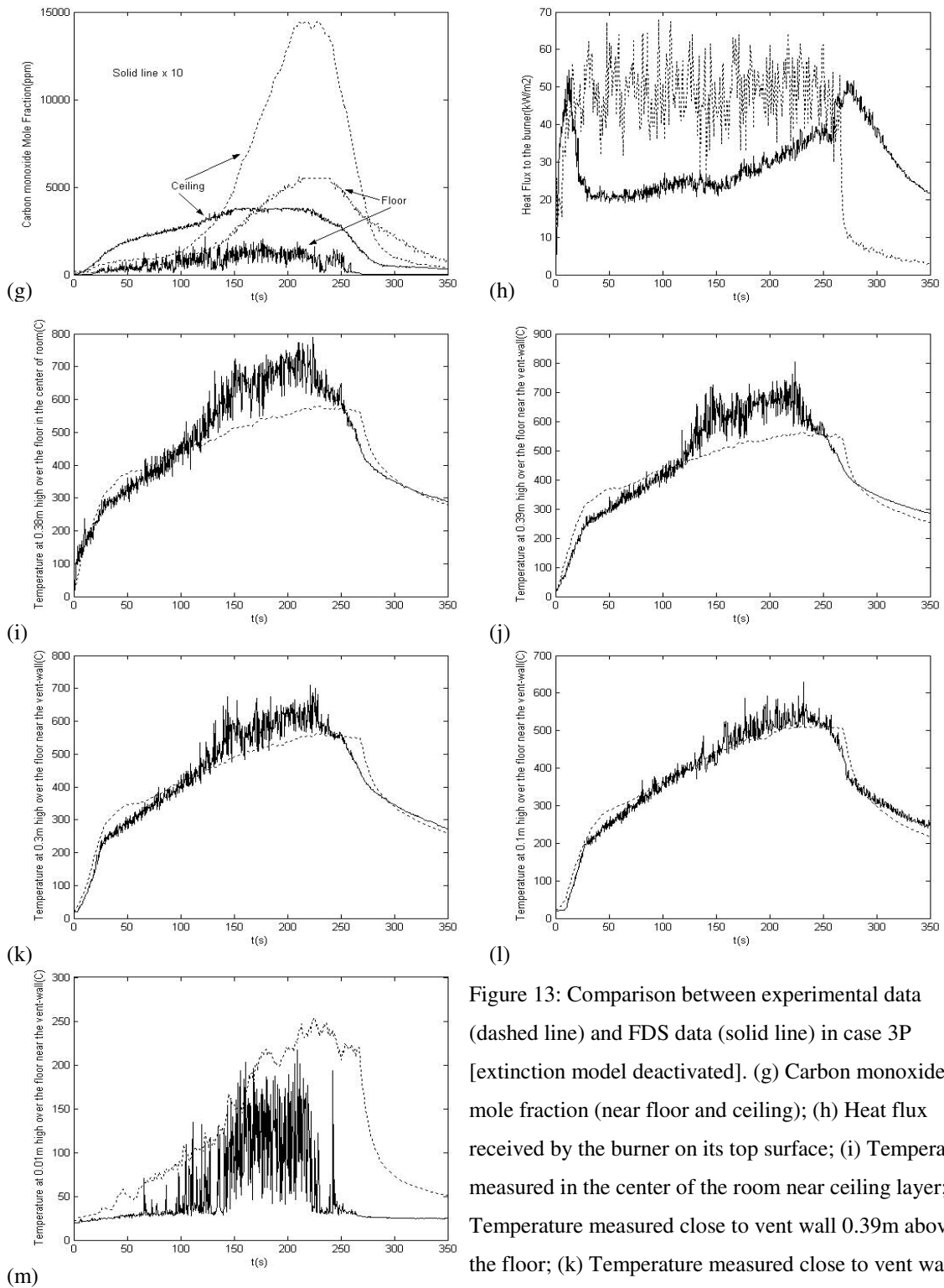
(g)

(h)

(i)

(j)

(k)

(l)

(m)

Figure 13: Comparison between experimental data (dashed line) and FDS data (solid line) in case 3P [extinction model deactivated]. (g) Carbon monoxide mole fraction (near floor and ceiling); (h) Heat flux received by the burner on its top surface; (i) Temperature measured in the center of the room near ceiling layer; (j) Temperature measured close to vent wall 0.39m above the floor; (k) Temperature measured close to vent wall 0.3m above the floor; (l) Temperature measured close to vent wall 0.1m above the floor; (m) Temperature measured close to vent wall 0.01m above the floor.

Fig. 13(i) presents the temperature obtained in the center of the room near the ceiling, while fig. 11(j-m) give the temperature along the vent wall from near ceiling to near floor. In this case, all simulated temperatures agree well with the experimental data.

4.4   Case 4P

Case 4 is selected as representative of regime R4 in which the combustion is fuel-rich and leads to complete flame extinction. Compared to case 1, the vent area in case 4 is decreased by a factor of sixty, whereas the fuel source area is unchanged. So the fire room equivalence ratio is estimated to be 12, which is ultra-rich. However, this ultra-rich condition is not observed, because flame extinction occurs before it reaches an overall fuel rich state. Fig. 14(a) shows the measured fuel mass loss rate per unit area in the experiment; the MLR goes down to very small value after 45s. Prior to extinction, the fuel mass loss rate per unit area is around 10 $g/m^2/s$, which is approximately equal to the estimated free-burn value (***Appendix I***).

Fig. 14(b) presents the burning rate (BR) per unit area compared to the MLR per unit area in the simulation; there is good agreement between BR and MLR. This shows that all the available fuel is burned in the fire room and the fire remains over-ventilated. We may also use the fuel mass loss rate and air mass flow rate to evaluate the fire room global equivalence, but in this case this would lead to an incorrect over-estimation due to the transient nature of the fire dynamics. Given the compartment size and using the value of MLR from Figure 14(a), one can show that a characteristic time to deplete the air

present in the fire room prior to ignition is about 80s (*details can be found in **Appendix II***); as a result, at t=45s, the fire room global equivalence ratio is much less than its steady state value, as estimated from the fuel and air mass flow rates.

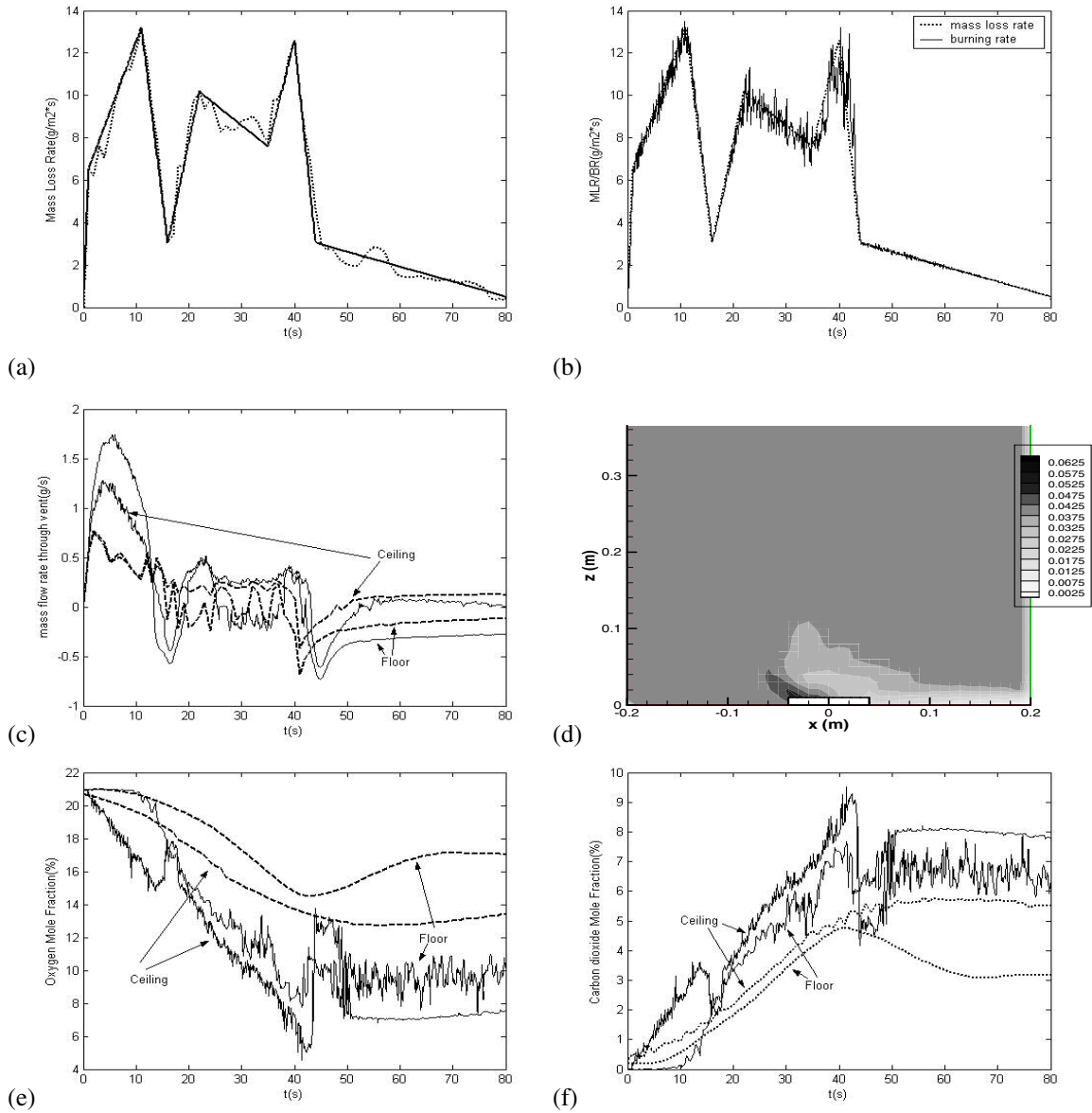(a)

(b)

(c)

(d)

(e)

(f)

Figure 14 (*to be continued*): Comparison between experimental data (dashed line) and FDS data (solid line) in case 4P [extinction model deactivated]. (a) Fuel mass loss rate; (b) MLR and BR in the simulation; (c) Vent flow rates (upper and lower vents); (d) FDS-based isocontour plot of mixture fraction in the central vertical plane; (e) Oxygen mole fraction (near floor and ceiling); (f) Carbon dioxide mole fraction (near floor and ceiling)

Fig. 14(c) presents the mass flow rates through the upper and lower vents. The numerical and experimental curves agree well, and both describe the short transient period after extinction, which corresponds to a sudden pressure drop inside the fire compartment and a subsequent inflow of air, through both the lower and upper vents.

Fig.14 (d) shows the mixture fraction isocontours before extinction; the flame is the interface between the black and light grey regions; the small flame is attached to the burner, which is similar to case 1, but weaker. The difference for this case is that the mixture fraction in the room is higher, suggesting a heavily vitiated oxidizer condition. There is still some air flows from the lower vent denoted by the white area.

Fig. 14(e) shows the oxygen mole fraction in the upper (ceiling) and lower (floor) layers. Experimental data give higher values than numerical ones. Both data sets still predict some significant amount of oxygen near the floor. Shortly after extinction, the pressure drop inside the room induces an inflow of air and a sudden increase of oxygen levels.

Fig. 14(f, g) presents the CO_2 and CO mole fractions data. Numerical data over-estimate CO_2 levels in both layers. The CO levels in the ceiling and floor layers are very close (applicable for both data sets). Note that the experimental measurements have a coarse 100 ppm resolution.
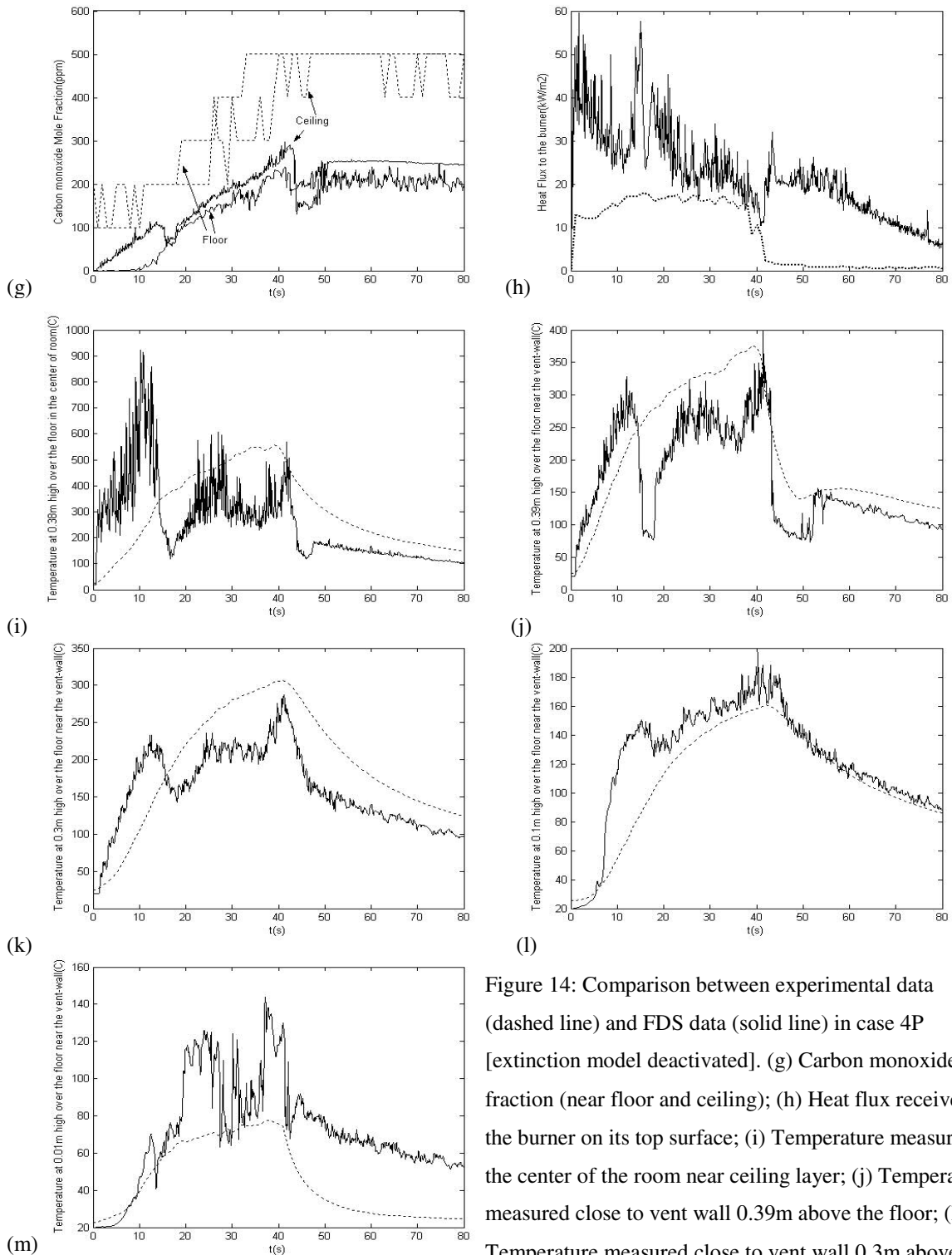
(g)

(h)

(i)

(j)

(k)

(l)

(m)

Figure 14: Comparison between experimental data (dashed line) and FDS data (solid line) in case 4P [extinction model deactivated]. (g) Carbon monoxide mole fraction (near floor and ceiling); (h) Heat flux received by the burner on its top surface; (i) Temperature measured in the center of the room near ceiling layer; (j) Temperature measured close to vent wall 0.39m above the floor; (k) Temperature measured close to vent wall 0.3m above the floor; (l) Temperature measured close to vent wall 0.1m above the floor; (m) Temperature measured close to vent wall 0.01m above the floor.

51

Fig. 14(h) presents the heat flux obtained at the center of the burner. At time $t \approx 45s$, flame extinction occurs, and the radiative feedback drops sharply, as seen in the experimental curve. This drop is not observed in the numerical curve because some level of combustion is still maintained. Fig. 14(i) presents the temperature obtained in the center of the room near the ceiling, while fig. 14(j-m) give the temperature along the vent wall from near ceiling to near floor. The agreement is fair.

Chapter IV: Simulation results compared against experiments
– calculating mass loss rate, extinction model deactivated

Next we consider the simulated cases in which the fuel mass loss rate is also the solution instead of being a prescribed input. While not required, the fuel supply is assumed to be infinite. The fire ignition source is removed 5 s after the simulation starts.

5.2   Case 1C

Fig. 15(a) shows the calculated fuel mass loss rate per unit area compared to the experimental one; both have an average value of about 20 g/m^2/s. Note that the calculated mass loss rate curve features a sudden drop at about t=145 s. If we look at fig. 15(c) and (e) we see that the oxygen at floor level and the air flow coming in through the lower vent correspond to well-ventilated conditions, which means that this observed jump in MLR is not due to insufficient air; it may be due to a decrease in the heat fed back to the burner. The temperature in the ceiling layer in Fig.15 (i) also has a similar jump at about the same time. The moment at which both mass loss rate and temperature in the ceiling jump is so close that we cannot determine which one is the cause or the effect. It would be valuable to check the heat flux at the burner location to get more information. However, apparently due to an error in FDS (this bug only happens for the calculated MLR cases), we fail to extract the heat flux data from the simulations. This is an issue that will be addressed in future work. In cases 1C-4C, the heat flux data are missing.

Fig. 15(b) gives the burning rate (BR) per unit area, which is found to follow the MLR per unit area; this means that the combustion is over-ventilated. Note that the peak observed before t=5s is due to the ignition source.
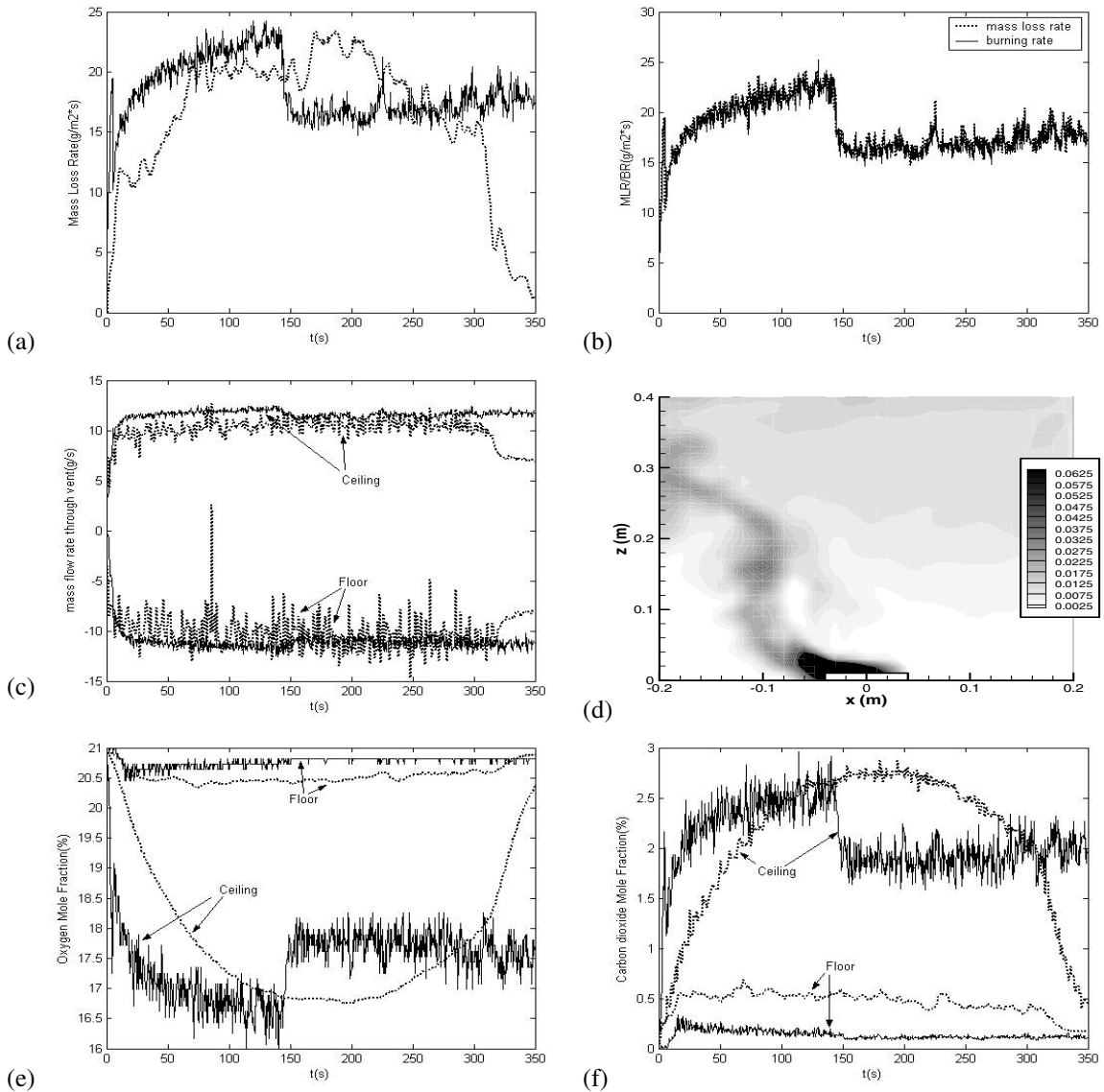

(a)

(b)

(c)

(d)

(e)

(f)

Figure 15 (*to be continued*): Comparison between experimental data (dashed line) and FDS data (solid line) in case 1C [extinction model deactivated]. (a) Fuel mass loss rate; (b) MLR and BR in the simulation; (c) Vent flow rates (upper and lower vents); (d) FDS-based isocontour plot of mixture fraction in the central vertical plane; (e) Oxygen mole fraction (near floor and ceiling); (f) Carbon dioxide mole fraction (near floor and ceiling)

Fig. 15(c) presents the mass flow rates through the upper and lower compartment vents. The calculated mass flow rates agree well with the experimental data, both give the rate of 10 g/s for the flow in and out of the compartment.

Fig.15 (d) shows the mixture fraction isocontours at an arbitrary time. The flame location is similar to that found in fig.11(d).

Fig. 15(e, f, g) show the O2, CO_2, CO mole fraction data at the upper (ceiling) and lower (floor) layers. The results are similar to figure 11, except for the jump in mixture composition in the ceiling layer, which is a consequence of the jump in mass loss rate seen in fig.15(a).

Fig. 15(h) presents the temperature obtained in the center of the room near the ceiling, while fig. 15(i-l) give the temperature along the vent wall from near ceiling to near floor. Similar to fig.11 in case 1P, FDS under-predict the temperature, especially near the lower vent, but the difference is less than 100ºC, and the comparison is found to be good in general.
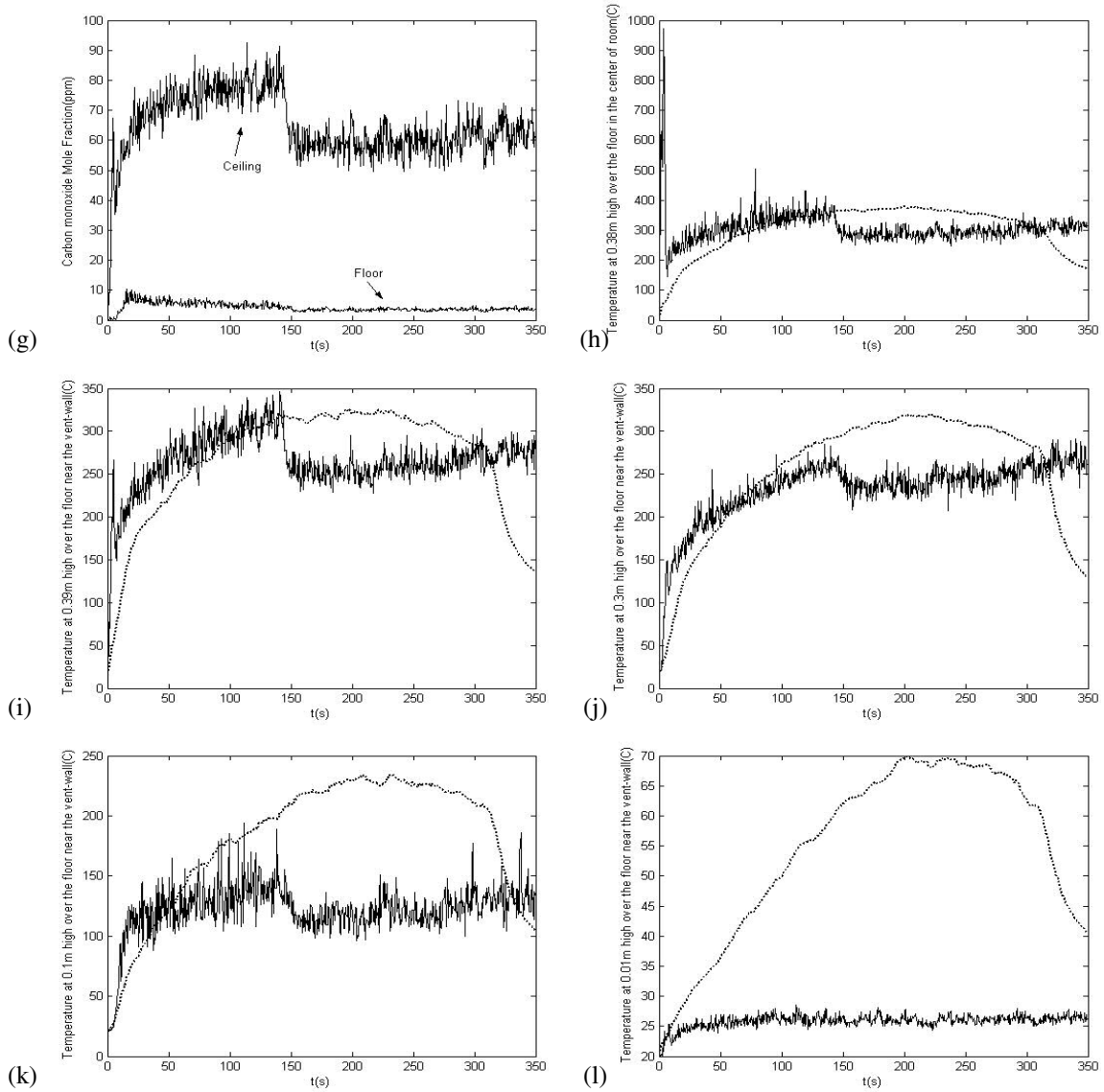
Figure 15: Comparison between experimental data (dashed line) and FDS data (solid line) in case 1C [extinction model deactivated]. (g) Carbon monoxide mole fraction (near floor and ceiling); (h) Temperature measured in the center of the room near ceiling layer; (i) Temperature measured close to vent wall 0.39m above the floor; (j) Temperature measured close to vent wall 0.3m above the floor; (k) Temperature measured close to vent wall 0.1m above the floor; (l) Temperature measured close to vent wall 0.01m above the floor.

56

5.2 Case 2C

Fig. 16 shows the FDS results obtained for case 2 with a calculated fuel mass loss rate. The duration of the simulation is still 250 s. As we can see in fig. 16(a), the experimental mass loss rate keeps steady at 20-25 $g/m^2/s$ until t=210 s when the fuel is depleted; in contrast, the simulated mass loss rate keeps increasing up to 35 $g/m^2/s$, and just starts to get steady when the simulation ends at 250s.

Fig. 16(b) gives the burning rate (BR) per unit area compared to the MLR per unit area in the simulation. The difference between BR and MLR indicates that the fire becomes under-ventilated (occurring at time t=50 s) and only a fraction of the vaporized fuel is actually burned in the fire room.

Fig. 16(c) presents the mass flow rates through the upper and lower compartment vents, the results are comparable to the predictions made in case 2P (in fig.12(c)). This simulation also fails to capture the large fluctuations at the lower vent observed in the experimental data at time t ≈ 50-90 s.

Fig.16 (d) shows the mixture fraction isocontours at an arbitrary time (the flame is the contour between the white and light grey regions). The flame is located between the burner and the lower vent.

Fig. 16(e) shows the O_2 mole fraction data at the upper (ceiling) and lower (floor) layer. Similar to the results obtained in case 2P, the oxygen and carbon dioxide predictions agree well with the experimental data. In particular, both data sets show that oxygen is depleted in the ceiling layer and very low in the floor layer, indicating under-ventilated conditions.
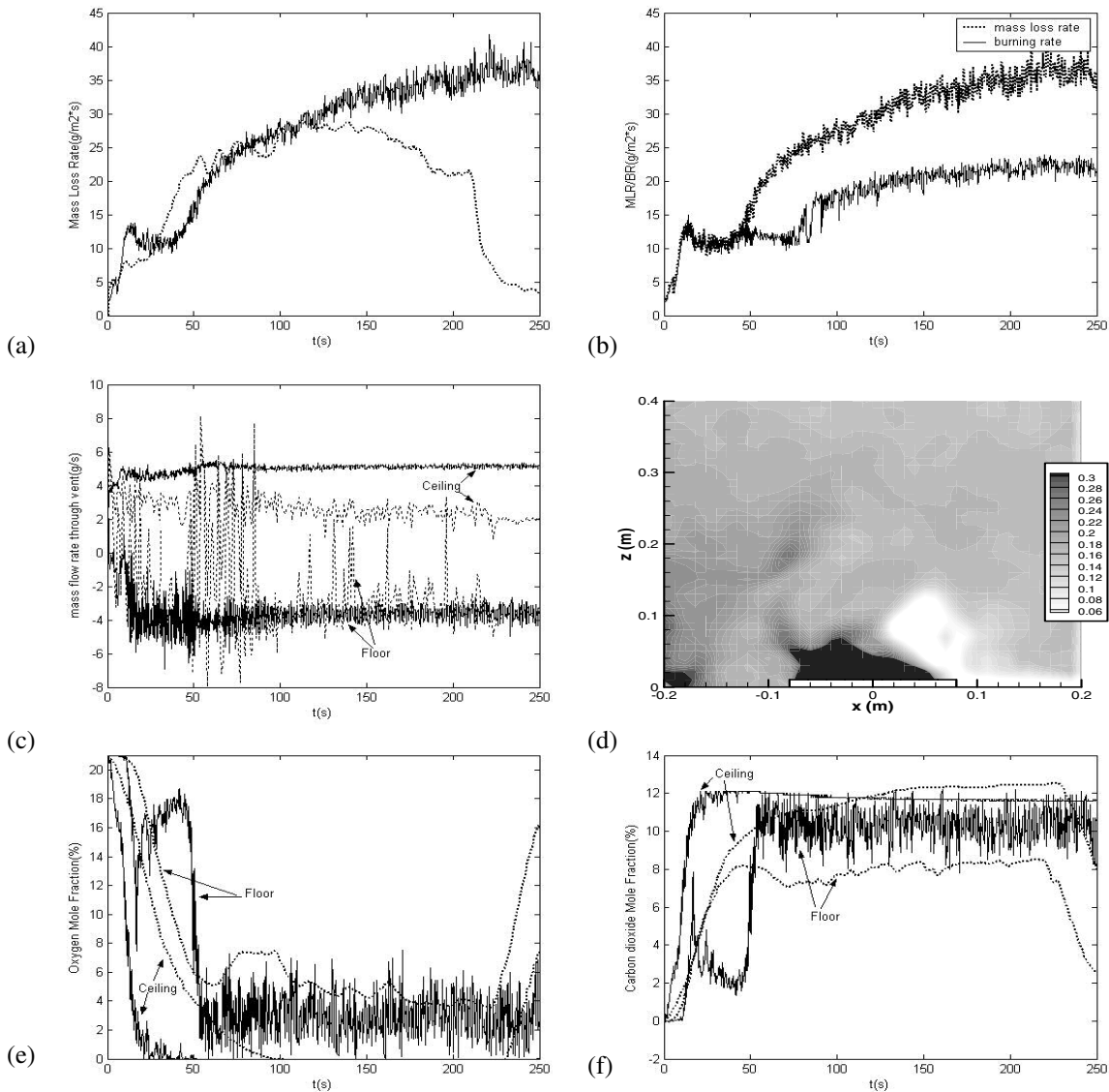

Figure 16 (*to be continued*): Comparison between experimental data (dashed line) and FDS data (solid line) in case 2C [extinction model deactivated]. (a) Fuel mass loss rate; (b) MLR and BR in the simulation; (c) Vent flow rates (upper and lower vents); (d) FDS-based isocontour plot of mixture fraction in the central vertical plane; (e) Oxygen mole fraction (near floor and ceiling); (f) Carbon dioxide mole fraction (near floor and ceiling)

Fig. 16(f, g) show the CO_2 and CO mole fraction data at the upper (ceiling) and lower (floor) layers. While CO_2 is calculated to be at the same level as in the experiment, CO predictions are still much lower than experimental data.
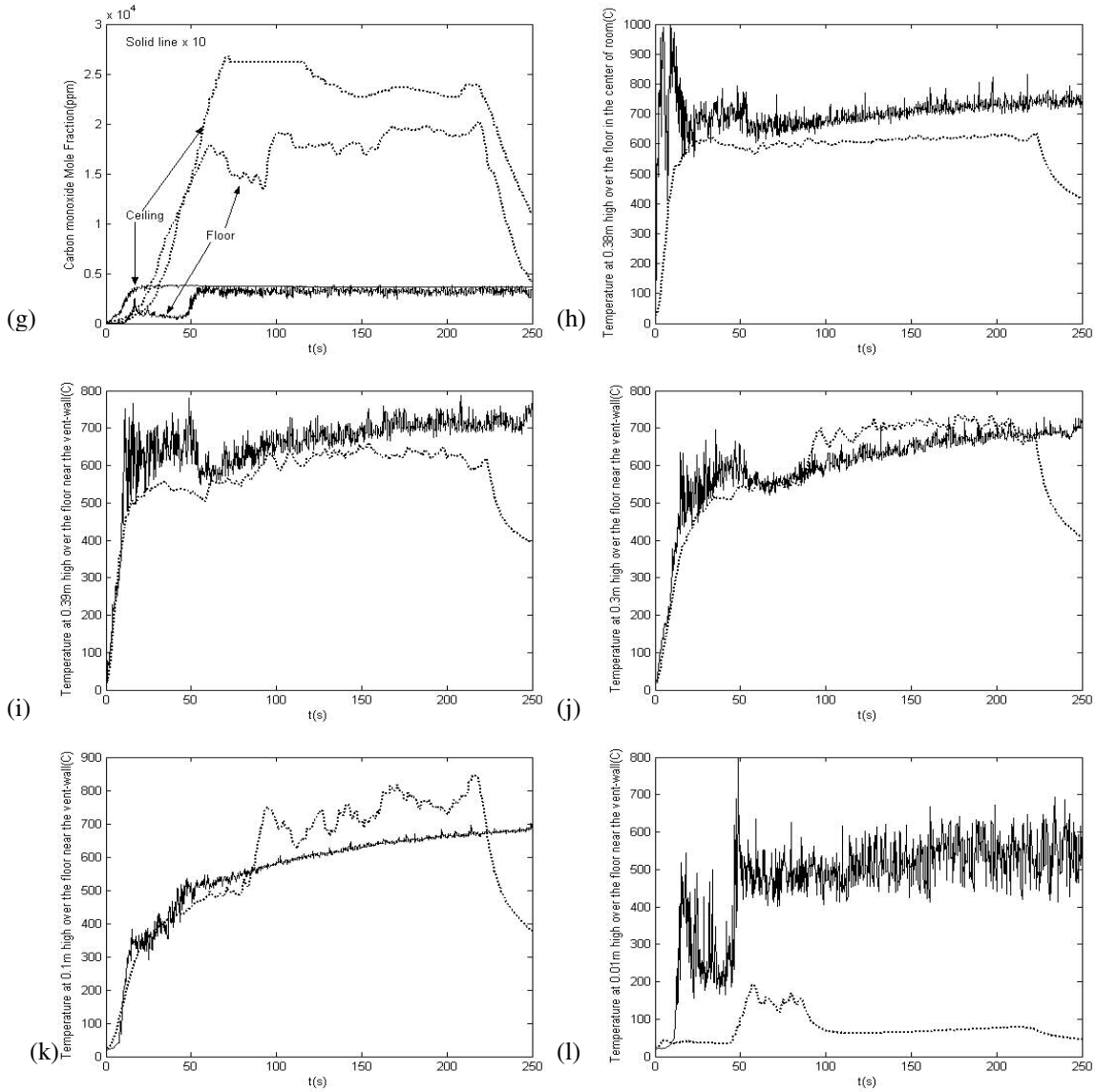

Figure 16: Comparison between experimental data (dashed line) and FDS data (solid line) in case 2C [extinction model deactivated]. (g) Carbon monoxide mole fraction (near floor and ceiling); (h) Temperature measured in the center of the room near ceiling layer; (i) Temperature measured close to vent wall 0.39m above the floor; (j) Temperature measured close to vent wall 0.3m above the floor; (k) Temperature measured close to vent wall 0.1m above the floor; (l) Temperature measured close to vent wall 0.01m above the floor.

Fig. 16(h) presents the temperature obtained at the center of the room near the ceiling, while fig. 16(i-l) give the temperature along the vent wall from near ceiling to near floor. The numerical results agree well with the experimental data except at the floor location, which gives temperature levels 400 ºC higher than the ones measured in the experiment, in part because the flame moves close to the vent.

5.3   Case 3C

We now consider case 3C. Fig.17(a) presents the evolution of the fuel mass loss rate per unit area; the numerical simulation gives an average value of 15 $g/m^2/s$, which is much less than the experimental average value, 30 $g/m^2/s$. Also, a sudden drop in MLR is observed near the end of the simulation. The reason for this drop remains unknown and will be explored in a future study.

As mentioned in case 3P, the global stoichiometric ratio is about 1 for case 3. Fig.17(b) confirms that the combustion remains fuel-limited in this case.

Fig. 17(c) presents the mass flow rates through the upper and lower compartment vents. While the FDS simulation provides acceptable average values, it does not capture the large fluctuations observed in the experiment. This observation is similar to that made in case 3P (figure 13(c)).

Fig.17 (d) shows a snapshot of the mixture fraction isocontours at an arbitrary time, and similar to case 3P, the flame is still attached to the burner with a strong deflection towards the back wall.
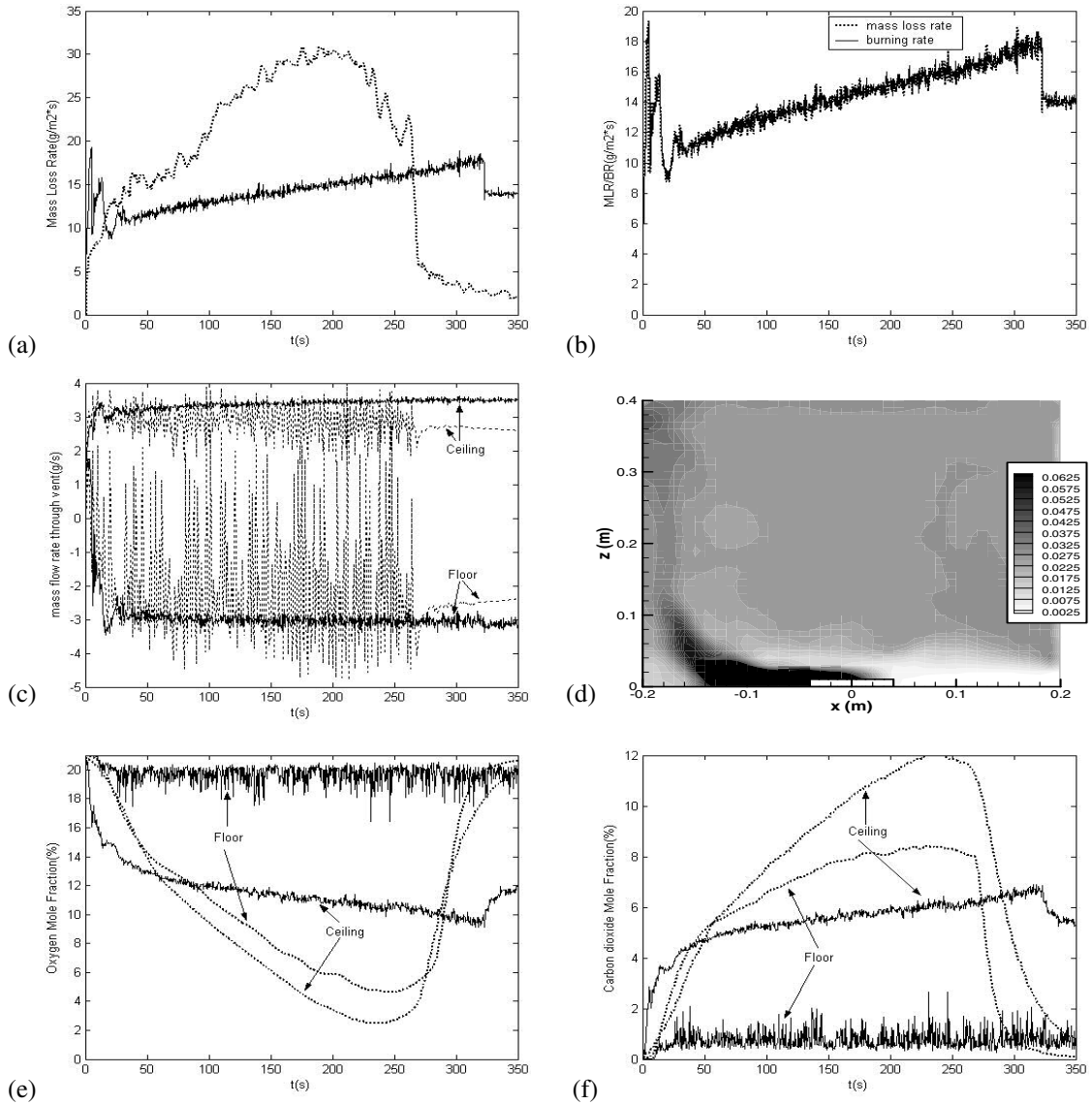

Figure 17 (*to be continued*): Comparison between experimental data (dashed line) and FDS data (solid line) in case 3C [extinction model deactivated]. (a) Fuel mass loss rate; (b) MLR and BR in the simulation; (c) Vent flow rates (upper and lower vents); (d) FDS-based isocontour plot of mixture fraction in the central vertical plane; (e) Oxygen mole fraction (near floor and ceiling); (f) Carbon dioxide mole fraction (near floor and ceiling)
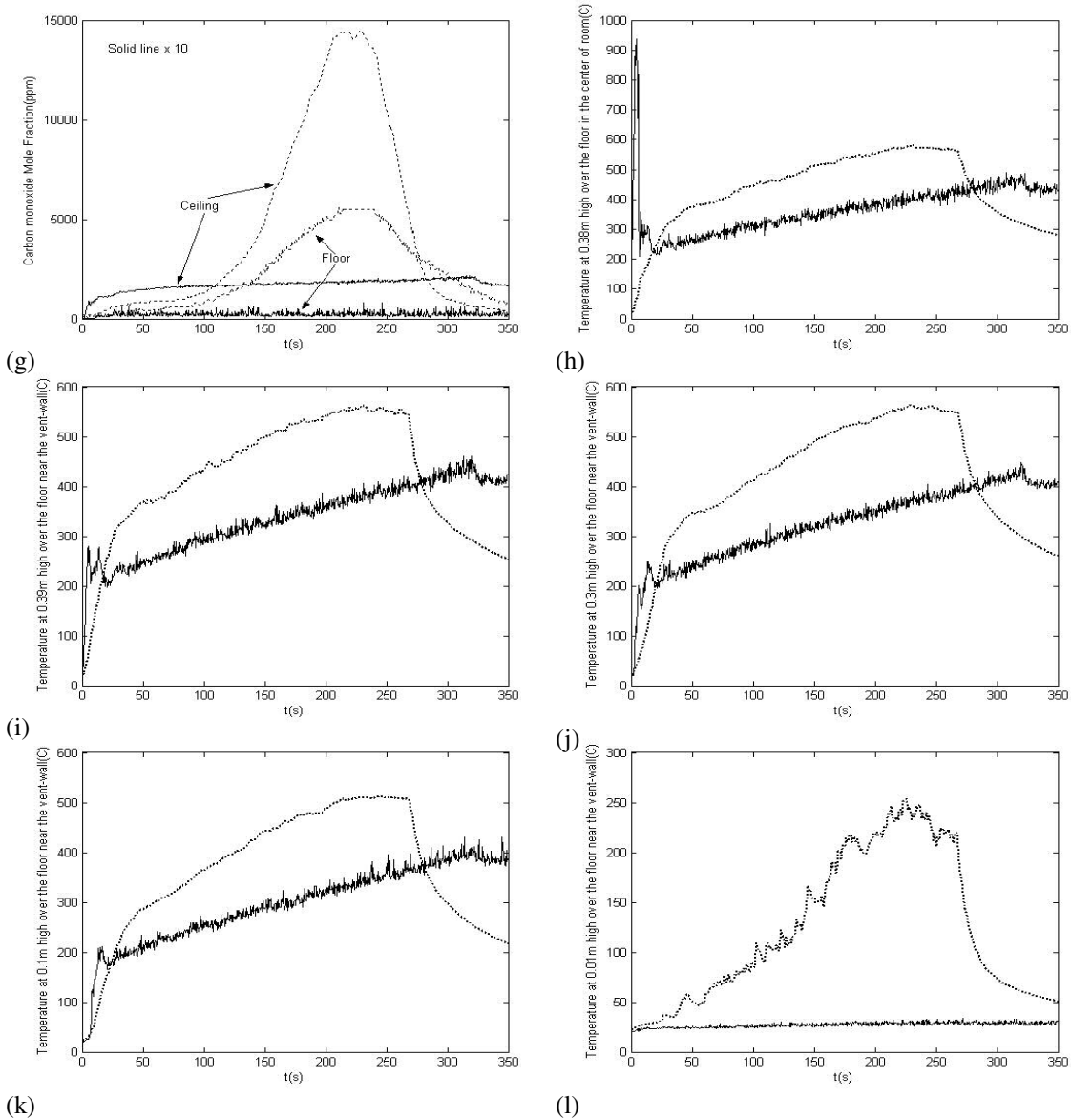
(g)

(h)

(i)

(j)

(k)

(l)

Figure 17: Comparison between experimental data (dashed line) and FDS data (solid line) in case 3C [extinction model deactivated]. (g) Carbon monoxide mole fraction (near floor and ceiling); (h) Temperature measured in the center of the room near ceiling layer; (i) Temperature measured close to vent wall 0.39m above the floor; (j) Temperature measured close to vent wall 0.3m above the floor; (k) Temperature measured close to vent wall 0.1m above the floor; (l) Temperature measured close to vent wall 0.01m above the floor.

Fig. 17(e) shows the oxygen mole fractions in the upper (ceiling) and lower (floor) layers. Consistent with the under-prediction of MLR seen in figure 17(a), the predicted

oxygen levels are now over-estimated. Similarly, in fig.17(f), the CO_2 levels are under-predicted.

Fig. 17(g) presents the CO mole fraction data. Compared to the experimental data, the calculated CO levels are again highly under predicted.

Fig. 17(h) presents the temperature obtained at the center of the room near the ceiling, while fig. 17(i-l) give the temperature along the vent wall from near ceiling to near floor. The difference between measured and calculated temperatures is larger than in case 3P because a lower amount of fuel is burned this time. In general, the temperatures are under-predicted.

5.4   Case 4C

Case 4 has the smallest vent and total flame extinction occurs in the experiment. The simulation of case 4C is performed to examine the calculated fuel mass loss rate. Before extinction occurs, we see a decrease in MLR which would lead to an asymptotic extinction even when no extinction model is adopted. This is viewed as an encouraging result. As shown in fig. 18(a), the calculated fuel mass loss rate agrees with the experimental data quantitatively.

Fig. 18(b) shows that BR and MLR are equivalent, suggesting that before extinction, the burning is fuel-limited. It still have the big jump at t=5s due to bigger power fire source put above the pool.
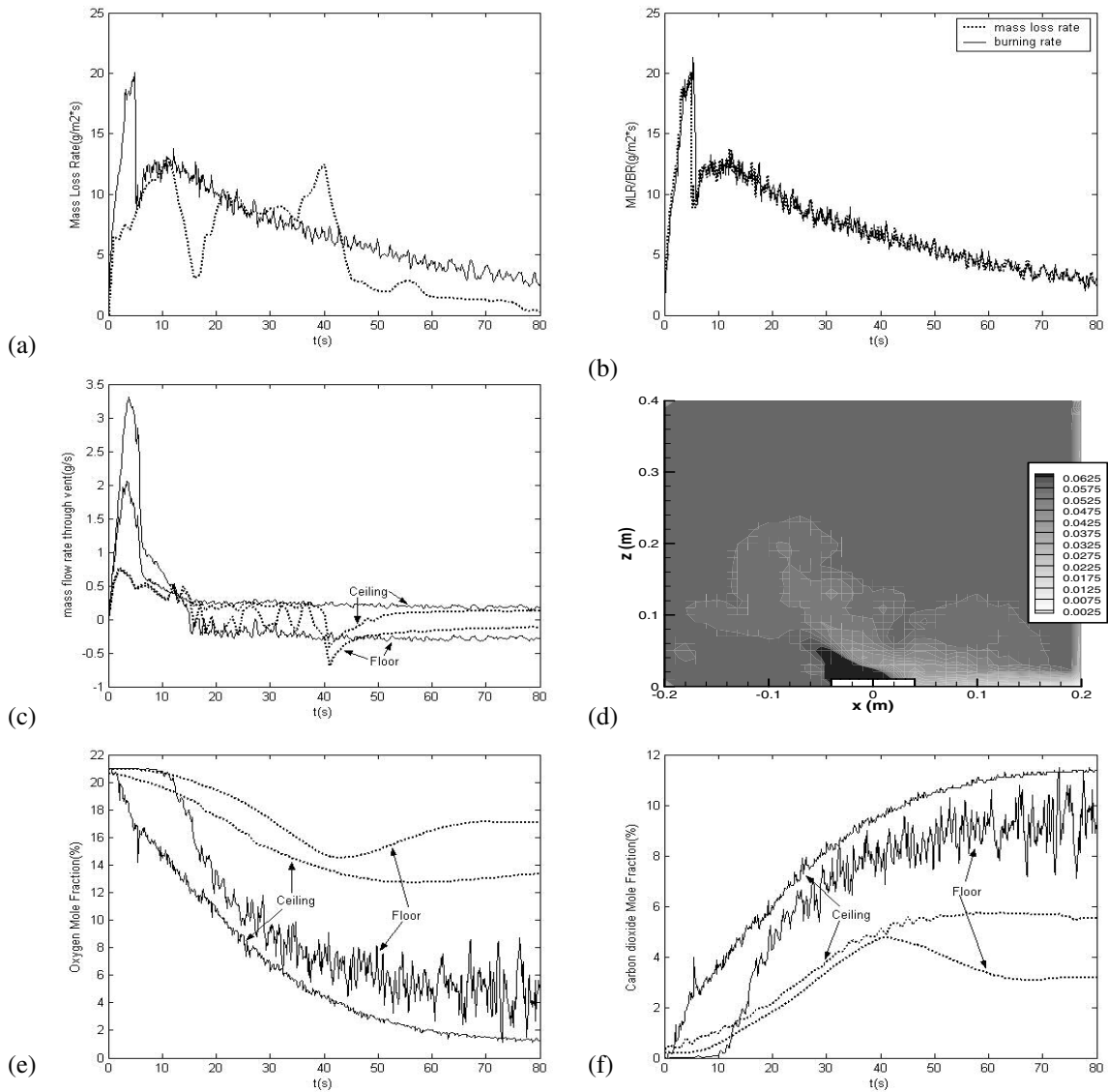
Figure 18(*to be continued*): Comparison between experimental data (dashed line) and FDS data (solid line) in case 4C [extinction model deactivated]. (a) Fuel mass loss rate; (b) MLR and BR in the simulation; (c) Vent flow rates (upper and lower vents); (d) FDS-based isocontour plot of mixture fraction in the central vertical plane; (e) Oxygen mole fraction (near floor and ceiling); (f) Carbon dioxide mole fraction (near floor and ceiling)

Fig. 18(c) presents the mass flow rates through the upper and lower compartment vents. The numerical data agree well with the experimental data, with the vent flow rates at about 0.3 g/s.

64

Fig.18 (d) shows the mixture fraction isocontours at a time taken after 40s; the simulated flame is not extinguished even though the mass loss rate is decreased to low levels, we can see a small flame attached to burner (between the black and light grey regions).

Fig. 18(e) shows the oxygen mole fractions in the upper (ceiling) and lower (floor) layers. The numerical simulation under-predicts the oxygen levels. Fig. 18(f, g) presents the CO_2 and CO mole fraction data. The numerical simulation over-predicts the CO_2 levels. Both data sets suggest a semi-uniform room environment.

Fig. 18(h) presents the temperature obtained at the center of the room near the ceiling, while fig. 18(i-l) give the temperature along the vent wall from near ceiling to near floor. The simulated temperatures compare favorably to the measurements, up to the extinction point. After extinction, the temperatures are over-estimated by FDS.
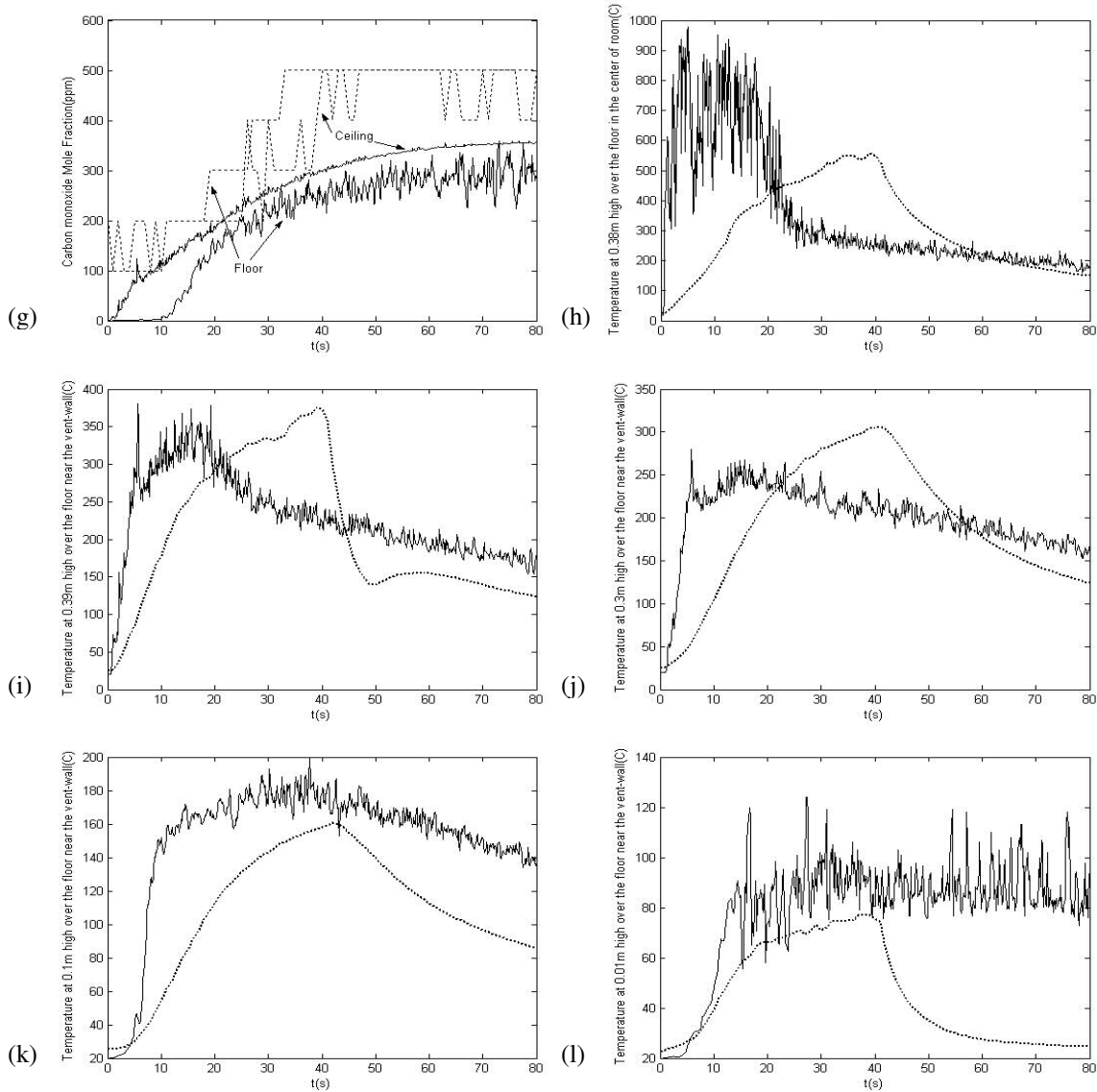
Figure 18: Comparison between experimental data (dashed line) and FDS data (solid line) in case 4C [extinction model deactivated]. (g) Carbon monoxide mole fraction (near floor and ceiling); (h) Temperature measured in the center of the room near ceiling layer; (i) Temperature measured close to vent wall 0.39m above the floor; (j) Temperature measured close to vent wall 0.3m above the floor; (k) Temperature measured close to vent wall 0.1m above the floor; (l) Temperature measured close to vent wall 0.01m above the floor.

66

Chapter VI. Simulation results compared against experiments

--- prescribing mass loss rate, with extinction model

In the following we will activate the flame extinction model introduced previously and

redo all above cases to highlight the differences. Plots will be shown in the same

sequence and not every picture will be explained if there is not much difference with the

previous extinction-free simulations.

6.1   *Case 1p*

Case 1 is a well-ventillated case and no extinction (local or global) occurs; so the

extinction model is not getting involved and the effect of the modification is negligible.

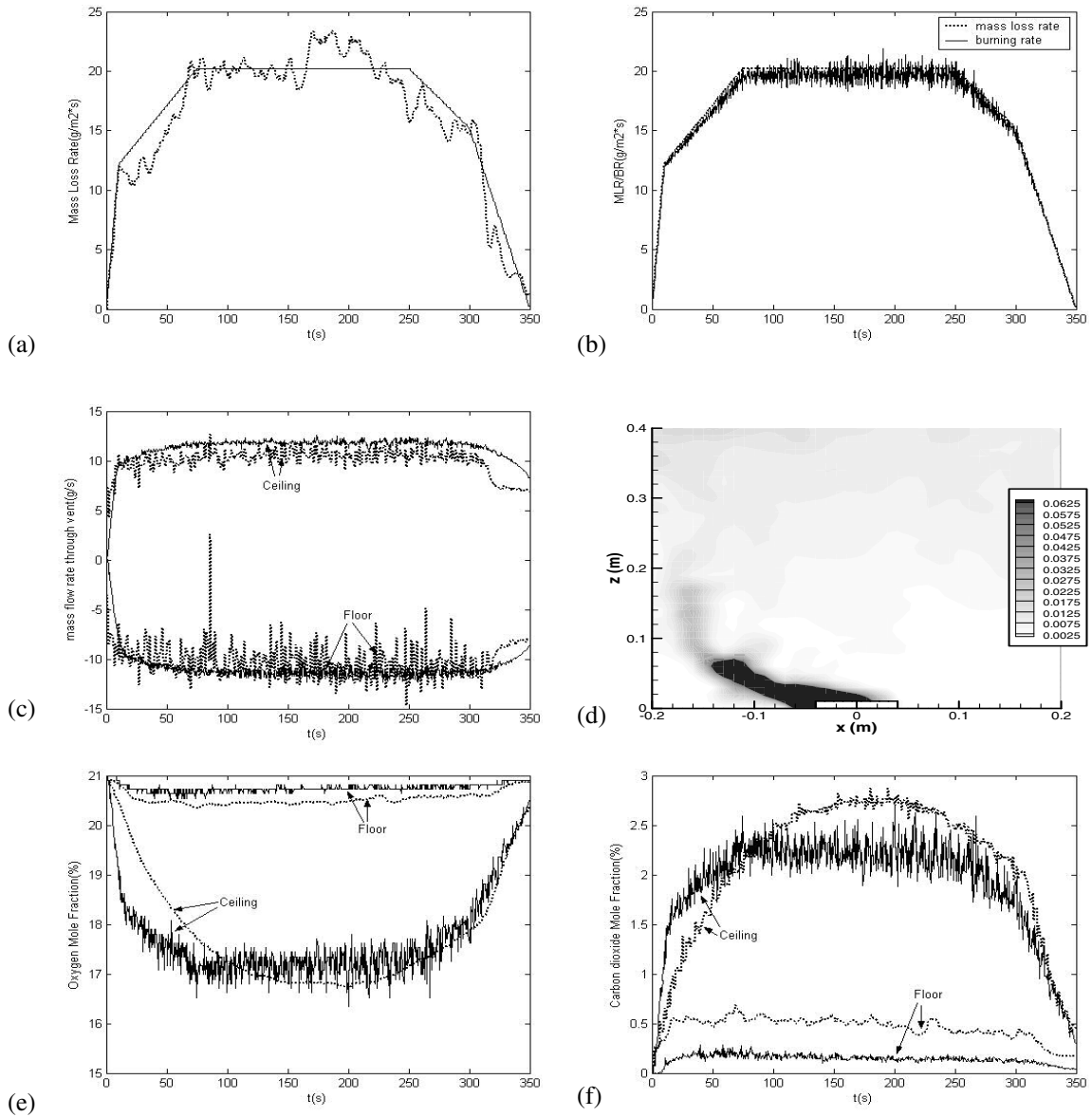The levels in fig.19 are similar to those presented in fig.11.

(a)

(b)

(c)

(d)

(e)

(f)

Figure 19 (*to be continued*): Comparison between experimental data (dashed line) and FDS data (solid line) in case 1P [extinction model activated]. (a) Fuel mass loss rate; (b) MLR and BR in the simulation; (c) Vent flow rates (upper and lower vents); (d) FDS-based isocontour plot of mixture fraction in the central vertical plane; (e) Oxygen mole fraction (near floor and ceiling); (f) Carbon dioxide mole fraction (near floor and ceiling)
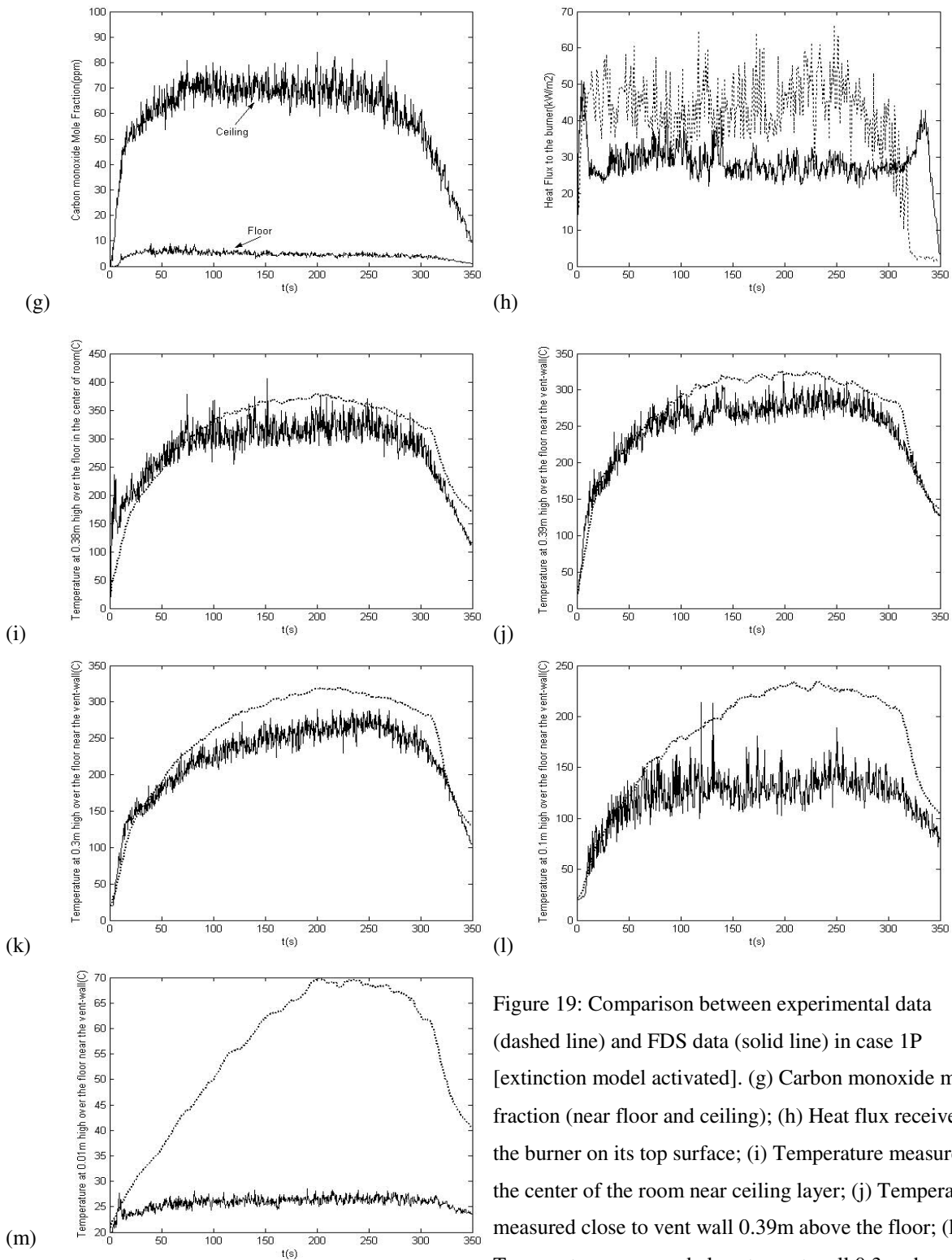
(g)

(h)

(i)

(j)

(k)

(l)

(m)

Figure 19: Comparison between experimental data (dashed line) and FDS data (solid line) in case 1P [extinction model activated]. (g) Carbon monoxide mo fraction (near floor and ceiling); (h) Heat flux received the burner on its top surface; (i) Temperature measured the center of the room near ceiling layer; (j) Temperatu measured close to vent wall 0.39m above the floor; (k) Temperature measured close to vent wall 0.3m above t floor; (l) Temperature measured close to vent wall 0.1r above the floor; (m) Temperature measured close to ve wall 0.01m above the floor;

69

6.2   Case 2P

The results for case 2P are presented in fig.20. Compared to results presented in fig.12, the new predictions indicate a newly observed tendency towards extinction at time $t \approx 30$-40s, as we can see in fig.20(b). This tendency occurs as the flame experiences a transition from over- to- under-ventilated conditions. In case 2P, the flame is able to survive through this transition and successfully establishes steady under-ventilated burning conditions.

There is another difference between fig.12(b) and fig.20(b). At time $t \approx 230$s, when the prescribed mass loss rate is decreased, the fire shows another tendency to extinguish.

Two jumps in the heat flux data in fig.20(h) can be seen consistent with tendencies towards extinction, while one jump is observed in the temperature data in fig.20(i-m) corresponding to the first extinction tendency. The mass flow rates through the vents and the species data are almost unaffected by the extinction model.
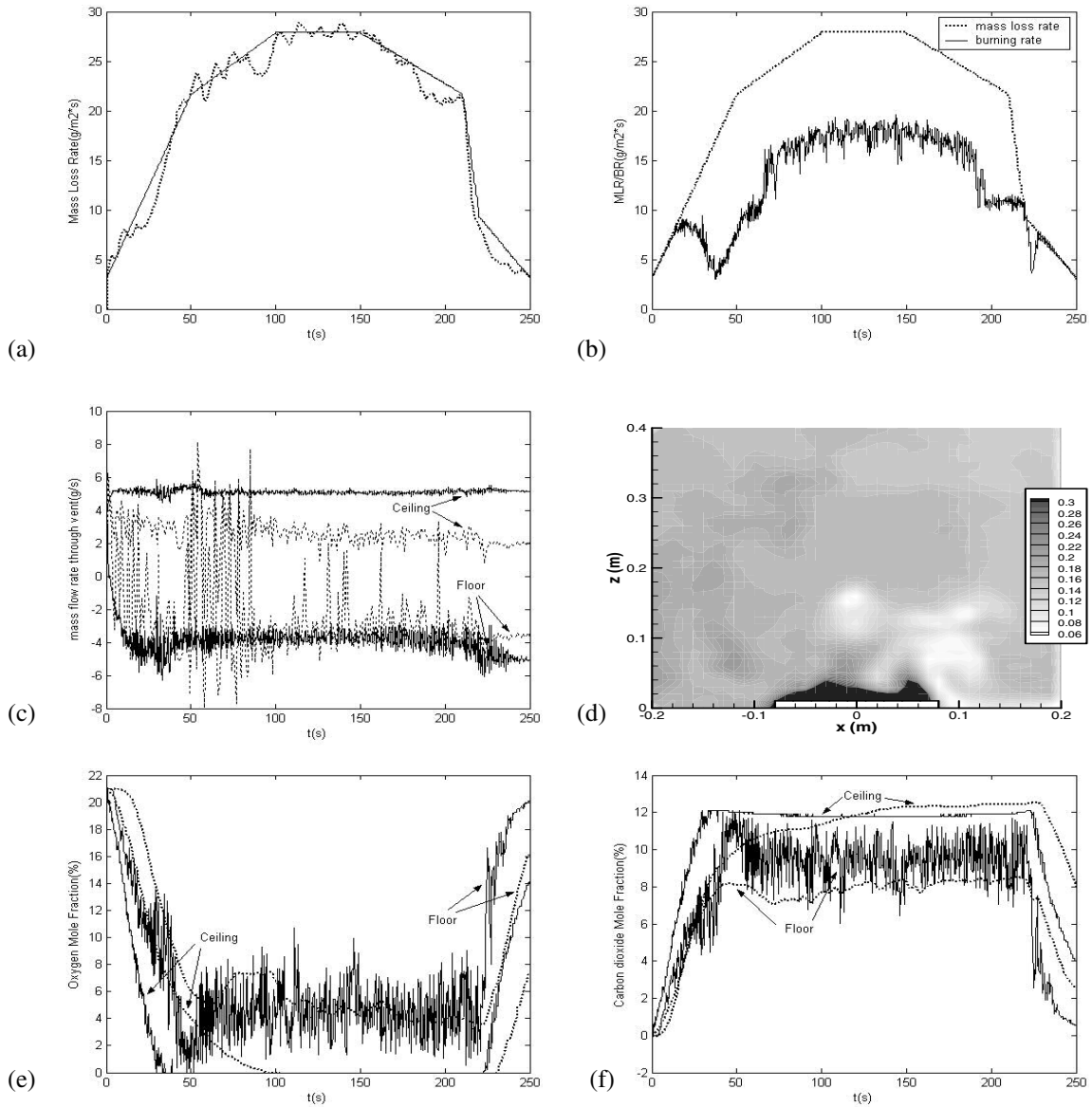
Figure 20 (*to be continued*): Comparison between experimental data (dashed line) and FDS data (solid line) in case 2P [extinction model activated]. (a) Fuel mass loss rate; (b) MLR and BR in the simulation; (c) Vent flow rates (upper and lower vents); (d) FDS-based isocontour plot of mixture fraction in the central vertical plane; (e) Oxygen mole fraction (near floor and ceiling); (f) Carbon dioxide mole fraction (near floor and ceiling)
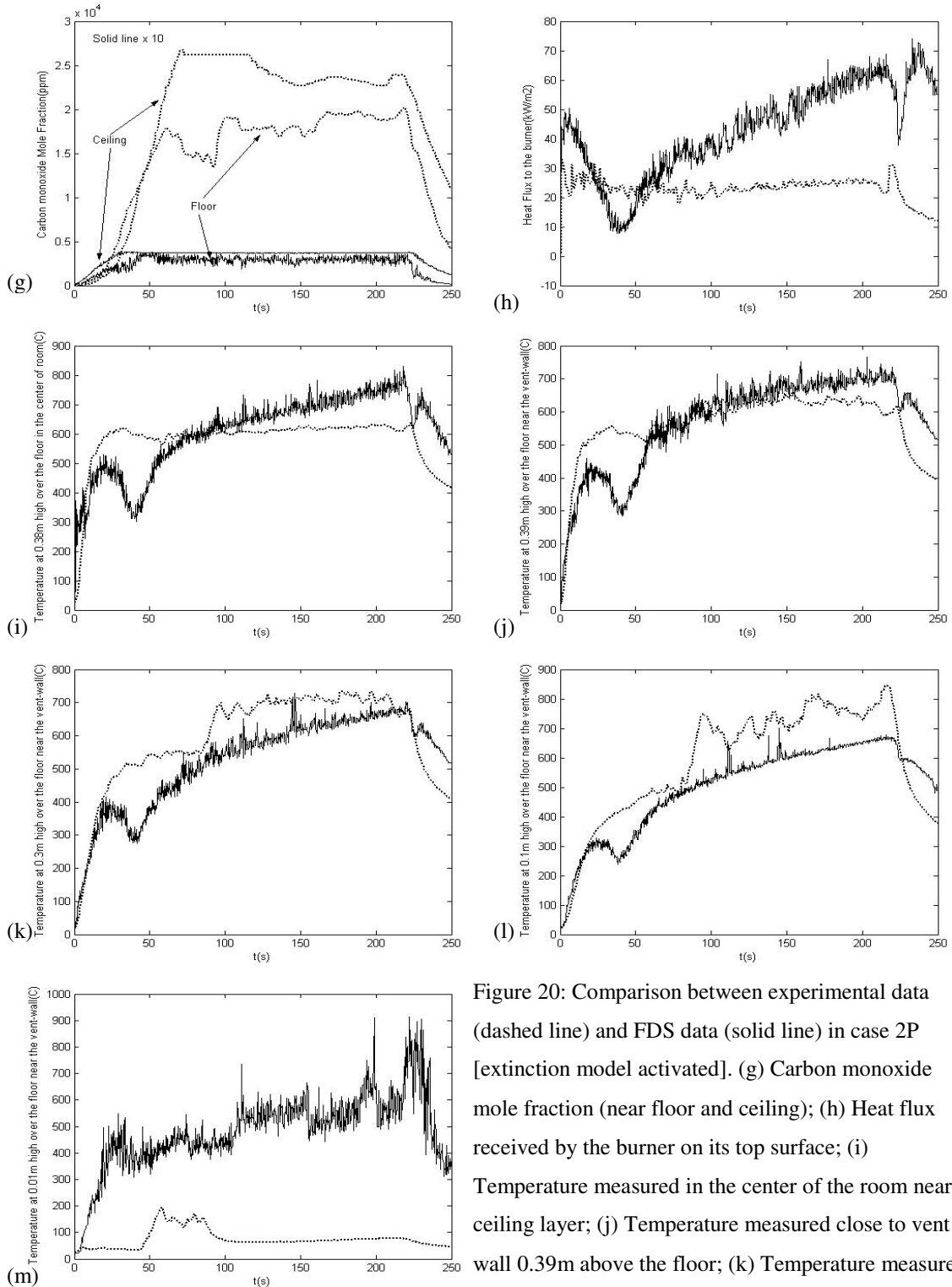
Figure 20: Comparison between experimental data (dashed line) and FDS data (solid line) in case 2P [extinction model activated]. (g) Carbon monoxide mole fraction (near floor and ceiling); (h) Heat flux received by the burner on its top surface; (i) Temperature measured in the center of the room near ceiling layer; (j) Temperature measured close to vent wall 0.39m above the floor; (k) Temperature measured close to vent wall 0.3m above the floor; (l) Temperature measured close to vent wall 0.1m above the floor; (m) Temperature measured close to vent wall 0.01m above the floor;

72

6.3   Case 3P

Case 3 is typical of regime R3 which features large flame oscillations and periodic flame extinction and re-ignition. The global equivalence ratio is nearly 1. Figure 21 presents the new predictions for case 3P. The difference between fig.21(b) and fig.13(b) is striking. Although the global equivalence ratio is nearly unity; local flame extinctions decrease the burning rate to extremely small values. At time $t \approx 200s$, the flame is almost totally extinguished. The peak in BR that occurs later at $t \approx 250s$ is the result of the prescribed decrease in MLR, which helps to take the flame back to over-ventilated conditions. The heat flux to the burner and all temperature data are affected by the partial flame extinction, while the vent flow rates and species data remain almost unchanged.

The temperatures calculated here are under-predicted, which suggests that flame extinction might be over-predicted in this case.
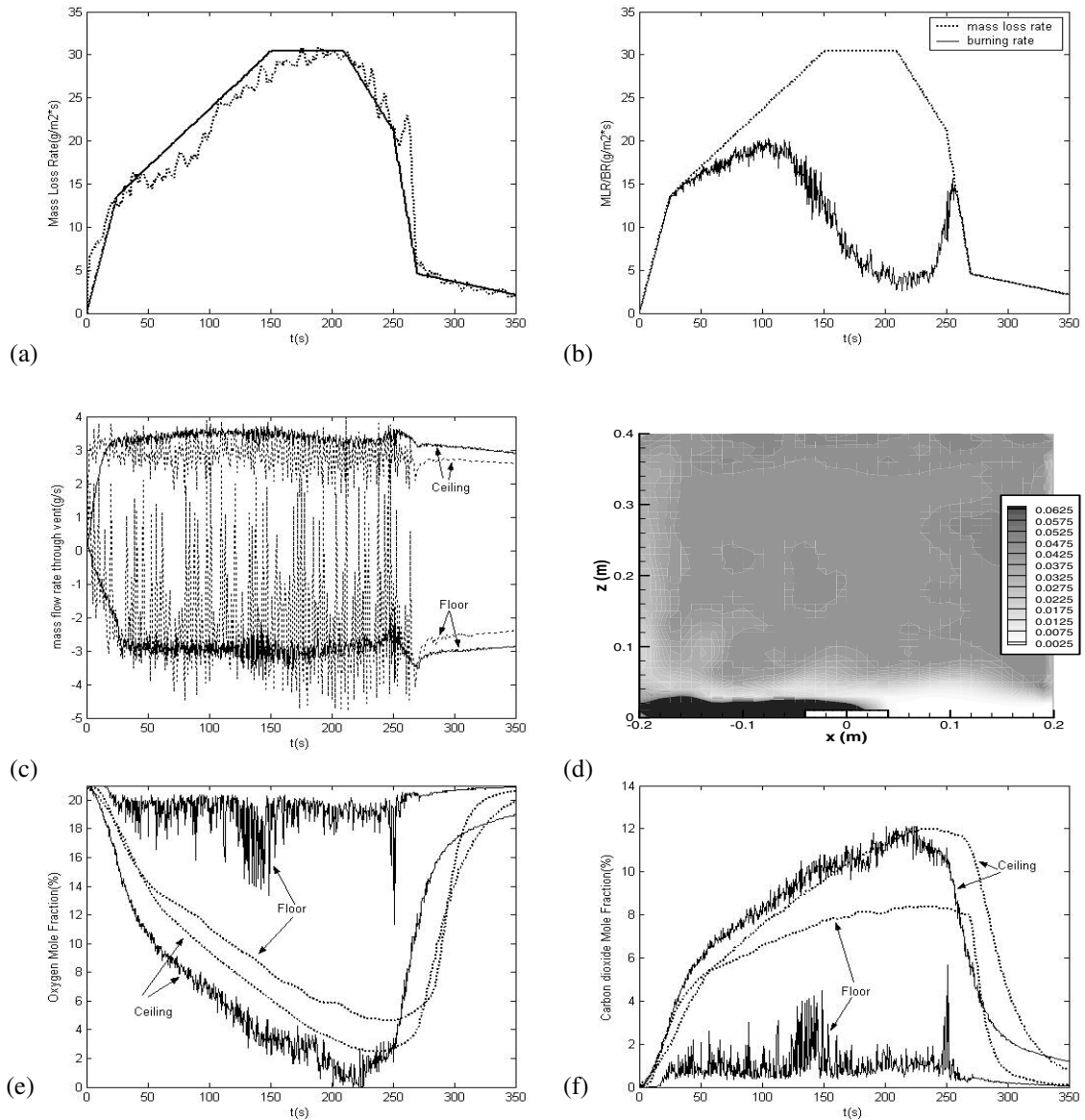
Figure 21 2(*to be continued*): Comparison between experimental data (dashed line) and FDS data (solid line) in case 3P [extinction model activated]. (a) Fuel mass loss rate; (b) MLR and BR in the simulation; (c) Vent flow rates (upper and lower vents); (d) FDS-based isocontour plot of mixture fraction in the central vertical plane; (e) Oxygen mole fraction (near floor and ceiling); (f) Carbon dioxide mole fraction (near floor and ceiling)
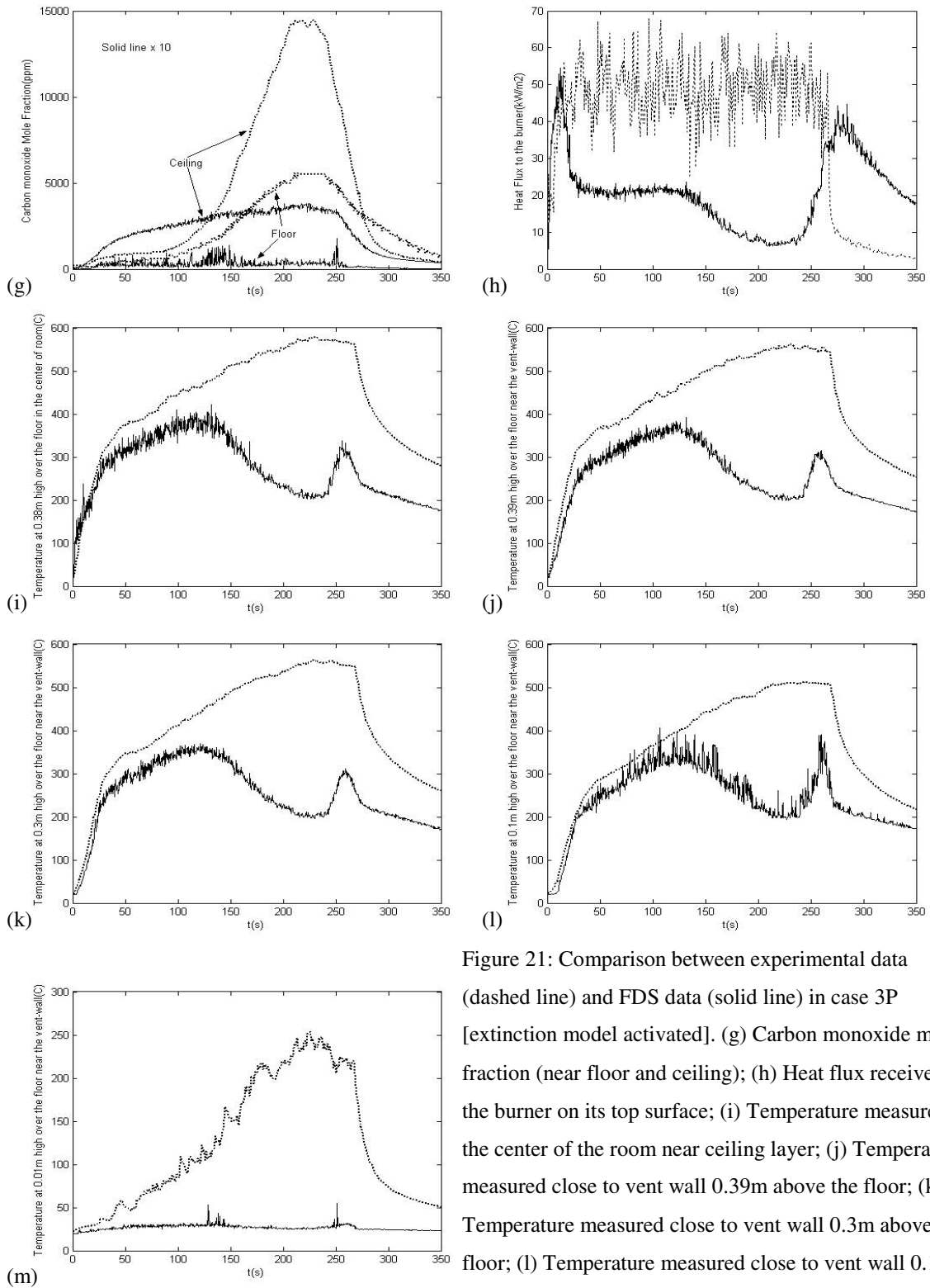
(g)

(h)

(i)

(j)

(k)

(l)

(m)

Figure 21: Comparison between experimental data (dashed line) and FDS data (solid line) in case 3P [extinction model activated]. (g) Carbon monoxide mole fraction (near floor and ceiling); (h) Heat flux received by the burner on its top surface; (i) Temperature measured in the center of the room near ceiling layer; (j) Temperature measured close to vent wall 0.39m above the floor; (k) Temperature measured close to vent wall 0.3m above the floor; (l) Temperature measured close to vent wall 0.1m above the floor; (m) Temperature measured close to vent wall 0.01m above the floor;

75

6.4   Case 4P

Case4 corresponds to fuel ultra-rich conditions, but as discussed in chapter III, the
flame dynamics take place during a transient phase that remains over-ventilated. Case 4 is
now simulated with the new flame extinction capability. In fig. 22(b) we see that BR is
deviating from MLR after time t = 20s and sharply decreases to zero at about t = 42 s,
exhibiting a total flame extinction.

Fig. 22(c) presents the mass flow rates through the upper and lower compartment
vents, which are not much different from the results presented in fig. 14. Whether or not
extinction happens, the mass flow rates through the vents are very low.

Fig.22 (d) shows a snapshot of the mixture fraction isocontours at the time after
extinction happens. The mixture is quasi-homogeneous in the compartment and the flame
is absent.

Fig. 22(e, f, g) shows the O_2, CO_2 and CO mole fractions in the upper (ceiling) and
lower (floor) layers; the results are similar to those presented in fig. 14.

Fig. 22(h) presents the heat flux at the center of the burner. Compared to fig.14(h), this
heat flux decreases quickly to low values after time t = 42s, due to global flame
extinction.

Fig. 22(i) presents the temperature measured in the center of the room near the ceiling, while fig. 22(j-m) give the temperature along the vent wall from near ceiling to near floor. Temperatures are lower than the temperatures predicted in the corresponding case without the extinction model in fig. 14.
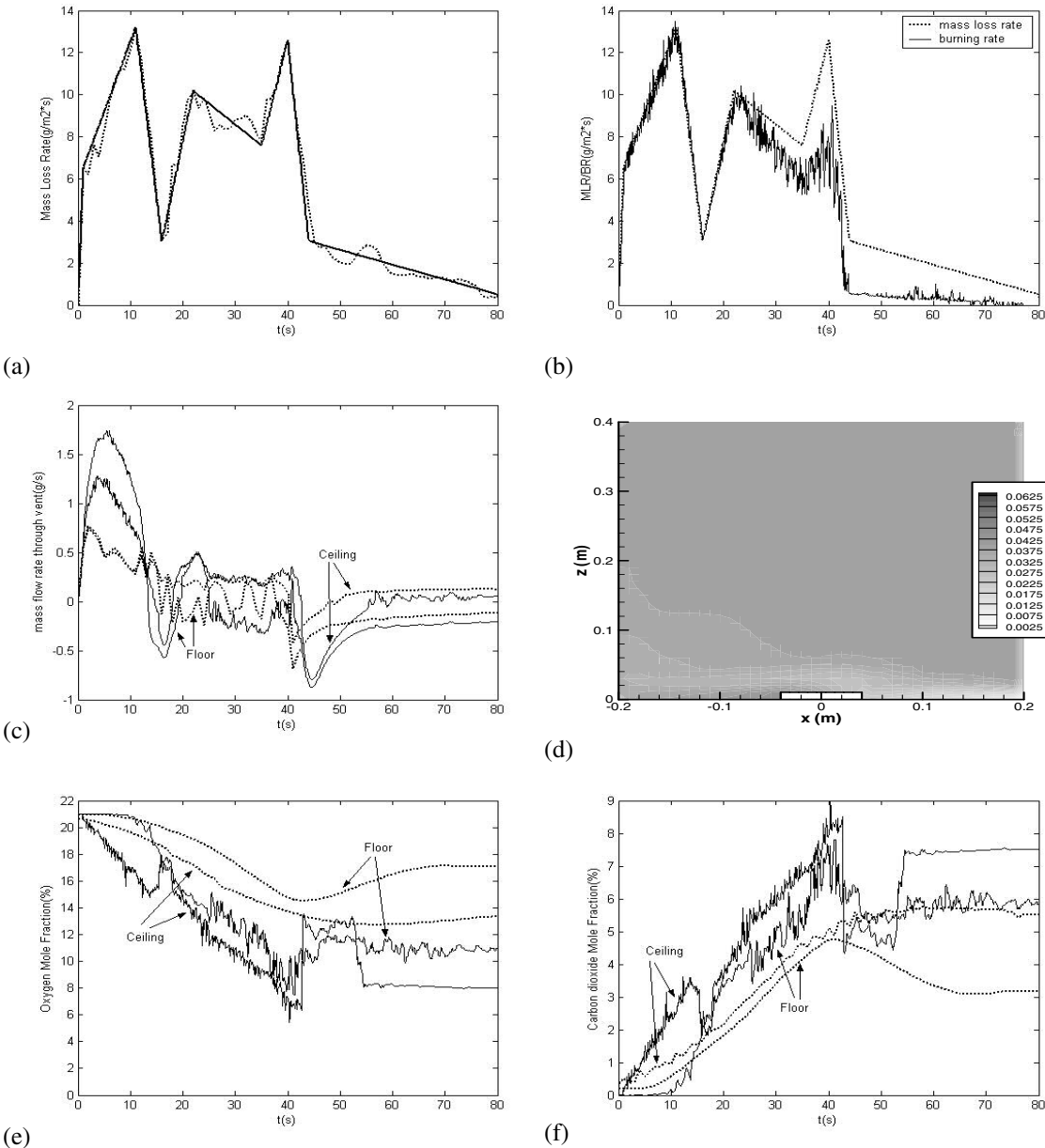

(a)

(b)

(c)

(d)

(e)

(f)

Figure 22 (*to be continued*): Comparison between experimental data (dashed line) and FDS data (solid line) in case 4P [extinction model activated]. (a) Fuel mass loss rate; (b) MLR and BR in the simulation; (c) Vent flow rates (upper and lower vents); (d) FDS-based isocontour plot of mixture fraction in the central vertical plane; (e) Oxygen mole fraction (near floor and ceiling); (f) Carbon dioxide mole fraction (near floor and ceiling)
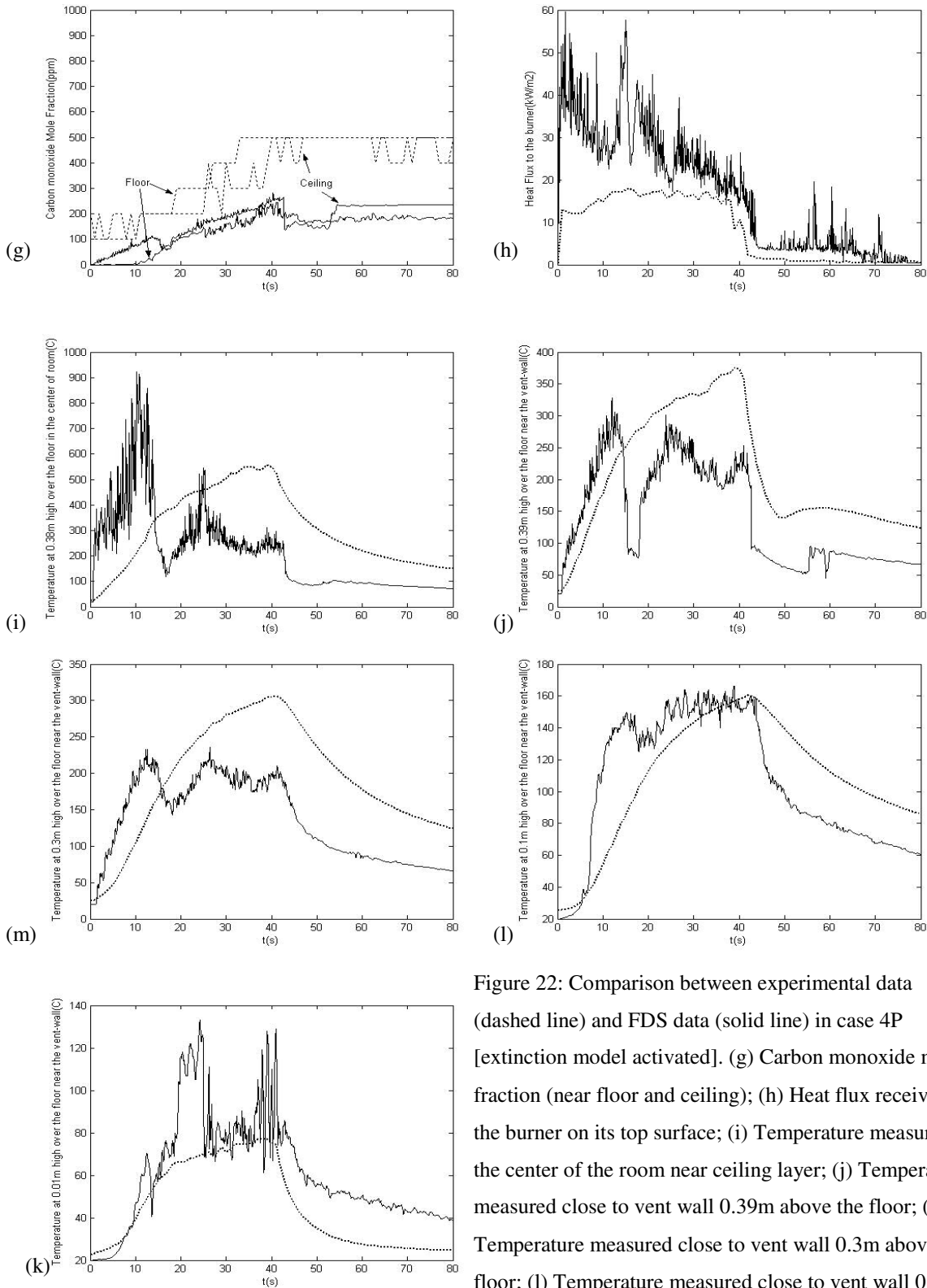
Figure 22: Comparison between experimental data (dashed line) and FDS data (solid line) in case 4P [extinction model activated]. (g) Carbon monoxide mole fraction (near floor and ceiling); (h) Heat flux received by the burner on its top surface; (i) Temperature measured in the center of the room near ceiling layer; (j) Temperature measured close to vent wall 0.39m above the floor; (k) Temperature measured close to vent wall 0.3m above the floor; (l) Temperature measured close to vent wall 0.1m above the floor; (m) Temperature measured close to vent wall 0.01m above the floor;

Chapter VII. Simulation results compared against experiments

--- calculating mass loss rate, with extinction model

The calculated fuel mass loss rate cases are simulated again, with the extinction model turned on. These are the cases closest to reality so far because flame extinction occurs in the experiment and the fuel mass loss rate is determined by the thermal feedback. Differences with results from previous chapters will be highlighted.Heat flux data here are missing too.

7.1   Case 1C

Similar to chapter VI, the extinction model has no effect in this simulation, and the differences between figure 23 and figure 15 are small. A jump in the fuel mass loss rate is observed at t = 140s. This jump remains unexplained.
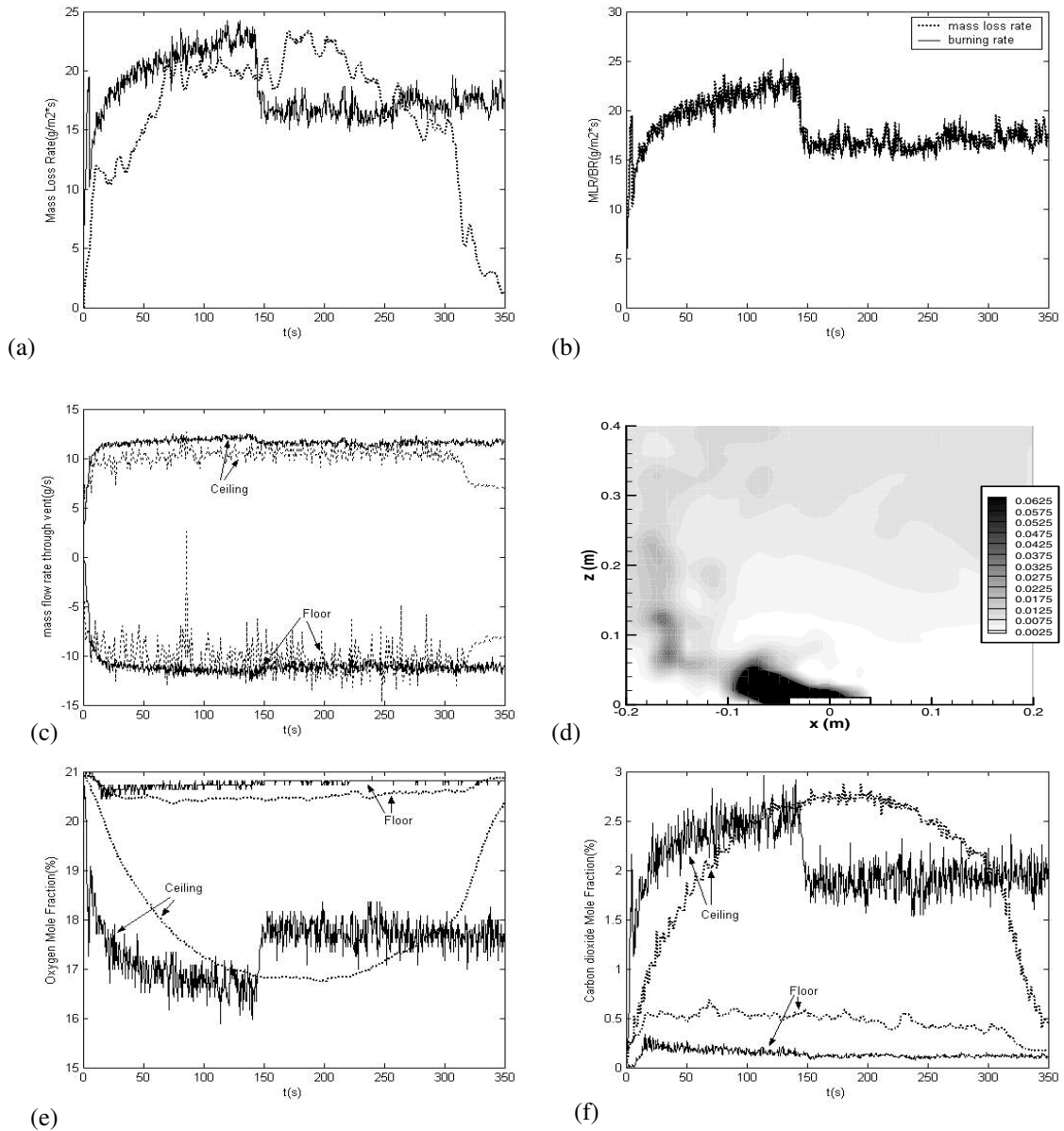
(a)

(b)

(c)

(d)

(e)

(f)

Figure 23 (*to be continued*): Comparison between experimental data (dashed line) and FDS data (solid line) in case 1C [extinction model activated]. (a) Fuel mass loss rate; (b) MLR and BR in the simulation; (c) Vent flow rates (upper and lower vents); (d) FDS-based isocontour plot of mixture fraction in the central vertical plane; (e) Oxygen mole fraction (near floor and ceiling); (f) Carbon dioxide mole fraction (near floor and ceiling)
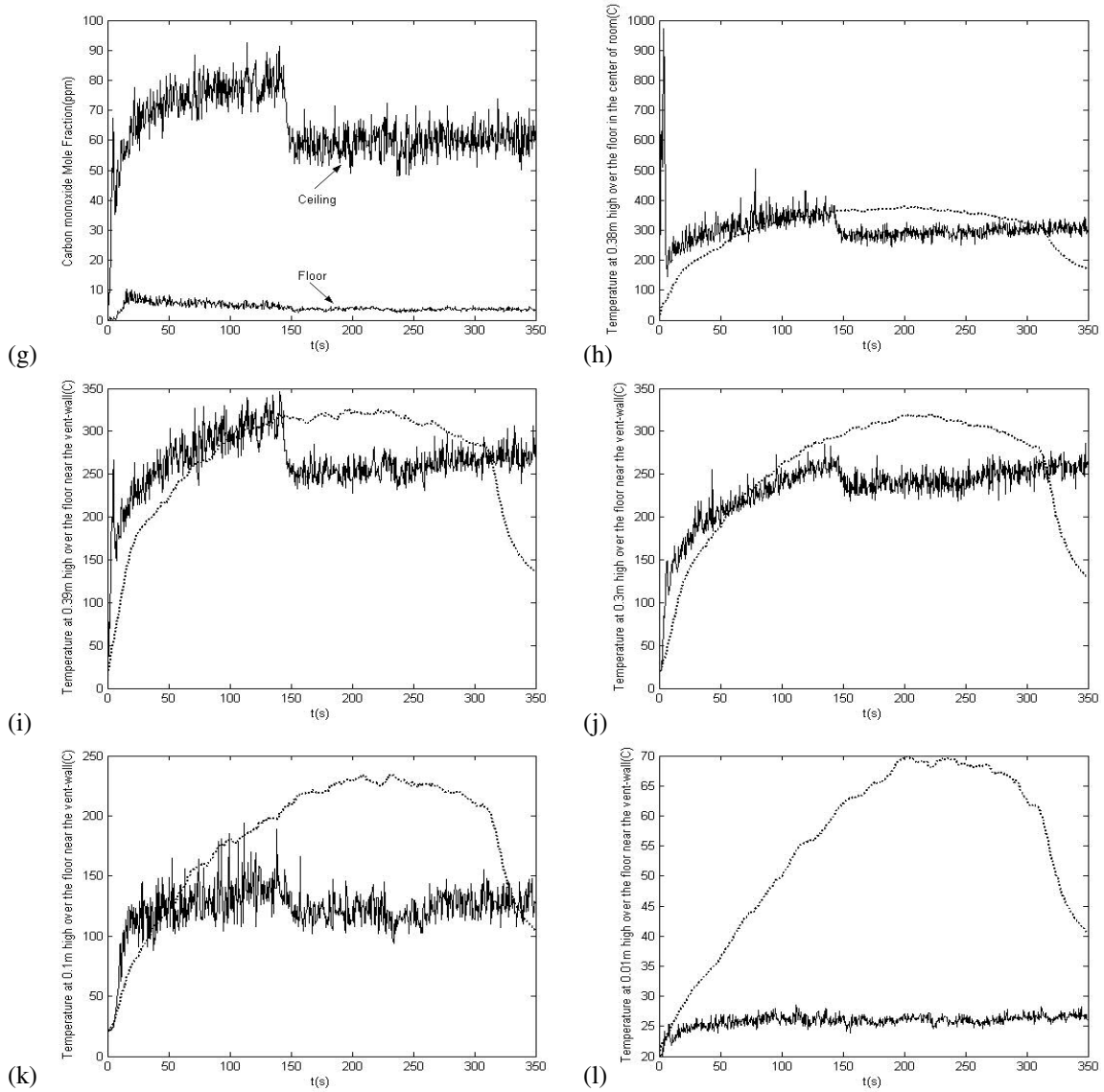
(g) (h) (i) (j) (k) (l)

Figure 23: Comparison between experimental data (dashed line) and FDS data (solid line) in case 1C [extinction model activated]. (g) Carbon monoxide mole fraction (near floor and ceiling); (h) Temperature measured in the center of the room near ceiling layer; (i) Temperature measured close to vent wall 0.39m above the floor; (j) Temperature measured close to vent wall 0.3m above the floor; (k) Temperature measured close to vent wall 0.1m above the floor; (l) Temperature measured close to vent wall 0.01m above the floor.

81

7.2 Case 2C

Case 2 is characterized by a global equivalence ratio of about 2, indicating air-limited conditions, which can also be observed in fig.24(b) by comparing BR and MLR data. In case 2C without the extinction model, the fuel mass loss rate is calculated to be increasing up to 35 $g/m^2/s$. But with the extinction model, the calculated mass loss rate is seen to be nearly constant at about 12 $g/m^2/s$ in fig. 24(a), which is much less than the experimental values.

The predicted vent flow rates remain unchanged as well as the composition of the ceiling layer. With the new extinction model, the oxygen level are increased, and the CO_2 levels are decreased in the lower layer. The data also show more fluctuation, suggesting that local extinction happens here and it helps improve the air vitiation situation.

Fig.24 (d) shows the snapshot of the mixture fraction isocontour at an arbitrary time in the central plane of the compartments that cuts through the fuel pan and the vents. In fig. 12(d) when the same case is simulated without the extinction model on, the flame surface is visible and tends to be near the vent. In this case, the flame surface is pushed the burner, suggesting fuel-limited condition.

In the same case done in chapter V, the temperatures were over-predicted, but here the temperatures are under-predicted.
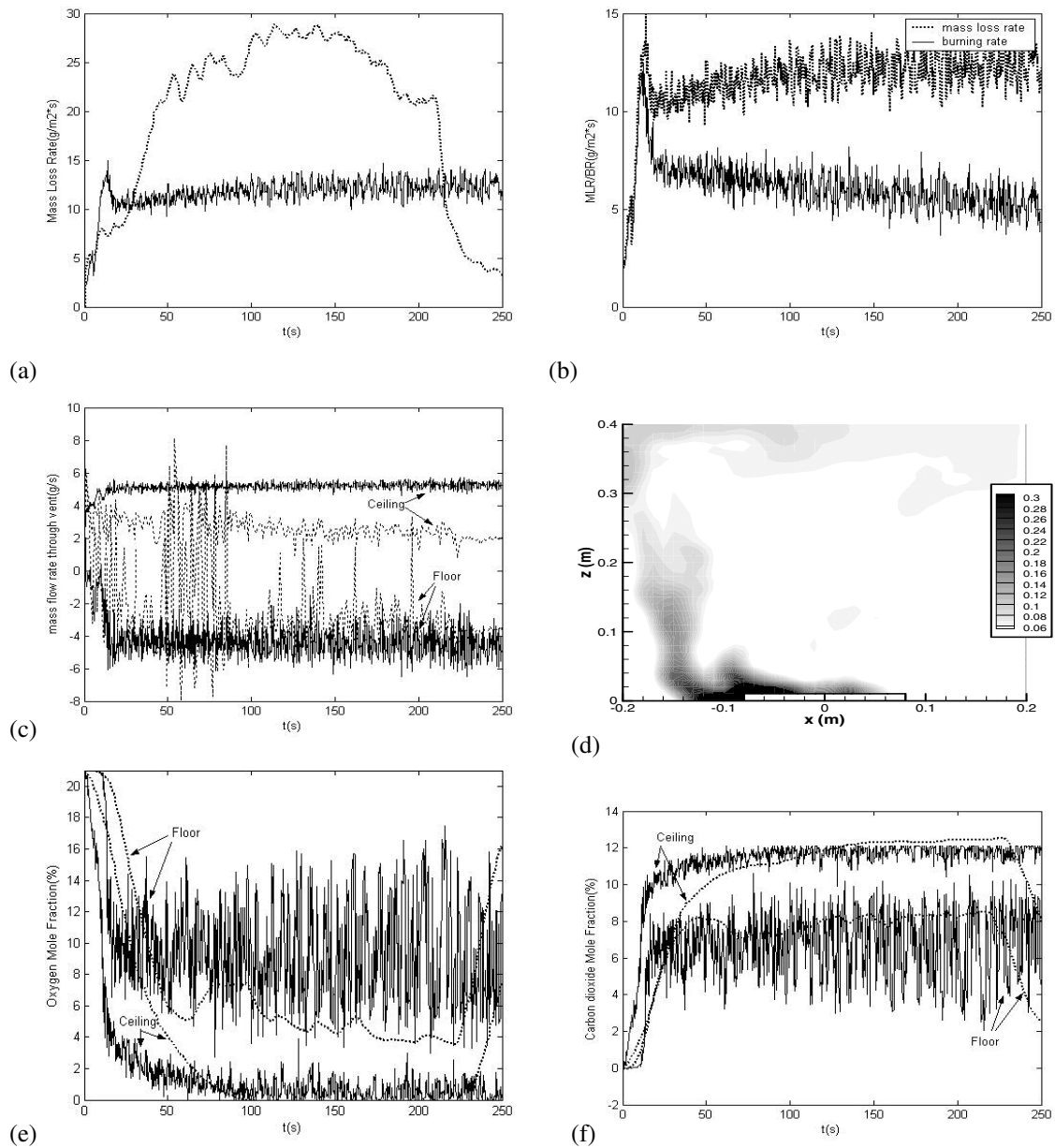
(a)

(b)

(c)

(d)

(e)

(f)

Figure 24(*to be continued*): Comparison between experimental data (dashed line) and FDS data (solid line) in case 2C [extinction model activated]. (a) Fuel mass loss rate; (b) MLR and BR in the simulation; (c) Vent flow rates (upper and lower vents); (d) FDS-based isocontour plot of mixture fraction in the central vertical plane; (e) Oxygen mole fraction (near floor and ceiling); (f) Carbon dioxide mole fraction (near floor and ceiling)
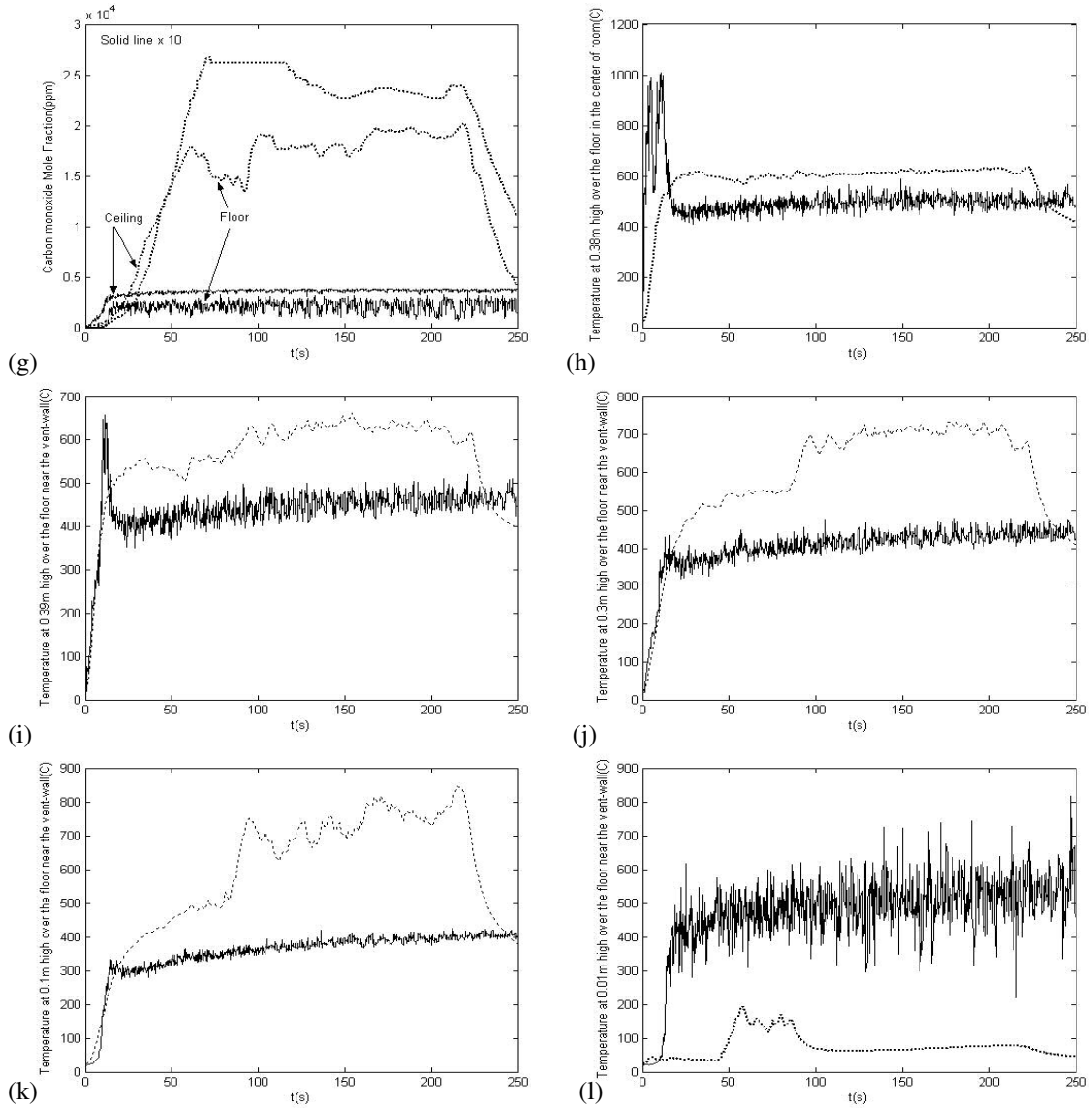
Figure 24: Comparison between experimental data (dashed line) and FDS data (solid line) in case 2C [extinction model activated]. (g) Carbon monoxide mole fraction (near floor and ceiling); (h) Temperature measured in the center of the room near ceiling layer; (i) Temperature measured close to vent wall 0.39m above the floor; (j) Temperature measured close to vent wall 0.3m above the floor; (k) Temperature measured close to vent wall 0.1m above the floor; (l) Temperature measured close to vent wall 0.01m above the floor;

7.3 Case 3C

Next we consider case 3C done with the extinction model on. Compared the one presented in chapter V when extinction model is deactivated, the jump on the curve of calculated mass loss rate occurred earlier in this case, which is at about 150 seconds.

(a)

(b)

(c)

(d)

(e)

(f)

Figure 25 (*to be continued*): Comparison between experimental data (dashed line) and FDS data (solid line) in case 3C [extinction model activated]. (a) Fuel mass loss rate; (b) MLR and BR in the simulation; (c) Vent flow rates (upper and lower vents); (d) FDS-based isocontour plot of mixture fraction in the central vertical plane; (e) Oxygen mole fraction (near floor and ceiling); (f) Carbon dioxide mole fraction (near floor and ceiling)

The fuel mass loss rate in this case is severely under-predicted, resulting in better ventilation conditions than actually observed, and no flame extinction.
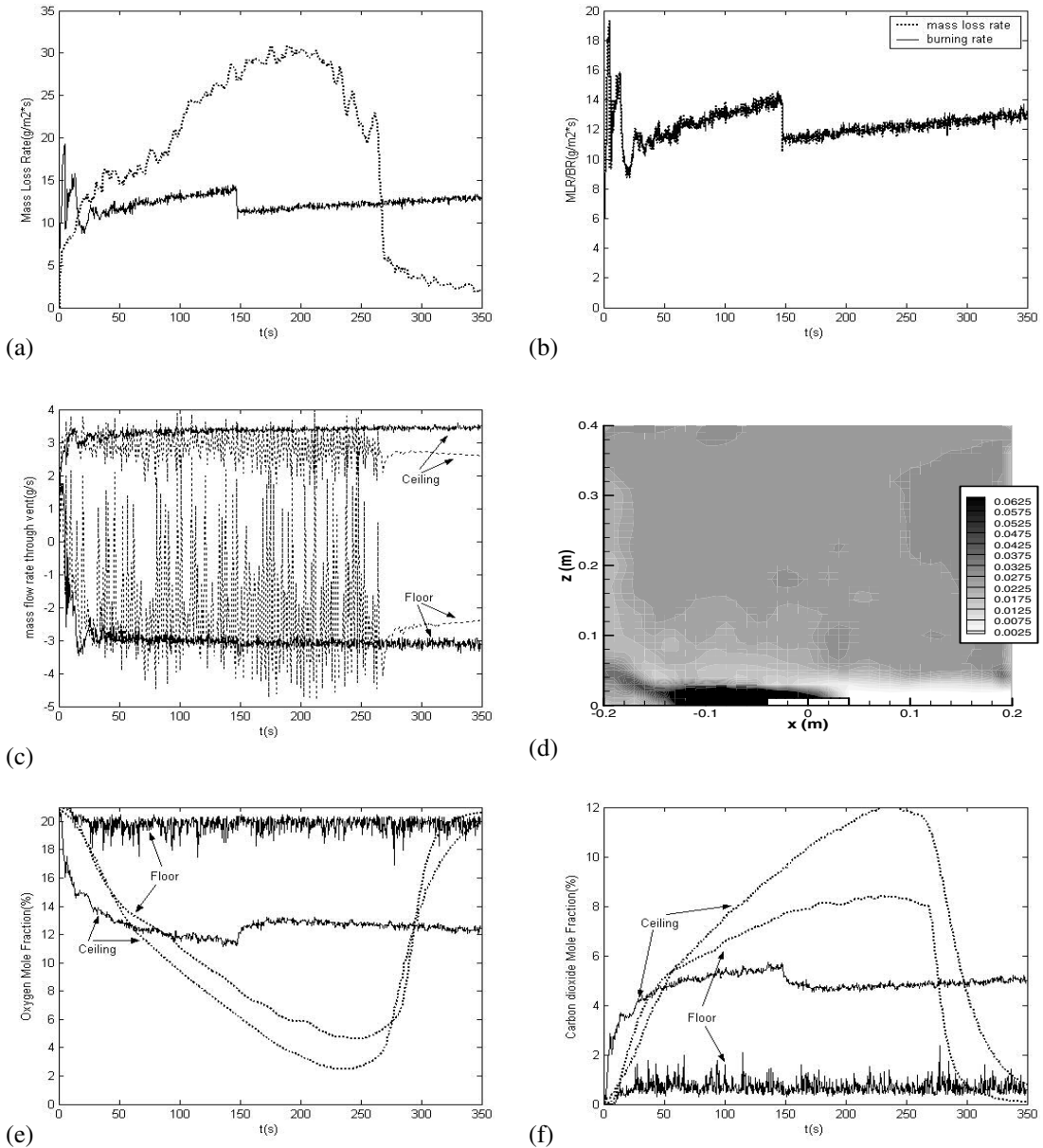

Figure 25: Comparison between experimental data (dashed line) and FDS data (solid line) in case 3C [extinction model activated]. (g) Carbon monoxide mole fraction (near floor and ceiling); (h) Temperature measured in the center of the room near ceiling layer; (i) Temperature measured close to vent wall 0.39m above the floor; (j) Temperature measured close to vent wall 0.3m above the floor; (k) Temperature measured close to vent wall 0.1m above the floor; (l) Temperature measured close to vent wall 0.01m above the floor.

86

7.4 Case 4C

Finally we consider case 4C with the extinction model on. Fig. 26(a) shows the calculated fuel mass loss rate per unit area as well as the experimental data. Compared to the same case simulated without the extinction model in fig. 14(a), in which the mass loss rate decrease continuously but still finite, the MLR here first decreases fast to 2 g/m^2/s, at time t ≈ 30s, and then drop down to zero at about t ≈ 70 s, when a total extinction happens and no reignition takes place. The simulation of total flame extinction here assures us that the extinction model is capable of handling global extinction and also calls for further studies on fire reignition in FDS.

After the significant decrease in fuel mass loss rate at t ≈ 30s, the burning rate is starting to depart from the mass loss rate. This indicates partial flame extinction events, global flame extinction is observed when BR goes to zero, at time t = 70s.

The snapshot of mixture fraction isocontours is picked at a time after extinction happens, and we see no flame at all. Calculated species data agree only qualitatively with the experimental data, and suggest a semi-uniform room composition. Compared to the same case simulated without extinction model in fig. 14(e, f, g), this numerical data set gives a little bit more oxygen and less CO_2, CO, so a less vitiated environment. Temperature levels are over-estimated prior to extinction.
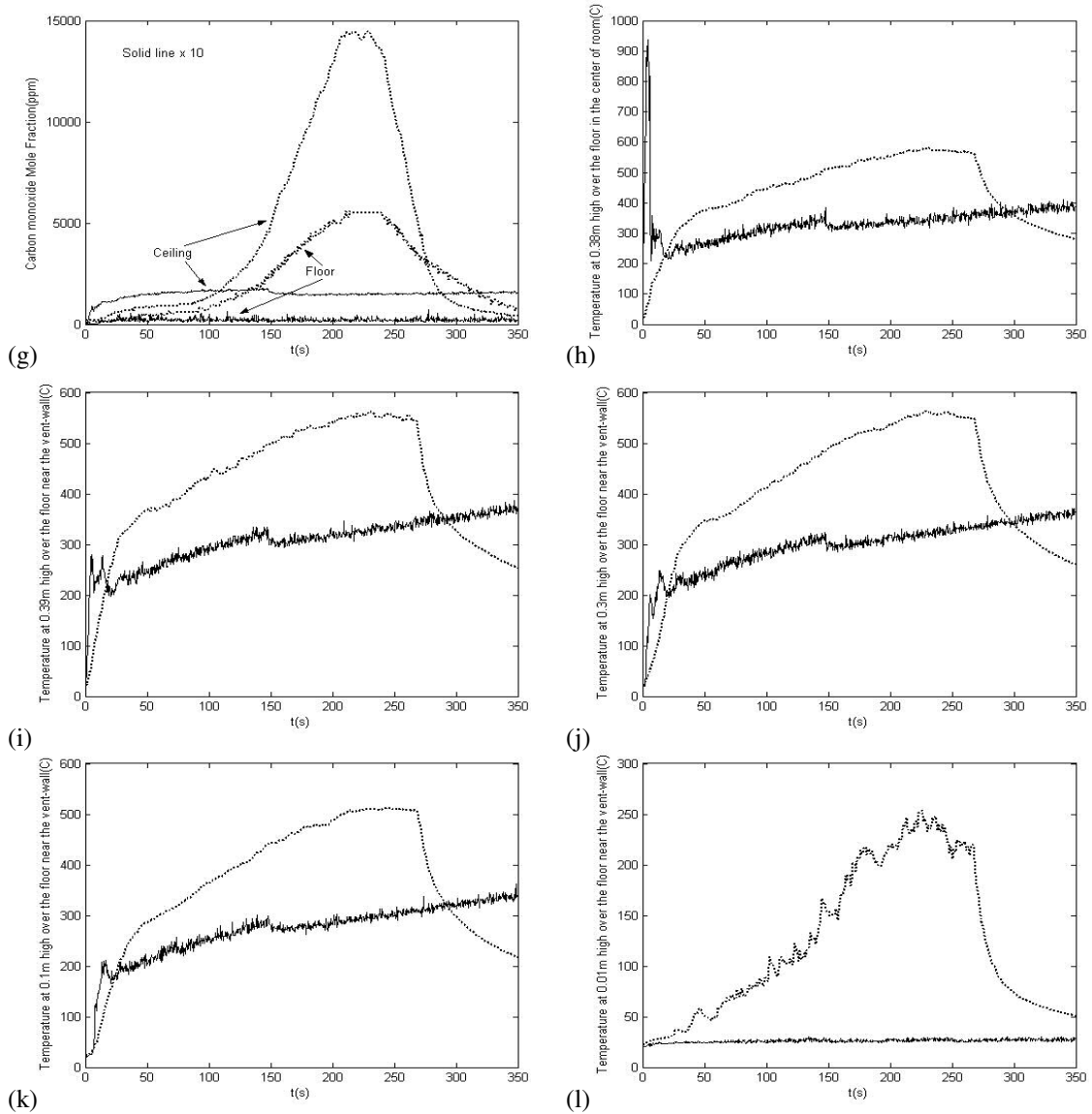
(a)

(b)

(c)

(d)

(e)

(f)

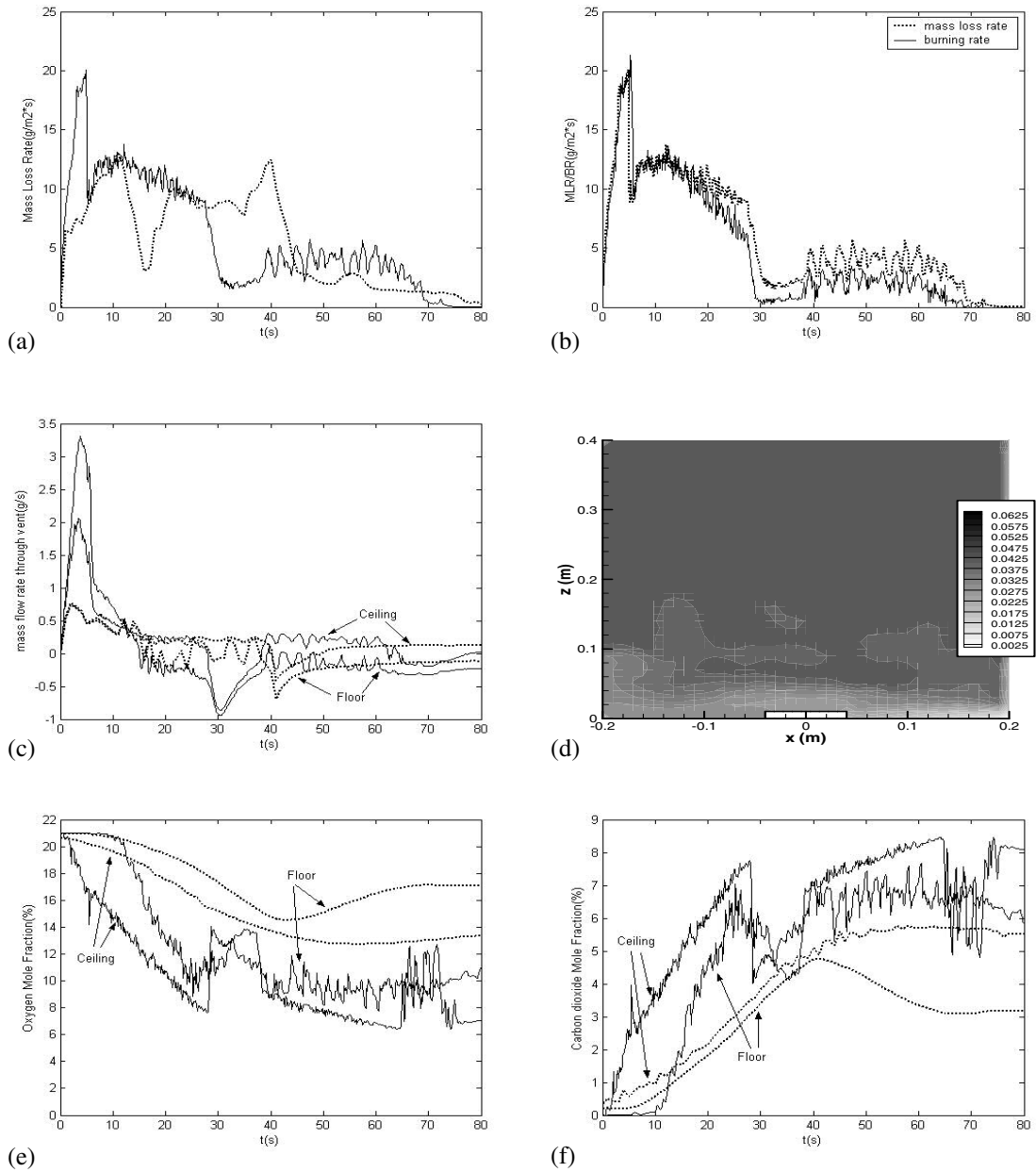Figure 26 (*to be continued*): Comparison between experimental data (dashed line) and FDS data (solid line) in case 4C [extinction model activated]. (a) Fuel mass loss rate; (b) MLR and BR in the simulation; (c) Vent flow rates (upper and lower vents); (d) FDS-based isocontour plot of mixture fraction in the central vertical plane; (e) Oxygen mole fraction (near floor and ceiling); (f) Carbon dioxide mole fraction
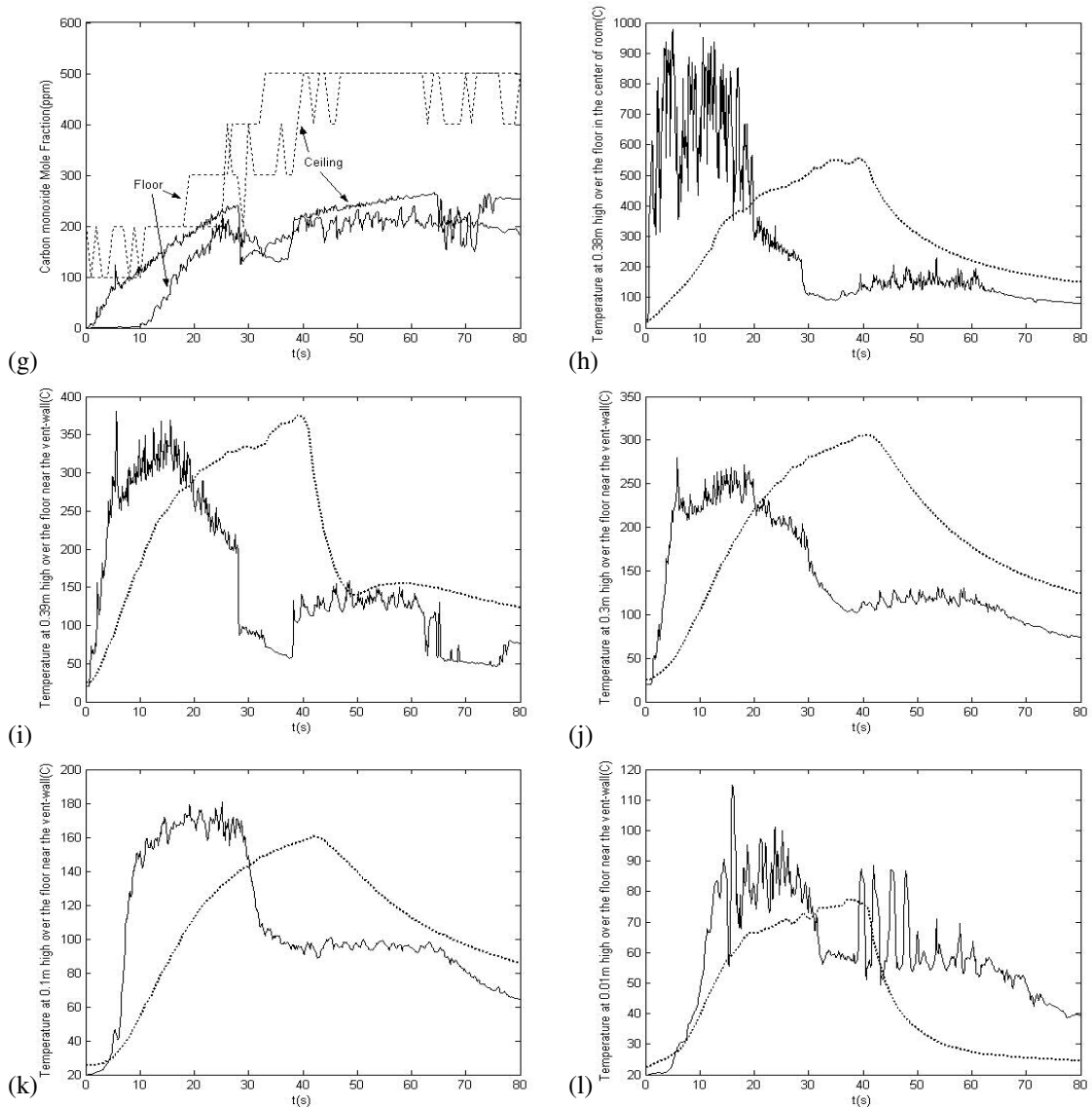
Figure 26: Comparison between experimental data (dashed line) and FDS data (solid line) in case 1P [extinction model activated]. (g) Carbon monoxide mole fraction (near floor and ceiling); (h) Temperature measured in the center of the room near ceiling layer; (i) Temperature measured close to vent wall 0.39m above the floor; (j) Temperature measured close to vent wall 0.3m above the floor; (k) Temperature measured close to vent wall 0.1m above the floor; (l) Temperature measured close to vent wall 0.01m above the floor.

Chapter VIII. Grid refinement effect

This chapter describes a grid refinement study and an evaluation of the numerical quality of the previous simulation. Grid size is always an issue in CFD, not only because it determines the computational cost, but also because it determines numerical accuracy (not only the spatial accuracy, but also the temporal accuracy because the grid size determines the time step). FDS uses a combined central-differencing/upwind-differencing scheme that is second/first order accurate, and the numerical truncation error will be first order or second order in terms of the grid size Δx. Reducing Δx leads to increased numerical accuracy as well as increased physical modeling fidelity since more length scales and flow dynamics are directly captured by the grid.

It is mentioned in previous chapters that the vent flow fluctuations are not captured by FDS simulations, especially in case 3 for which experimentally observed fluctuations are so high that the lower vent oscillations between inflow and outflow conditions. So here we will examine the grid refinement effect by focusing on the mass flow rates at the lower and upper vents and comparing results to the experimental data. Two cases–Case 1P and Case 3P are selected here since case 1 has the most steady vent flow while case 3 has the biggest fluctuations. Both cases are simulated with the extinction model on cases studied in chapter 6 will be the reference.

Figure 27 presents the effect of refining the grid on vent flows in case 1P. Fig.27 (a) shows vent flows measured in the experiment, in which the flow through lower vent has a little fluctuation while the flow through the upper vent is smooth. Fig.27 (b) shows the

vent flows calculated in FDS simulation with a uniform grid size of 1cm, which

corresponds to the case shown in figure 19(c) in chapter 6 (the grid size is 40^3+40^3 for

the two compartments, or 128000). Fig.27 (c) shows the vent flows calculated in a FDS

simulation with the grid size of 0.5 cm in the fire room while the outside of the fire room

still keeps a 1cm grid size. The grid size is 40^3+80^3, or 576000 grid cells. Fig.27 (d)

shows the vent flows calculated in a simulation with the grid size in the region near the

vent inside and outside of the fire room at 0.25 cm while most of the other regions keep

1 cm grid size. The grid size here is 39*40*40+39*40*40+8*160*160, or 329600 grid

cells, which is less than the computational load in Fig.27(c). Since this case corresponds

to a steady fire and the vent flow is also steady, the calculations are not always

conducted up to t = 350 s.

Fig. 27(b-d) show little difference in the FDS predictions and still less fluctuation

than observed experimentally at the lower vent, which suggests that grid refinement is
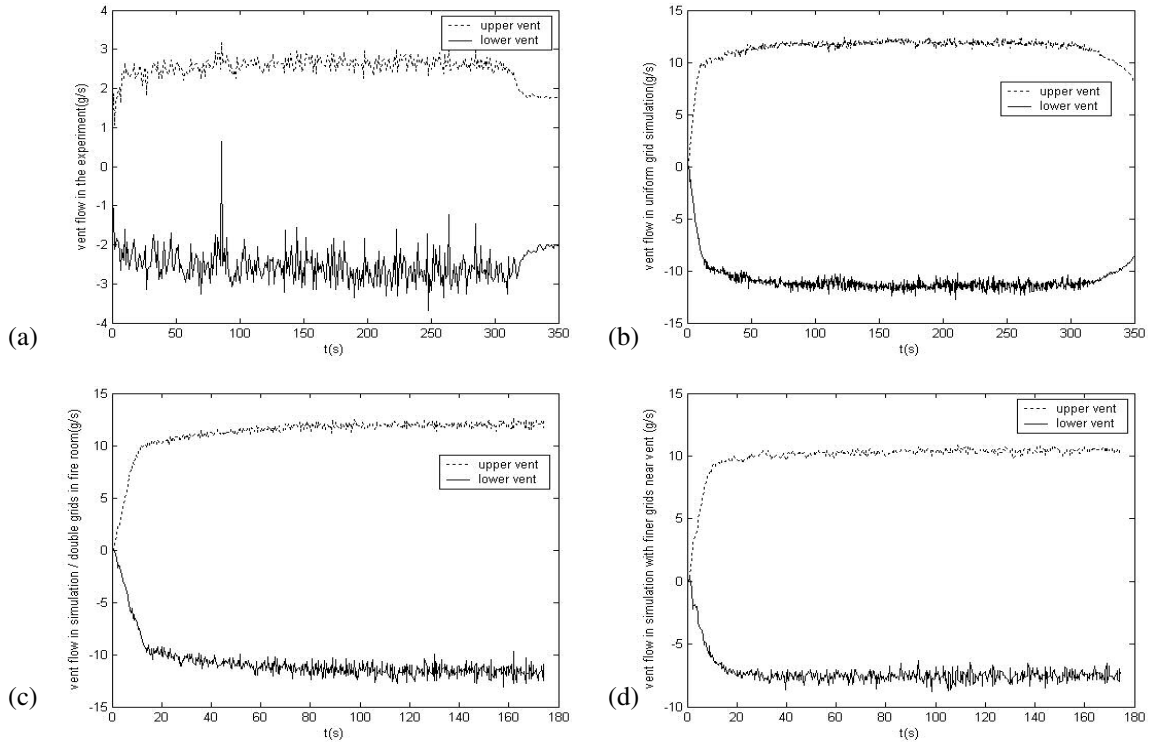
not helping much for this case.

Figure 27: Grid refinement effect on vent flows in case 1P (with extinction model on). (a) vent flows measured in experiment; (b) vent flows calculated in simulation with uniform grid size of 1cm; (c) vent flows calculated in simulation with the grid size of 0.5 cm in fire room while the outside of the fire room still keeps 1cm grid size; (d) vent flows calculated in simulation with the grid size in the region near the vent inside and outside of the fire room at 0.25 cm while most of other regions keep 1 cm grid size.

We now move to case 3P now and perform a same grid refinement study similar to that above. Fig.28 (a) shows the vent flows measured in the experiment; fig.28 (b) shows the vent flows calculated in a simulation with uniform grid size of 1cm; fig.28 (c) shows the vent flows calculated in a simulation with the grid size of 0.5 cm in the fire room while the outside of the fire room still keeps 1cm grid size; fig.28 (d) shows vent flows calculated in a simulation with the grid size in the region near the vent inside and outside of the fire room at 0.25 cm while most of other regions keep a 1 cm grid size.

Compared to the case using uniform grid of 1 cm as in fig.28 (b), the case using a grid

size of 0.5 cm in the fire room in fig.28(c) predicts more flow fluctuations, but not to the

point of reversing the flow at the lower vent. The case in fig. 28 (d), which uses a grid

size of 0.25 cm near the vent, gives the best numerical results with large oscillations and

occasional flow reverse events. This suggests that for case 3, a fine grid near the vent

help resolve the flow dynamics.

(a)
(b)
(c)
(d)
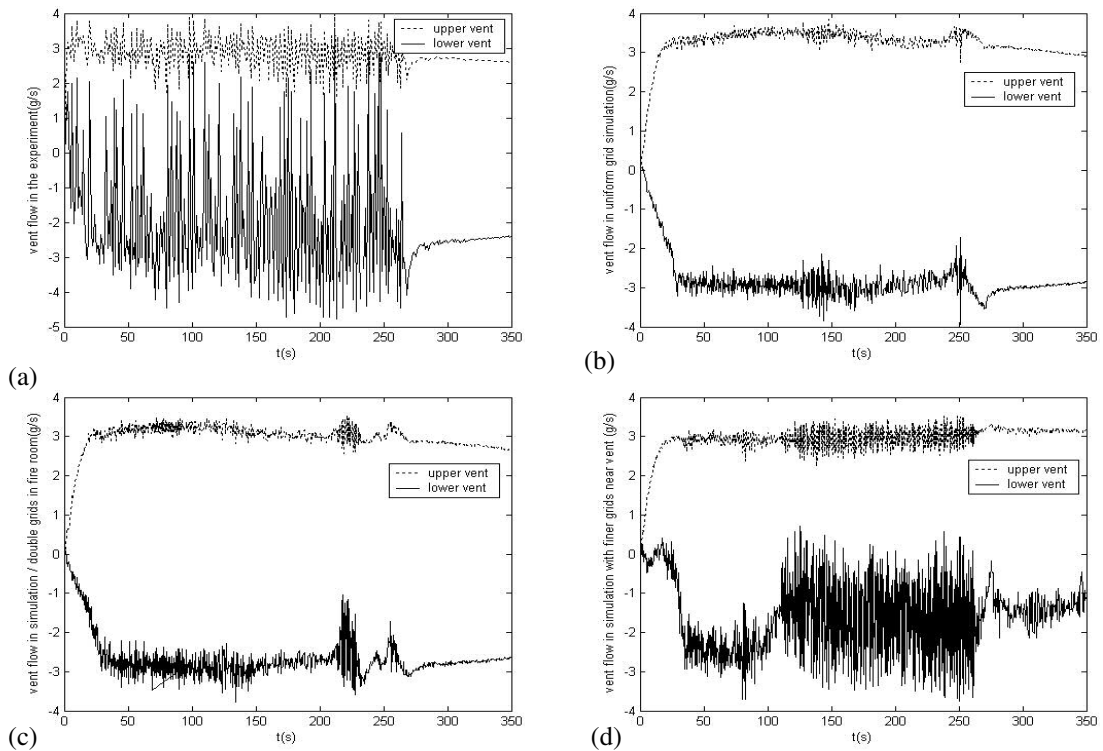
Figure 28: Grid refinement effect on vent flows in case 3P (with extinction model on). (a) vent
flows measured in experiment; (b) vent flows calculated in simulation with uniform grid size of
1cm; (c) vent flows calculated in simulation with the grid size of 0.5 cm in fire room while the
outside of the fire room still keeps 1cm grid size; (d) vent flows calculated in simulation with the
grid size in the region near the vent inside and outside of the fire room at 0.25 cm while most of
other regions keep 1 cm grid size.

Chapter IX. Conclusion

This study provides an evaluation of FDS for flame extinction events in compartment fire simulations. Four cases are selected to represent four fire categories: (R1) steady well-ventilated fires in which the flame is stabilized above the burner; (R2) steady under-ventilated fires in which the flame is stabilized near the vents; (R3) unsteady under-ventilated fires featuring large periodic oscillations and temporary flame quenching; (R4) unsteady under-ventilated fires leading to complete flame extinction. For each case, the FDS simulations are performed four times, with a prescribed or a calculated fuel mass loss rate, without or with flame extinction. The numerical results are compared to an existing experimental database, in terms of mass loss rate, burning rate, vent flow rates, flame structure, heat flux to the burner, species mass fraction and temperature measured at different locations in the fire room.

When we choose to prescribe the experimental fuel mass loss rate, the comparison between FDS and experimental data provides encouraging results. The results are best in the absence of flame extinction (R1 and R2 in our terminology). The new flame extinction model incorporated in FDS does improve the results for R3 and R4, but these results remain preliminary and qualitative. It is shown, however, that the new model allows the simulation of partially- or- totally- extinguished flames.

Appendix I. Calculation of the free-burn value of the fuel mass loss rate for an heptane pool

For liquid pool fires, the free-burn value of MLR may be expressed as [42]:

$$\dot{m}'' = \dot{m}''_\infty (1 - e^{-k\beta D})$$

in which $\dot{m}''_\infty$ and $k\beta$ are two empirical constants, and D is the pool diameter. For heptane:

$$\dot{m}''_\infty = 101 \ \ g/m^2/s$$

$$k\beta = 1.1 \ \mathrm{m}^{-1}$$

So for cases 1, 3 and 4, we have $D=$ 9.5cm and:

$$\dot{m}'' = \dot{m}''_\infty (1 - e^{-k\beta D}) = 101 \times (1 - e^{-1.1 \times 0.095}) = 10.02 g/m^2/s$$

For case 2, $D=$19 cm, and:

$$\dot{m}'' = \dot{m}''_\infty (1 - e^{-k\beta D}) = 101 \times (1 - e^{-1.1 \times 0.19}) = 19.05 g/m^2/s$$

Appendix II. Calculation of the time required to deplete the initial air present in the compartment prior to ignition (case 4)

From the mass loss rate in figure 14, we can estimate the average MLR at steady state to be 10 g/m²/s, the buner size is 0.08*0.08 m², so the injected fuel mass flow rate is:

$$\dot{m}_f = 10*0.08*0.08\, g/s = 0.064\, g/s$$

Assume the air density to be $\rho=1.2$ kg/m³, the compartment size is 0.4*0.4*0.4 m, so the amount of air initially present in the compartment is

$$m_{air} = 0.4^3\, m^3 * 1200\, g/m^3 = 76.8\, g$$

The stoichiometic ratio of heptane to oxygen r_s=3.52, the oxygen mass fraction in the air Y_{ox}=0.233, so we can estimate the time to deplete the air initially in the compartment as:

$$t = \frac{m_{air} \times Y_{ox}}{r_s \times \dot{m}_f} = \frac{76.8g \times 0.233}{3.52 \times 0.064\, g/s} \approx 79s$$

Reference

1. E.E.Zukoski. (1986) "Fluid dynamic aspects of room fires", *Fire Safety Science, Proceedings of the First International Symposium*, p.1-30.

2. A.Tewarson. (1996), "Ventilation effects on combustion products"*, Toxicology*, **115**: p. 145-156.

3. W.M.Pitts. (1995), "The global equivalence ratio concept and the formation mechanisms of carbon monoxide in enclosure fires"*, Prog. Energy Combust. Sci.*, **21**: p. 197-237.

4. M.P.Tolocka. (1999), "The effect of global equivalence ratio and postflame temperature on the composition of emissions from laminar ethylene/air diffusion flames", *Combustion and flame*, **118**: p. 521-536.

5. C.Beyler. (2002), "Flammability limits of premixed and diffusion flames", *SFPE Handbook of Fire Protection Engineering, NFPA (3rd Ed.)*, **2**: p. 172-187.

6. Wang, Y. and Trouvé, A. (2005) "Direct numerical simulation of non-premixed flame-wall interactions", *submitted to Combust. Flame*.

7. N.Peters. (1983), "Local Quenching Due to Flame Stretch and Non-Premixed Turbulent Combustion", *Combustion Science and Technology*, **30**: p. 1-17.

8. C.D.Pierce, P.Moin. (1998), "A dynamic model for subgrid-scale variance and dissipation rate of a conserved scalar"*, Phys. Fluids*, **10**: p. 3041-3044.

9. S.Leonard. (1994), "Generation of CO and Smoke during Underventilated Combustion", *Combustion and Flame*, **98**: p. 20-34.

10. D.T.Gottuk, B.Y.Lattimer. (2002), "Effect of combustion conditions on species production", *SFPE Handbook Fire Protection Eng., NFPA(3rd Ed.)*, **2**: p.54-82.

11. C.L.Beyler. (1986). "Major species production by solid fuels in a two-layer compartment fire environment", *Fire Safety Science, Proceedings of the First International Symposium,*p.431-440.

12. E.E.Zukoski. (1989) "Combustion Processes in Two-layered Configurations", *Fire Safety Science, Proceedings of the Second International Symposium*, p.295-304

13. J.H.Morehart, E.E.Zukoski. (1992), "Chemical Species Produced in Fires Near the Limit of Flammability"*, Fire Safety Journal*, **19**: p. 177-188.

14. E.E.Zukoski, J.H.Morehart. (1991), "Species Production and Heat Release Rates in Two-Layered Natural Gas Fires". *Combustion and Flames*, **83**: p. 325-332.

15. C.L.Beyler. (1984), "Ignition and burning of a layer of incomplete combustion products"*, Combustion. Science Technology*, **39**: p. 287-303.

16. W.M.Pitts. (1992), "Reactivity of product gases generated in idealized enclosure fire environments", *Proc. Combust. Inst.*, **24**: p. 1737-1746.

17. S.Lomax & R.F.Simmons. (1986) "The Formation of Carbon Monoxide from Diffusion Flames", *Fire Safety Science, Proceedings of the First International Symposium*, p.441-450

18. G.Mulholland. (1991) "The Effect of Oxygen Concentration on CO and Smoke Produced by Flames", *Fire Safety Science, Proceedings of the Third International Symposium*, p.585-594

19. D.T.Gottuk, R.J.Roby & C.L.Beyler. (1995) "The role of temperature on carbon monoxide production in compartment fires", *Fire Safety Journal,* **24**: p. 315-331.

20. F.A.Williams. (1985) *Combustion Theory, Benjamin/Cummings (2nd Ed.).*

21. T.Poinsot, D.Veynante. (2001) *Theoretical and numerical combustion*, Edwards.

22. S.M.Hyde & J.B.Moss. (2002) "Modelling CO Production in Vitiated Compartment Fires", *Fire Safety Science, Proceedings of the Seventh International Symposium*, p.395-406

23. H.Tuovinen. "CFD Modelling of Under-Ventilated Fires", *Swedish National Testing and Research Institute Report 1996:41,* ISSN 0284-5172, ISBN 91-7848-646-7

24. H.Tuovinen. "CO Formation from Soot and CO2 in the Hot Gas Layer"*, Swedish National Testing and Research Institute Report 2002:08,* ISSN 0284-5172, ISBN 91-7848-899-0

25. H.Tuovinen, M.Simonson. "Incorporation of Detailed Chemistry into CFD Modelling of Compartment Fires", *Swedish National Testing and Research InstituteReport 1999:03*, ISSN 0284-5172, ISBN 91-7848-757-9.

26. W.M.Pitts.(1997) "An Algorithm for Estimating Carbon Monoxide Formation in Enclosure Fires". *Fire Safety Science, Proceedings of the Fifth International Symposium*, p.535-546

27. J.G.Quintiere.(2002) "Fire Behavior in building compartments". *Proc. Combust. Inst.,* **29:**p.181-193

28. V.Novozhilov.(2001) "Computational fluid dynamics modeling of compartment fires". *Prog. Energy Combust. Sci.*, **27**: p. 611-666.

29. D.Veynante, L.Vervisch. (2002) "Turbulent Combustion Modeling". *Progress in Energy and Combustion Science*. **28**: p. 193-266.

30. L.Vervisch, T.Poinsot. (1998) "Direct numerical simulation of non-premixed turbulent flames". *Annu. Rev. Fluid Mech.* **30**: p. 655-691.

31. K.McGrattan, H.Baum, R.Rehm, A.Hamins, G.Forney, J.Floyd&S.Hostikka."Fire Dynamics Simulator – Technical Reference Guide". *NIST Internal Report, NISTIR 6783.*

32. K.McGrattan, J.Floyd, G.Forney, H.Baum, S.Hostikka.(2001) "A mixture fraction combustion model for large scale fire modeling". *Proc. Intl. Mech. Eng. Congress and Exposition.*

33. K.McGrattan, J.Floyd, G.Forney, H.Baum, S.Hostikka.(2001) "Development of combustion and radiation models for large scale fire simulation". *Third Tech. Symp. Comp. Appli. In Fire Protection Eng.*: SFPE.

34. Y.Utiskul.(2005) "Compartment fire phenomena under limited ventilation". *Fire Safety Journal*. **40**: p. 367-390.

35. Z.Hu, Y.Utiskul. (2005) "A comparison between observed and simulated flame structures in poorly ventilated compartment fires". *Fire Safety Science, Proceedings of the Eighth International Symposium, Beijing.*

36. A.Marshall, J. Quintiere. (2003)*"Experimental investigation of vitiated flame behavior and self-extinction in fires", proposal submitted to NIST/BFRL.*

37. Z.Hu, G.Panafieu, J.Stauder, A.Trouvé. (2004) *"A presumed Pdf approach to model turbulent non-premixed combustion in FDS", Intl. Tech. Congress on Computational Simulation Models in Fire Engr. and Res., Ed. J. A. Capote Abreu, GIDAI, Univ. Cantabria, Santander, Spain*, p.281-295.

38. N.Pierce. (1983) *Combust. Sci. Technol.* **30**:1-17

39. J. S. T'ien. (1986) "Diffusion flame extinction at small stretch rates: the mechanism of radiative loss". *Combustion and flame* **65**: p31-34

40. I.K.Puri, K.Seshadri. (1986) "Extinction of diffusion flames burning diluted methane and diluted propane in diluted air". *Combustion and flame* **65**: p.137-150

41. M.H.Yang, A.Hamins, I.K.Puri. (1994) "The structure of inhibited counterflowing nonpremixed flames". *Combustion and flame* **98**: p.107-122

42. A.Hamins. (1994) "Extinction of nonpremixed flames with halogenated fire suppressants". *Combustion and flame* **99**: p.221-230

43. V.Babraukas. (2002) "Heat Release Rate", *The SFPE Handbook of Fire Protection Engineering, National Fire Association (3rd ed.)* **3**: p.25-26